

Transient phenomena of scalar transport during accidental gas releases in urban environments

Dissertation

zur Erlangung des Doktorgrades der Naturwissenschaften

im Fachbereich Geowissenschaften

der Universität Hamburg

vorgelegt von

Eva Berbekar

Hamburg

2016

Als Dissertation angenommen vom Fachbereich Geowissenschaften der Universität Hamburg
auf Grund der Gutachten von

Prof. Dr. Bernd Leidl

und

Prof. Dr. Rüdiger Höffer

Hamburg, den 27. Januar 2017

Prof. Dr. Jürgen Böhner

(Leiter des Fachbereichs Geowissenschaften)

Eidesstattliche Versicherung

Hiermit erkläre ich an Eides statt, dass ich die vorliegende Dissertationsschrift selbst verfasst und keine anderen als die angegebenen Quellen und Hilfsmittel benutzt habe.

Declaration on oath

I hereby declare, on oath, that I have written the present dissertation by my own and have not used other than the acknowledged resources and aids.

Hamburg, 09.11.2016

Eva Berbekar

Abstract

Due to the urgency of the situation, in emergencies involving the release of airborne materials in built environments, simple atmospheric dispersion models with a negligible response time are frequently applied. State-of-the-art, high-resolution models are often not capable of the fast response demanded in case of accidental releases. This thesis improves the understanding of the dispersion phenomena in urban environments to help close this gap between theory and praxis.

To study the transient dispersion field in urban environments, boundary layer wind tunnel measurements were carried out. Based on the experimental results, essential questions related to gas dispersion in urban areas are investigated.

The new experimental data sets generated within the scope of this thesis are applicable for the validation of atmospheric dispersion models predicting the concentration field resulting from airborne hazardous materials in local-scale urban environments. Based on the data, a consistent set of characteristics describing transient dispersion are presented and their dimensionless forms are derived.

Gaussian plume models are based on the assumption that the mean concentration profiles follow Gaussian distribution. Although the Gaussian distribution provided sufficient fits on the measured mean concentration profiles, due to the parametrization of the turbulent flow field in local-scale urban environments, Gaussian models have difficulty to predict the concentration field. A strong relationship between the mean and the high percentiles of the concentration distributions was found. General probability density functions provided reasonable fits on the concentration distributions, and sufficiently predicted the higher order statistics based on the first two moments. This indicates that the higher percentiles of a concentration distribution can be determined based on the mean concentration with sufficient accuracy compared to the atmospheric dispersion modeling uncertainties.

The effect of modification and simplification of the building structure on the dispersion field was investigated based on systematic wind tunnel measurements. It was found that geometrical simplification of a larger area generally increased the measured concentration and decreased the characteristic times of dispersion. The modification of a building significantly larger in size than its surroundings had an evident effect on the results. When a building is reconstructed without significant geometrical changes or it is similar in size to its surroundings, the effects are negligible.

Keywords: accidental release, boundary layer wind tunnel, extreme value theory, geometry simplification, probability density functions, residence time, urban dispersion, validation

Kurzfassung

Zur Bestimmung der lokalen Schadstoffkonzentration werden in Störfällen aufgrund der benötigten kurzen Reaktionszeiten einfache und schnelle Prognosemodelle verwendet. Komplexe Modelle mit höherer zeitlichen und räumlichen Auflösung können den Ersthelfern aufgrund der längeren Berechnungsdauer nicht die benötigten Erkenntnisse bereitstellen. Die vorliegende Arbeit soll das allgemeine Verständnis der urbanen Schadstoffausbreitung verbessern und den Stand der Forschung anwendungsorientiert übersetzen.

Auf Basis der für diese Arbeit durchgeführten Untersuchungen im Grenzschichtwindkanal konnten grundlegende Fragestellungen hinsichtlich der Gasausbreitung in Stadtgebieten beantwortet werden. Die experimentellen Datensätze wurden explizit für die Validierung numerischer Störfallmodelle im urbanen Raum erstellt. Basierend auf diesen Daten konnten Charakteristiken des Ausbreitungsverhaltens definiert und dimensionslose Parameter bestimmt werden.

Gaußfahnenmodelle basieren auf der Annahme, dass das mittlere Konzentrationsprofil dem einer Gauß-Verteilung entspricht. Die Analyse der Messdaten zeigt eine gute Annäherung der gemessenen Konzentrationsprofile an eine Normalverteilung, jedoch haben Gaußfahnenmodelle aufgrund der parametrischen Lösung des Strömungsfeldes Schwierigkeiten in der Bestimmung des Konzentrationsfelds.

Bei der Messwertanalyse konnte ein Zusammenhang zwischen dem Mittelwert und den oberen Perzentilwerten einer Konzentrationsverteilung gefunden werden. Allgemein zeigen Verteilungsfunktionen eine gute Anpassung an die gemessenen Konzentrationsprofile sowie eine gute Annäherung an die daraus bestimmten Momente höherer Ordnung. Dies beweist, dass gegenüber den Unsicherheiten in der numerischen Modellierung von Schadstoffausbreitungen die Berechnung der Perzentile einer Konzentrationsverteilung aus einem präzise bestimmten Mittelwert hinreichend genau ist.

Der Einfluss von Umstrukturierungen sowie Modellvereinfachungen auf das Ausbreitungsverhalten wurde anhand systematischer Windkanalstudien untersucht. Großräumige oder an signifikanten Gebäuden ausgeführte Modellvereinfachungen zeigen starke Auswirkungen auf das lokale Konzentrationsfeld und dessen zeitliche Charakteristiken, der Einfluss kleinräumiger Veränderungen ist hingegen vernachlässigbar.

Stichworte: Extremwertanalyse, geometrische Vereinfachung, Grenzschichtwindkanal, Störfallfreisetzung, urbanes Ausbreitungsverhalten, Validierung, Wahrscheinlichkeitsdichtefunktion

Libertatem quam peperere
maiores digne studeat
servare posteritas.

Acknowledgement

First of all, I am thankful for you, dear reader for your interest in my thesis.

I am very thankful for everyone who supported me by encouragement or criticism, interest or indifference, guidance or ignorance. All positive and negative feedback was helping me to get closer to the aim of the last years – writing my PhD thesis. Listing all the people and organizations helping me during my research would be enough to fill a book. Thank you!

I cannot summarize in one paragraph all the things I am thankful for to my supervisor, Bernd Leitl. He allowed me to join the group of the Environmental Wind Tunnel Laboratory for a short-term scholarship, which significantly changed my professional and personal life in a positive manner. I am thankful for accepting me for another year of scholarship, introducing me to the top researchers of our field through the COST Action ES1006 and trusting me with employment at the Environmental Wind Tunnel Laboratory. Thank you for your guidance when I needed help, your encouragement when I had doubts, your patience when I needed time, your understanding when I failed and your appreciation when I succeeded.

I am thankful to Frank Harms for putting up with me as an office mate and for the professional and personal guidance he provided. I would like to thank the whole group of the Environmental Wind Tunnel Laboratory for all the help I received and for the pleasant working environment.

I am thankful to my Fluid Mechanics Professor, Tamás Lajos, who triggered my interest in the topic and invited me to work at the Department of Fluid Mechanics at the Budapest University of Technology and Economics. The years spent at the Department provided the theoretical basis I still rely on during my work. It was an honor to work with the smartest group of people I have ever met and I am thankful to the team of the Department of Fluid Mechanics for sharing their knowledge with me.

The valuable guidance provided by the members of the COST Action ES1006 during the measurements and data processing of the Michelstadt test case is very much appreciated. I am particularly thankful to Anikó Rákai and George Efthimiou for sharing their passion for atmospheric dispersion with me. Their insightful questions, answers and ideas contributed to this work enormously. Their constant motivation provided encouragement for me even in difficult times.

I would like to express my gratitude to the developers of SAGA GIS, especially to Olaf Conrad for his personal tutorials and to Volker Wichmann for the quick forum responses.

I am thankful to Gopal Patnaik and Adam Moses from the US Naval Research Laboratory for their enormous help and constant encouragement throughout the CT-Analyst Hamburg II

project. I am also thankful to Holger Drees at the University of Hamburg for his advice on extreme value theory.

I would like to thank Frieso Kipsch for taking such good care of me when I arrived in Hamburg and ever since. Your patience, help, encouragement and above all, humor helped me to get through the difficult times and made the good times perfect.

Without the support of my family and friends and their faith in me, I would have given up a long time ago. I could not wish for better people to surround me, thank you for always being there for me!

It is greatly acknowledged, that the *Deutscher Akademischer Austauschdienst*, *Deutsche Bundesstiftung Umwelt*, *Campus Hungary*, *COST Action ES1006* and the *Behörde für Inneres und Sport* provided the financial support for the research this thesis relies on.

Last but not least, I am thankful to the evaluators of this thesis, Bernd Leitl and Rüdiger Höffer for the valuable comments and ideas that made this thesis as it is. Their help throughout the correction process is greatly appreciated.

Content

Abstract	v
Kurzfassung.....	vii
Acknowledgement.....	xi
Content	xiii
Nomenclature	xvii
Abbreviations	xvii
List of symbols.....	xviii
Roman symbols.....	xviii
Greek symbols.....	xx
Operators, subscripts and special symbols.....	xxi
1 Introduction	1
1.1 Motivation	1
1.1.1 COST Action ES1006.....	2
1.1.2 CT-Analyst Hamburg II project.....	4
1.2 Scope and scientific importance of the thesis	4
1.3 Structure of the thesis	6
2 Transient dispersion processes	7
2.1 Governing equations	7
2.1.1 Assumptions, simplifications, conventions.....	7
2.1.2 Transport equation	9
2.1.3 Continuity and Navier-Stokes equations	10
2.2 Origin of time dependence	11
2.2.1 Flow field.....	11
2.2.2 Transport and dispersion.....	15
3 Methodology.....	19
3.1 Measurement and characterization of scalar transport in urban environments.....	20
3.1.1 Requirements of small-scale modeling.....	20

3.1.2	Concentration measurements in a boundary-layer wind tunnel.....	23
3.1.3	Characteristic parameters of dispersion	26
3.1.4	Relevant statistics.....	32
3.2	Test cases.....	34
3.2.1	Model geometries.....	34
3.2.2	Wind tunnel facility	36
3.2.3	Preliminary measurements.....	36
3.2.4	Representativeness and reproducibility	41
3.2.5	Data sets	45
3.2.6	Model validation based on the data sets	49
4	Results and discussion	53
4.1	Statistical analysis of continuous release measurements	53
4.1.1	Spatial distribution of concentration	53
4.1.2	Frequency distribution of concentration	63
4.1.3	Extreme value analysis of the frequency distribution.....	70
4.2	Residence time analysis based on short-term releases	77
4.2.1	Characterizing concentration decay measurements	78
4.2.2	Exemplary results of the concentration decay measurements	82
4.3	The effect of geometry modification on the dispersion	87
4.3.1	Results of continuous release measurements.....	90
4.3.2	Results of puff release measurements.....	94
4.3.3	Impact of geometrical modification on the residence time.....	97
5	Conclusions	101
5.1	Summary of the results.....	101
5.1.1	Characterizing the dispersion results of various release scenarios	102
5.1.2	The (in)appropriateness of the Gaussian distribution to model the concentration field in urban areas	102
5.1.3	Predicting high concentrations using probability density functions	103
5.1.4	The impact of geometry modifications and simplifications on the dispersion in urban environments	104
5.2	Outlook.....	105
6	Appendix	107

6.1	Appendix A: Longitudinal, lateral and vertical concentration profiles.....	107
6.2	Appendix B: Effects of geometry modifications on continuous release measurement results	111
6.3	Appendix C: Effects of geometry modifications on puff release measurement results	114
	Bibliography.....	119
	List of Figures	131
	List of Tables.....	141

Nomenclature

Abbreviations

ABL	Atmospheric Boundary Layer
CFD	Computational Fluid Dynamics
COST	European Cooperation in Science and Technology
FAC2	fraction of predictions within a factor of two of observations
FB	Fractional Bias
FID	Flame Ionization Detection/Detector
FS	Full Scale
GEV	Generalized Extreme Value
GPD	Generalized Pareto Distribution
HH	Hamburg
ISL	Inertial Sublayer
LDA	Laser Doppler Anemometer
LDV	Laser Doppler Velocimetry
LES	Large Eddy Simulation
LoD	Level of Detail
MEF	Mean Excess Function
MLE	Maximum Likelihood Estimation
MS	Michelstadt
NRL	Naval Research Laboratory
NSME	Normalized Mean-Square Error
PDF	Probability Density Function
Ph	Phase
QQ	Quantum-Quantum
RANS	Reynolds-Averaged Navier Stokes
RMS	Root Mean Square
RSL	Roughness Sublayer
SxPy	Source x, Point y
TS	Time Series
UCL	Urban Canopy Layer
URANS	Unsteady Reynolds-Averaged Navier Stokes
US	United States
WTC	World Trade Center

List of symbols

Roman symbols

a, b, c, d	constants
A_m	projected area of the model geometry
asct	ascent time
at	arrival time
A_{WT}	cross section of the wind tunnel
C, C	concentration
C_o	observed value
C_p	predicted value
c_v	coefficient of variation
D	diffusion coefficient
dos	dosage
d_s	surface displacement length
dsct	descent time
dT	averaging time
du	duration
f	frequency
Fr	Froude number
g_i	acceleration vector of the field force
H	building height
H_S	source height
I	turbulence intensity
j_{adv}	advective flux
j_{diff}	diffusive flux
j_i	flux
k	turbulence kinetic energy
K_i	turbulent diffusion coefficient
Kn	Knudsen number
L	length
L_{MN}	Monin-Obukov length
lt	leaving time
L_{Ui}	integral length scale
M	mass
n	sample size
p	pressure
pc	peak concentration
p_{he}	pressure in hydrostatic equilibrium

P_i	power product of the dimensional analysis
p_{mod}	modified pressure
pt	peak time
p_δ	longitudinal pressure
Q	flow rate
Q^*	net all wave radiation flux density
Q_E	turbulent latent heat flux
Q_F	anthropogenic heat flux
Q_H	turbulent sensible heat flux
Q_i	physical properties
R^2	coefficient of determination
Re	Reynolds number
$ReSc$	Reynolds-Schmidt product
Ro	Rosby number
R_Q	exemplary quantity
R_T	rate of sources and sinks
Sc	Schmidt number
Str	Strouhal number
t, T	time
t_{di}	time between the release and $i\%$ of the dosage
t_i	timestep
T_{rel}	release duration
T_t	temperature
U	mean longitudinal velocity component
u	threshold of the GPD
u^*	shear velocity
u_i	velocity vector
U_δ	wind speed at δ height
V	released amount
x	longitudinal coordinate
x_i	variables
x_r, y_r, z_r	coordinates of the source location
y	vertical coordinate
z	lateral coordinate
z_0	surface roughness length

Greek symbols

α	constant
β	blockage ratio
δ	boundary-layer thickness
δ_{ij}	the Kronecker delta
δQ_s	net storage heat flux
δT_t	temperature deviation
ε_{ijk}	Levi-Civita permutation tensor
η	Kolmogorov length scale
κ	von Karman constant
λ	length of the molecular mean free path
μ	mean, location parameter
μ_m	dynamic molecular viscosity
ν	kinematic viscosity
ξ	shape parameter
σ	scale parameter
σ^*	modified scale parameter
σ^2	variance
σ_y	horizontal dispersion coefficient
σ_z	vertical dispersion coefficient
τ	time constant
τ_a	arrival time of the short-term releases
τ_{ij}	Reynolds stress tensor
χ_i	characteristic
Ω_j	angular velocity of the rotating Earth

Operators, subscripts and special symbols

$()'$	fluctuation
$()^*$	dimensionless quantity
$()_0$	initial value
$()_{\text{crit}}$	critical value
$()_{\text{FS}}$	full scale
$()_{\text{ref}}$	reference value
$()_{\text{WT}}$	wind tunnel
$\overline{()}$	mean
$\partial()$	partial derivative
$\nabla()$	gradient
$O()$	order of magnitude
$\Delta()$	difference
$\Delta_r()$	relative difference

1 Introduction

1.1 Motivation

Have you ever wondered why you smell the fire in a city, even though the fire fighters already put it out? Or why you can smell it in one street canyon, but not in another? Why is it hard to decide for the fire fighters where to stand to treat an urban fire to avoid being downwind from it? How long does it take until it is safe to return home after a chemical release in the neighborhood? How can the first responders predict the affected area of a hazmat release, and how trustworthy are these predictions? To answer these questions and others alike, this thesis is investigating the dynamics behind gas dispersion in urban environments.

Starting around the 1970s, building aerodynamics and urban dispersion became a popular research topic within fluid mechanics (Balczo, 2015). Hanna (2010) gives an overview of atmospheric dispersion field experiments and their evolution. Although the number of field trials today is comparatively small compared to wind tunnel studies and numerical modeling, looking at the history of field tests gives a good overview of the research development focusing on atmospheric dispersion, which I will present in the next paragraphs based mainly on the extensive summary in the paper of Hanna (2010).

The first field experiments investigating atmospheric dispersion focused on specific issues raised by a single researcher. Richardson (1926) used natural tracers (such as turnips in water) to study diffusion. Roberts (1923) analyzed smoke with optical methods to investigate puff diffusion. Compared to the practice of the following decades, these research projects were not heavily funded. Still, fundamental laws and relations were investigated that provided the basis for today's atmospheric dispersion research.

Later on, mainly throughout the World War II era and during the Cold War, the focus shifted to military applications to study the short-range dispersion of releases from chemical and biological weapons. Another topic of the military research on atmospheric transport and dispersion was the investigation of long range deposition of radiological releases from nuclear weapons.

After the 1960s, environmental issues gained significant attention, environmental agencies were established and laws (such as the US Clean Air Act) were enacted. As a result, the research on air pollution was increasingly funded by governmental bodies and industrial consortiums. Topics including short-range dispersion from stack releases, air pollution in cities, mesoscale transport and dispersion in complex terrains were studied. Regional problems, such as acid rain

or ozone transport became important topics. Nevertheless, field experiments on such large scales are expensive and must involve many groups and instrument systems.

Due to multiple disasters following industrial accidents, such as the Bhopal gas tragedy in 1984 or the Seveso disaster in 1976, the dispersion of hazardous materials from accidental releases received attention. As a result, extensive field tests of dense gas releases were carried out. Hanna et al. (1993) give a summary of eight field measurements from the past century involving heavy gas dispersion with a focus on accidental releases. The paper also lists and evaluates fifteen numerical models, from which some are still in use to model hazmat dispersion.

In recent years, research on atmospheric dispersion includes environmental, public health and military topics. According to Hanna (2010) field tests before the 1960s were used mainly to improve parameterizations in one-or-two-line analytical dispersion models. Nowadays, the field experiments support the evaluation and development of parameterizations in detailed numerical models.

The research presented in this thesis was inspired by and builds on the results of two projects, both dealing with emergency response tools for airborne hazards in built environments. The first one is the COST Action ES1006 European cooperation focusing on the evaluation, improvement and guidance for the use of local-scale emergency prediction and response tools (COST ES1006, 2012). The second project is the CT-Analyst Hamburg II initiative of the University of Hamburg and the US Naval Research Laboratory, carried out for the Behörde für Inneres und Sport in Hamburg with the aim to provide an emergency response tool for the Hamburg Fire Brigade covering the whole area of the city.

1.1.1 COST Action ES1006

The focus of the Action was to evaluate tools and atmospheric dispersion models used in the context of emergency response and to coordinate and harmonize European efforts in threat assessment. The tools and models evaluated by the Action can be categorized into three basic types based on their complexity (see **Table 1.1**).

Table 1.1 Types of emergency response tools and atmospheric dispersion models, based on the integrated flow and/or dispersion modeling approaches (COST ES1006, 2015b).

Model type	Flow modeling approach	Dispersion modeling approach
Type I	models that do not resolve the flow between buildings	Gaussian
Type II	models with diagnostic or empirical flow resolution, but not within the building structures	Lagrangian
Type III	models that resolve the flow between buildings	Eulerian

The documents of the Action (COST ES1006, 2012; COST ES1006, 2015a; COST ES1006, 2015b and COST ES1006, 2015c) provide an extensive review, evaluation, guidance and examples on the use of atmospheric dispersion models for accidental releases in complex

environments. As an example of the results, a test case from the so-called Michelstadt experiments is shown in Figure 1.1. Mean concentration values predicted by different model types are plotted against the reference values from dedicated experiments in a boundary layer wind tunnel. An ensemble mean value over all model results of each type is used for comparison. The closer the points lie to the 45° (1:1) line, the better the predictions are. If a point lies below or above this line, the model is under- or overpredicting the reference data respectively. The results show that with increasing physical complexity of the models, the quality of model predictions improves.

Using Type I models during emergency situations is still common due to the assumption of being conservative (COST ES1006, 2015a). However, the results of the Action do not confirm this assumption (see Figure 1.1.a). The appropriateness of the constraints of the Type I (Gaussian) models for accidental releases in urban environments will be investigated in Chapter 4.1.1 of this thesis.

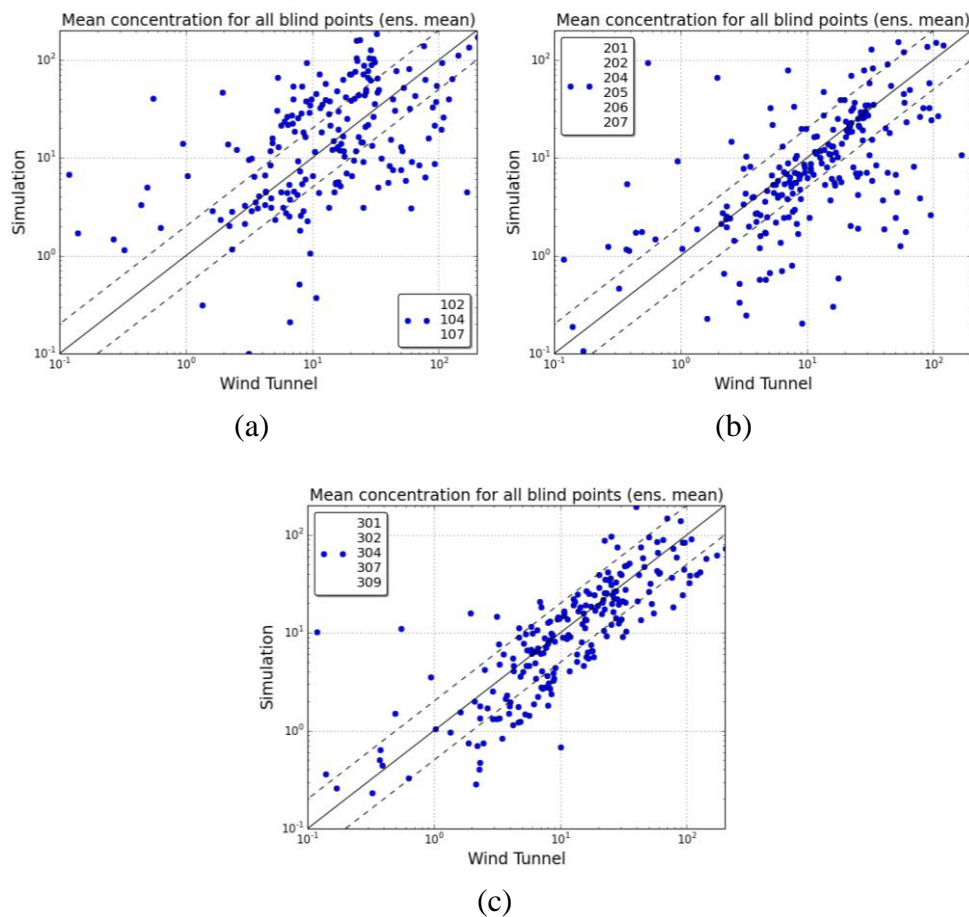


Figure 1.1 Scatter-plots of measured versus ensemble averaged modeled mean concentration values for continuous releases within the Michelstadt blind test case for model Type I (a), Type II (b) and Type III (c). Source: COST ES1006 (2015b)

1.1.2 CT-Analyst Hamburg II project

CT-Analyst is an instantaneous dispersion modeling tool developed by the US Naval Research Laboratory. The three-dimensional flow field behind the dispersion modeling of CT-Analyst is based on detailed urban aerodynamics computations carried out by the FAST3D-CT Large Eddy Simulation (LES) model (Boris, 2002; Cybyk et al., 2001 and Cybyk et al., 1999). The algorithm in FAST3D-CT is documented in Boris et al. (1993) and was substantially modified by Patnaik et al. (2005).

In urban hazmat accidental release scenarios three quarters of direct exposure fatalities are exposed within the first 15 minutes of an event (NRL, 2016). Therefore, time is a key factor in emergency situations. In atmospheric dispersion modeling, usually more complexity means better predictions, but also longer computing time. Normally, a compromise must be made between the accuracy of results and the duration of the simulation. One of the main advantages of CT-Analyst in comparison to other emergency response tools is that it combines the increased performance of an obstacle- and eddy-resolving wind flow model with the speed of a sufficiently accurate but simplified dispersion model called “dispersion nomographs” (Boris et al., 2004). The high-resolution flow field is computed ahead of time with the FAST3D-CT LES code. Relevant wind information is stored in a highly compact database, which can be accessed by CT-Analyst, therefore only the dispersion has to be modeled in case of an accident.

The aim of the project was to expand the already existing CT-Analyst tool of the Hamburg Fire Brigade to cover the whole area of the city. The evaluation and validation of time-dependent features were also part of the project. An example of the evaluation of the contaminant residence time will be shown in Chapter 3.2.60. The data enabled a deeper insight in transient flow and dispersion within the scope of this thesis as well.

1.2 Scope and scientific importance of the thesis

It is not the intention of this thesis and beyond my expertise to provide a numerical or statistical model that would be superior to the existing ones. The aim of this thesis is to raise attention and provide conceptual solutions to some of the problems that are often disregarded while predicting the concentration field resulting from an accidental release in an urban area.

Atmospheric boundary layer wind tunnel measurements were carried out to model gas dispersion in urban areas. Two different model scenarios were investigated: an idealized city structure (Michelstadt) and a part of the city center of Hamburg. During the dispersion measurements tracer gas was released from ground-level point sources. Time-resolved concentration measurements were carried out at numerous locations in the model area. Based on

the experimental results, various questions related to gas dispersion in urban areas are investigated in this thesis.

How does the release duration affect transient dispersion behavior? A release can be categorized as instantaneous (puff), short-term or continuous based on its duration. All three kinds of release durations are investigated in this thesis based on the wind tunnel measurements. A comprehensive method for evaluating and characterizing the measured time series with various release scenarios is presented.

How appropriate is it to model the spatial distribution of the mean concentration with the Gaussian distribution function? Due to their instant results, easy accessibility and application, Gaussian models are often used in emergency situations to predict the spatial concentration distribution. There is a preconception about the Gaussian models that they provide a conservative prediction even in urban geometries, even though the specific model constraints do not apply to such an environment. However, the results of the COST Action ES1006 indicate a different overall model performance. It is investigated in this thesis, whether the Gaussian distribution is a reasonable fit for the mean concentration patterns measured in the wind tunnel.

How to predict high concentrations? Most numerical models applied in emergency situations provide a single mean value for each location, whereas we know from field and wind tunnel tests (and of course from theory) that the temporal variability of turbulence-resolving concentration measurements and the scatter of individually measured concentration values can be quite large. The results in Chapter 4.1.2 show a threefold difference between the mean value and the 95th percentile of the concentration distributions. In emergency situations dealing with accidental gas releases, information about high concentrations is crucial, because the duration of the exposure together with the concentration level determine the dosage affecting individuals. The concentration distributions at the measurement locations are analyzed with extreme value theory to evaluate the probability of high concentrations. Probability density functions are tested to predict the whole frequency distributions as well as high percentiles based only on the mean and the variance.

What is the effect of geometrical modification on the dispersion? The structure of most cities constantly changes due to construction works. If the input data of the numerical models is not updated, these geometrical changes are not taken into consideration. The effect of modifications of the model geometry within the city center of Hamburg on the transient dispersion was investigated in the wind tunnel.

How representative are the predictions based on a simplified geometry? Numerical modeling is often carried out on structured meshes, which results in a simplification of the geometry. A mesh-independency study should be and usually is part of numerical simulation tests. However, if the input geometry is already a simplified model of the city structure, the effect of this simplification will not be present within the mesh-independency test. Within this thesis various stages of simplifications are tested to identify tendencies of the influence on the transient dispersion.

There are questions regarding gas dispersion in urban areas, which are out of the scope of this dissertation. Effects such as the dimension of the source, the density of the tracer gas, chemical reactivity and half-life of the tracer, thermal stratification of the flow, traffic-induced turbulence and the effect of water surfaces on dispersion will not be part of the thesis.

1.3 Structure of the thesis

After the introduction, *Chapter 2* describes the theoretical background of transient flow and dispersion processes in urban environments. The basic assumptions and governing equations are introduced. The time dependency of the flow and concentration field is discussed. The characteristics of urban boundary layers are briefly described.

Chapter 3 presents the methodology applied to generate and evaluate the wind tunnel data sets. The general methods of investigation and characterization of scalar transport in urban environments are discussed with focus on boundary-layer wind tunnel measurements. The two measured data sets are described in detail. Michelstadt is a semi-idealized urban geometry resembling characteristic features of European city centers. The Hamburg data set was measured within a model of parts of the city center of Hamburg. The "Wotan" wind tunnel facility of the Environmental Wind Tunnel Laboratory at the University of Hamburg is introduced. The measurements carried out in each model geometry are described. The representativeness and reproducibility of the experimental results are investigated and documented and the two data sets are summarized. At the end of Chapter 3, the wind tunnel measurements are presented as validation data sets. The usefulness of the data is demonstrated based on examples from the COST Action ES1006 and the CT-Analyst Hamburg II project.

Chapter 4 evaluates the results of the data sets described in the previous chapter. First a statistical analysis is provided of the spatial and frequency distributions of the concentration measured in case of continuous point source releases. The Gaussian plume model and its applicability for urban environments are discussed. Distributions derived from the Gaussian plume model are fitted on the spatial distribution of the measured mean concentration fields. Several probability density functions are investigated according to the goodness of their fit on the measured frequency distributions. The predictability of the extreme concentration based on the frequency distributions is also analyzed. Predictions based on the generalized extreme value distribution and the generalized Pareto distribution are studied. The chapter continues with the analysis of the residence time in various test cases based on short-term release measurements. The effect of geometry simplifications on the transient dispersion was also evaluated for various release durations.

Finally, *Chapter 5* discusses the results and provides a summary and outlook of the thesis.

2 Transient dispersion processes

The definition of the word “*transient*” according to the Oxford English Dictionary (*OED Online*, 2015) is “passing by or away with time; not durable or permanent; temporary, transitory; [...]”. However, in this thesis the term “transient” is defined in a broader sense, involving both *quasi- and non-stationary time-dependent processes* that contribute to scalar transport in an urban environment. To give an example, “transient phenomena of scalar transport” do not only refer to non-stationary features such as short-term emissions or the decay of concentration, but to the fluctuation of a statistically (or quasi-) stationary flow field caused by turbulence as well.

This chapter introduces the basic equations governing transient transport processes and the assumptions that are eligible for urban boundary layer flows. A general description of the flow field and dispersion in urban environments follows, with an emphasis on time dependence.

2.1 Governing equations

The basic assumptions that can be made for scalar transport in an urban environment are introduced in this chapter. The basic hypotheses, physics laws, governing equations and their simplifications are presented. The chapter summarizes the fundamentals of urban dispersion based on the books of Lajos (2008), Batchelor (1967) and Tritton (1988).

2.1.1 Assumptions, simplifications, conventions

In our everyday lives, we observe various phenomena and forms of behavior in the real world (Figure 2.1). We translate these phenomena to our conceptual world by modeling, trying to describe, explain and predict our observations (Dym, 2004). To predict the behavior of a physical system, an appropriate mathematical model describing the phenomena is applied. Assumptions about the properties of the physical system help to specify and simplify general mathematical models.

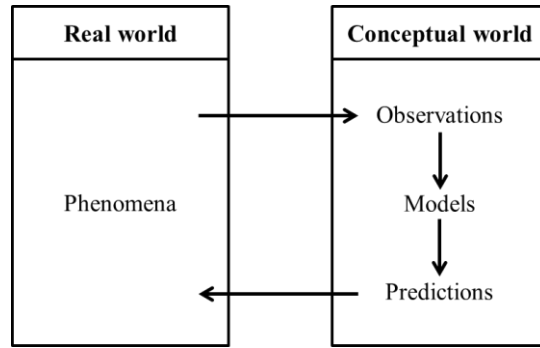


Figure 2.1 The relation between our conceptual models of the world and observations made within the real world (inspired by Dym and Ivey, 1980)

Fluid dynamics is a mathematical model describing the phenomena of fluid motion and therefore applicable to describe the flow field in an urban environment if the underlying assumptions of the mathematical model are met. When applying the equations of fluid dynamics, the continuum hypothesis and the conservation of mass, energy and momentum are assumed.

Continuum

The continuum hypothesis implies that if the length of the molecular mean free path (λ) is significantly lower than the representative length scale (L_{ref}) of a physical phenomenon, the fluid can be treated as a continuous medium rather than as discrete particles. The ratio between L_{ref} and λ is expressed by the *Knudsen number* (Kn). If $Kn \ll 1$, the continuum hypothesis applies.

$$Kn = \frac{\lambda}{L_{ref}} \quad (2.1)$$

For atmospheric flows, the Knudsen number is typically around $O(10^{-9})$, indicating that the fluid can be treated as a continuum, allowing the application of continuum mechanics.

Conservation laws

The conservation laws are fundamental principles of mechanics. They state that the mass, energy and momentum of an isolated system are constant, thus conserved.

Newton's law of viscosity

Newton's law of viscosity holds for the so-called Newtonian fluids. The viscous stress of a Newtonian fluid is proportional to the strain rate by a constant, namely the molecular viscosity (μ_m). The molecular viscosity of a Newtonian fluid depends only on the pressure and the temperature and is not influenced by external forces acting on the fluid.

Incompressible flow

In an incompressible flow, pressure variations do not produce significant changes in the density of the fluid. The density of air (like most fluids) can be assumed constant in space and

time at low flow velocities, given that the pressure and temperature changes are moderate (Lajos, 2008).

Fick's law

Fick's law of diffusion states that the particles move from high-concentration regions to regions of low concentration with a flux proportional to the concentration gradient. The proportionality constant is the diffusion coefficient. Fick's law assumes the conservation of the number of particles, which "can be justified for the transport of tracer particles in a homogeneous medium and in the absence of external forces" for tracers consisting of "non-interacting particles whose motion does not affect the system state" (Milligen et al., 2005).

Since the assumptions of the above described laws and hypotheses hold for scalar transport processes in urban environments, they will be considered throughout the thesis.

Further assumptions

In this thesis, the flow in a local-scale urban environment is assumed to be non-buoyant with no thermal stratification (assuming a neutral atmospheric boundary layer) and the Coriolis force is neglected. The atmospheric boundary layer and the introduced simplifications will be discussed in detail in Chapter 2.2.1.

Conventions

The *Cartesian coordinate system* and the *Eulerian specification* of fluid motion are applied throughout the thesis. Therefore, the velocity vector is represented as $u(x,y,z,t)$, a function of position and time.

The *Einstein summation* convention is applied, meaning that terms are summed over repeated indices. The indicial notation used in this thesis is described by Hopman (2002) in detail.

2.1.2 Transport equation

The transport of a physical quantity can be described by the *transport equation*. The transport equation can be derived from the differential form of the continuity equation

$$\frac{\partial c}{\partial t} + \nabla_i j_i = R_T, \quad (2.2)$$

where c is the amount of the physical quantity over unit volume (such as concentration), j_i is the flux of the quantity and R_T is representing the sources and sinks. The flux can be divided into two parts. The diffusive part can be approximated by Fick's law

$$j_{i,diff} = -D \nabla_i c, \quad (2.3)$$

where D is the diffusion coefficient. The advective part is

$$j_{i,adv} = u_i c, \quad (2.4)$$

where u_i represents the velocity vector.

Substituting Eq. (2.3) and Eq. (2.4) into the differential form of the continuity equation gives the general form of the transport equation:

$$\frac{\partial c}{\partial t} + \nabla_i (u_i c) = \nabla_i (D \nabla_i c) + R_T \quad (2.5)$$

Assuming constant diffusion coefficient, incompressible flow and no sources or sinks, Eq. (2.5) can be simplified:

$$\frac{\partial c}{\partial t} + u_i \nabla_i c = D \nabla_i \nabla_i c. \quad (2.6)$$

Since the number of unknowns (concentration and three velocity components) exceeds the number of equations (Eq. 2.6), further equations are necessary to describe the transport process with a fully determined system of equations.

2.1.3 Continuity and Navier-Stokes equations

Advection (Eq. 2.4) describes the transport mechanism of a quantity driven by fluid motion, causing a velocity-dependence of the transport equation.

The *continuity equation* (Eq. 2.2) applies to the flow field as well. Assuming incompressible flow field, Eq. 2.2 reduces to

$$\nabla_i u_i = 0. \quad (2.7)$$

The *Navier-Stokes equation*, the equation of motion for viscous fluids, can be derived from the conservation of momentum. With the consideration of the prerequisites from Chapter 2.1.1, the Navier-Stokes equation can be reduced to

$$\frac{\partial u_i}{\partial t} + u_j \nabla_j u_i = g_i - \frac{1}{\rho} \nabla_i p + \nu \nabla_j \nabla_j u_i, \quad (2.8)$$

where g_i represents the acceleration vector of the field force acting on the fluid, ρ is the density of the fluid, p is the pressure and ν is the kinematic viscosity.

With the transport, the continuity and the three components of the Navier-Stokes equations, the number of unknowns and the number of equations are both 5, resulting in a fully determined system of equations.

2.2 Origin of time dependence

2.2.1 Flow field

As described in the introduction of Chapter 2, both quasi- and non-stationary time-dependent processes are considered when discussing transient phenomena. The flow can be non-stationary, causing the statistical characteristics (such as the mean velocity) to change with time. However, even a quasi-stationary flow can have time-dependent parameters, for example if the flow is turbulent.

This thesis deals only with quasi-stationary (or ergodic) turbulent flows, meaning that the statistical characteristics of the velocity distribution are independent of time. The non-stationarity is a result of the time-dependence of the concentration field (caused by for example the non-stationary tracer gas release). Since non-stationary flows are not part of this thesis, this chapter only focuses on the fluctuation of the flow field caused by turbulence.

Turbulent flows

As found experimentally by Osborne Reynolds, with increasing *Reynolds-number* (Eq. 2.9) the flow regime changes from laminar to turbulent.

$$\text{Re} = \frac{U_{ref} L_{ref}}{\nu} \quad (2.9)$$

The main characteristics of turbulent flows are *irregularity*, *rotationality*, *diffusivity* and *dissipation*.

Turbulent flows are assumed to be chaotic, making a deterministic description difficult. Therefore, turbulence is normally described statistically.

Turbulent flows are always three-dimensional and have non-zero vorticity. Through the energy cascade of turbulence, the energy of large eddies is transferred to smaller ones. The length scale of the vortices decreases until the kinetic energy of the small-scale structures can be transformed into heat by the fluid's molecular viscosity. This dissipation of energy is caused by the viscous shear stress.

The diffusivity of turbulence causes rapid mixing and redistribution of momentum and scalar quantities. The turbulent diffusion coefficient (analogous to molecular diffusivity) is a phenomenological property describing turbulent diffusion without true physical meaning. The effect of turbulent diffusivity is significantly larger than the effect of the molecular diffusivity for the type of flows discussed here.

The properties of a quasi-stationary turbulent flow, such as the velocity or the pressure, can be divided into a mean and a fluctuating part:

$$u_i = \bar{u}_i + u'_i \text{ and} \quad (2.10)$$

$$p = \bar{p} + p', \quad (2.11)$$

where

$$\bar{x}_i = \lim_{T \rightarrow \infty} \frac{1}{T} \int_0^T x_i dt. \quad (2.12)$$

The mean of the fluctuating part equals zero (Eq. 2.13).

$$\overline{x'_i} = \lim_{T \rightarrow \infty} \frac{1}{T} \int_0^T x'_i dt = 0. \quad (2.13)$$

Therefore, the fluctuations cause a time dependence of the flow characteristics even if the mean characteristics are constant. Due to the complexity and time-dependence of turbulence, the characteristics of the flow cannot be determined analytically. Therefore, Osborne Reynolds derived the Navier-Stokes equation (Eq. 2.8) for temporal averages, the so-called *Reynolds-Averaged Navier Stokes (RANS) equation* (Eq. 2.14).

$$\frac{\partial \bar{u}_i}{\partial t} + \nabla_j \bar{u}_i \bar{u}_j = g_i - \frac{1}{\rho} \nabla_i \bar{p} + \nu \nabla_j \nabla_j \bar{u}_i - \nabla_j \overline{u'_i u'_j} \quad (2.14)$$

In the same manner, the momentum balance equation can be applied for the time-averaged variables (Lajos, 2008). The resulting terms containing the velocity fluctuations are the momentum and normal stresses, which are summarized in the so-called *Reynolds stress tensor* (Eq. 2.15).

$$\tau_{ij} = -\rho \overline{u'_i u'_j} \quad (2.15)$$

Other characteristics describing turbulence are the *turbulence intensity*, the *length and time scale of the turbulent vortices* and the *turbulent kinetic energy* (Lajos, 2008). Turbulence intensity (Eq. 2.16) compares the root-mean-square (RMS) fluctuation to the mean velocity. The turbulent kinetic energy (Eq. 2.17) is the mean kinetic energy acting on a unit mass due to the turbulent fluctuations of the flow field. The turbulence intensity can be converted to the turbulent kinetic energy (Eq. 2.18). The turbulent kinetic energy is frequently characterized by the RMS of the velocity fluctuations.

$$I = \frac{1}{\bar{u}_i} \sqrt{\frac{1}{3} \overline{u'_i u'_i}} \quad (2.16)$$

$$k = \frac{1}{2} \overline{u'_i u'_i} \quad (2.17)$$

$$k = \frac{3}{2} (\bar{u}_i I)^2 \quad (2.18)$$

Atmospheric boundary layer

If a flow is bounded by a surface with no slip condition, the velocity of the flow along this boundary will be zero. In the vicinity of the surface, the velocity of the flow increases perpendicular to the boundary until it reaches the velocity of the bulk flow. The boundary layer is the layer near the surface, where the velocity increases perpendicular to the surface and the effect of friction is significant. Depending on the Reynolds number, a boundary layer can be laminar or turbulent. However, even in case of a turbulent boundary layer, the presence of the wall prevents the formation of vortices at the surface. Therefore, a *laminar (a.k.a. viscous) sublayer* is present at the direct vicinity of the wall, where the viscous forces are dominant.

The *atmospheric boundary layer (ABL)* is the boundary layer between the surface of the Earth and the free atmosphere. The surface of the Earth has a no-slip condition. The *geostrophic wind* in the free atmosphere is driven by the pressure gradient caused by the non-uniform global thermal energy distribution. The ABL flow generally has a high Reynolds number ($Re \sim 10^8$). Therefore, the boundary layer is turbulent with a $O(10^{-2} \text{ m})$ or even thinner viscous sublayer at the direct vicinity of the surface.

To describe the flow field of the ABL (Eq. 2.19), the *Coriolis effect*, an inertial force that causes the deflection of the path of an object in motion relative to a rotating coordinate system, appears in the Navier-Stokes equations (Eq. 2.8.), and the term describing the force field is expanded with the *buoyancy effect* (Snyder, 1981).

$$\frac{\partial u_i}{\partial t} + u_j \nabla_j u_i = \frac{g_i}{T_{ref}} \delta T_t \delta_{3i} - 2\varepsilon_{ijk} \Omega_j u_k - \frac{1}{\rho} \nabla_i p + \nu \nabla_j \nabla_j u_i \quad (2.19)$$

The term $-2\varepsilon_{ijk} \Omega_j u_k$ describes the Coriolis effect, where Ω_j is the angular velocity of the rotating Earth and ε_{ijk} is the Levi-Civita permutation tensor. Due to the low rotation rate of the Earth, the Coriolis force becomes significant only over large distances.

The buoyancy effect (Snyder, 1981) is determined by the deviation of the temperature (δT_t) from the temperature of a neutral atmosphere (T_t). T_{ref} is the reference value of the temperature and δ_{ij} is the Kronecker delta.

The ABL can be divided into sublayers (Figure 2.2). The results of this thesis, as most boundary-layer wind tunnel measurements, are applicable for the *Prandtl layer* of the ABL during *neutral stratification*. In the Prandtl layer the flux is assumed to be constant in vertical direction and the Coriolis effect is negligible at local scale $O(10^3-10^4 \text{ m})$. In a neutrally stratified atmosphere the vertical potential temperature gradient is close to zero, which allows neglecting the buoyancy effect in Eq. 2.19. Therefore Eq. 2.8 can be used to characterize the flow field in a neutrally stratified Prandtl layer at micrometeorological scales.

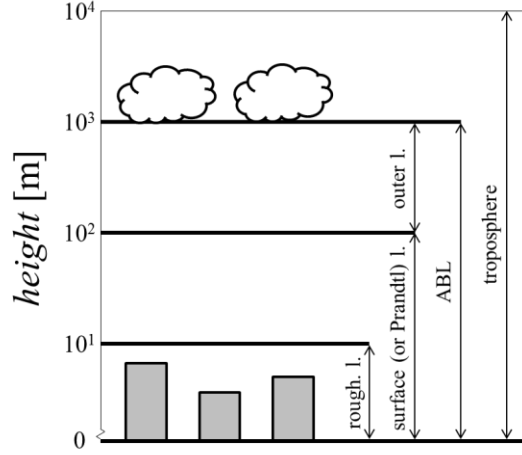


Figure 2.2 Schematic of the planetary boundary layer (based on Arya, 2001 and Hertwig, 2013). The heights are more typical for neutral stability and they are highly variable in space and time.

Urban boundary layer

Cities have a significant effect on the flow field of the atmospheric boundary layer. The city geometry causes a drag force on the flow field, an increase in the heat-storage of the surface and a decrease in evapotranspiration. The urban energy balance (Oke, 1982) can be written as

$$Q_* + Q_F = Q_E + Q_H + \Delta Q_S, \quad (2.20)$$

where Q_* is the net all wave radiation flux density, which consists of the incoming shortwave and longwave radiation. Q_F is the anthropogenic heat flux, Q_H is the turbulent sensible heat flux, Q_E is the turbulent latent heat flux and ΔQ_S is the net storage heat flux (Grimmond et al., 2011).

The urban boundary layer, similarly to the ABL, can be divided into vertical layers (Grimmond and Oke, 2002). The layer closest to the ground is the urban canopy layer (UCL). The flow field in the UCL is directly influenced by the local building geometry. The UCL is the lower part of the roughness sublayer (RSL). Above the UCL within the RSL, the flow field is still highly inhomogeneous and strongly affected by the city structure. Above the RSL is the inertial sublayer (ISL). In the ISL the flow field is spatially homogeneous, the effect of the individual buildings cannot be observed anymore (Grimmond and Oke, 1999).

The vertical profile of the mean wind velocity in a neutral boundary layer can be described by a logarithmic function (Eq. 2.21) derived from Prandtl's mixing length theory (Lajos, 2008).

$$\frac{u(z)}{u_*} = \frac{1}{\kappa} \ln \left(\frac{z - d_s}{z_0} \right) \quad (2.21)$$

To ensure the applicability of the Monin-Obukov similarity theory, an additional term is introduced to the logarithmic wind profile, which contains a universal dimensionless function with variables z and L_{MN} , the Monin-Obukov length. The Monin-Obukov similarity theory describes the velocity and temperature profiles for non-neutral conditions. However, due to

several physical effects the stability over urban areas is forced toward neutral conditions (Britter and Hanna, 2003), therefore Eq. (2.21) describes the vertical mean wind profile appropriately in most cases.

In Eq. (2.21) u_* is the shear velocity, κ is the von Karman constant, d_s is the surface displacement length and z_0 is the surface roughness length (Britter and Hanna, 2003). There are multiple approaches to estimate d_s and z_0 . Table 2.1 and Table 2.2 present exemplary values of d_s and z_0 taken from the paper of Britter and Hanna (2003) and VDI 3783/12 (2000).

Table 2.1 Surface roughness length data for different urban and industrial categories (Britter and Hanna, 2003).

Category	Roughly open	Rough	Very rough	Skimming	"Chaotic"
z_0 [m]	0.1	0.25	0.5	1	2
Distance between obstacles	20H	12H	3-7H	Densely built-up area without much obstacle height variation.	City centers with mixture of low-rise and high-rise buildings.

Table 2.2 Surface roughness lengths and surface displacement length for different surfaces (VDI, 2000)

Category	Slightly rough	Moderately rough	Rough	Very rough
z_0 [m]	$10^{-5} - 5 \cdot 10^{-3}$	$5 \cdot 10^{-3} - 0.1$	0.1 - 0.5	0.5 - 2
d_s [m]	0	0	0.75H	0.75H
Description	ice, snow, water surface	grassland, farmland	park, suburban area	forest, inner-city area

The enhanced drag due to the urban geometry causes momentum loss of the flow field. This results in intensified turbulent fluxes above the urban canopy and increases the turbulence compared to flows above flat-open terrain (Hertwig, 2013). Typical vertical turbulence intensity profiles for different surface roughness categories can be found in ESDU (1985).

2.2.2 Transport and dispersion

The transport of a physical quantity is described by the transport equation (Eq. 2.5), which was introduced in Chapter 2.1.2. Assuming a constant diffusion coefficient, the time dependent variables in Eq. (2.5) are the velocity (u_i) and the term representing sources and sinks (R_T). Similarly to the other characteristics of a quasi-stationary turbulent flow (see Chapter 2.2.1), the concentration can also be divided into a mean and a fluctuating part (Fischer, 2011):

$$c = \bar{c} + c'. \quad (2.22)$$

If Eq. (2.22) is substituted into Eq. (2.5), the averaged transport equation can be derived, as the RANS equation (Eq. 2.14) was derived by averaging the Navier-Stokes Equation in Chapter 2.2.1:

$$\frac{\partial \bar{c}}{\partial t} + \bar{u}_i \nabla_i \bar{c} = D \nabla_i \nabla_i \bar{c} + R_T - \nabla_i \overline{u'_i c'}. \quad (2.23)$$

In Eq. (2.23), the term $\bar{u}_i \nabla_i \bar{c}$ is the *advective transport* driven by the mean velocity. The term of the *molecular diffusion* of the mean concentration is $D \nabla_i \bar{c}$, and $\overline{u'_i c'}$ is the *turbulent diffusion* of the concentration. The turbulent diffusion can be expressed with the mean concentration, using the turbulent diffusion coefficient, K_i [m²/s] (Etling, 2008):

$$\overline{u'_i c'} = -K_i \nabla_i \bar{c}. \quad (2.24)$$

Following the outline of Etling (2008), the averaged transport equation will be simplified and solved for different release scenarios in the sections below.

Solution of the averaged transport equation for continuous releases from point sources

In case of a continuous release, the release duration is constant and theoretically infinite (see Chapter 3.1.3). In case of a continuous release, the following assumptions can be made for the transport equation:

1. $D \ll K_i$, the molecular diffusion can be neglected,
2. $\nabla_i K_i = 0$, assuming homogeneous turbulence,
3. $R_T = 0$, there are no additional sources or sinks,
4. $\bar{u}_x(x_i, t) = U$, $\bar{u}_y = \bar{u}_z = 0$, where U is constant,
5. $\frac{\partial \bar{c}}{\partial t} = 0$, the concentration field is stationary.

Considering the assumptions listed above, the transport equation for continuous releases can be simplified to

$$U \frac{\partial \bar{c}}{\partial x} = K_i \nabla_i \nabla_i \bar{c}. \quad (2.25)$$

To solve Eq. (2.25), another assumption can be made:

6. $|K_x \nabla_i \nabla_i \bar{c}| \ll \left| U \frac{\partial \bar{c}}{\partial x} \right|$, downwind diffusion is negligible compared to the advection.

With the previous assumptions, the solution of Eq. (2.25) is

$$\bar{c}(x, y, z) = \frac{Q}{4\pi x \sqrt{K_y K_z}} \exp \left[-\frac{U}{4x} \left(\frac{y^2}{K_y} + \frac{(z - H_s)^2}{K_z} \right) \right], \quad (2.26)$$

for a point source located at $(0, 0, H_s)$. According to Eq. (2.26), at each x location downwind from the source the concentration has a two-dimensional Gaussian distribution on the y - z plane. The one-dimensional Gaussian (or normal) distribution has the general form:

$$G(y) = \frac{1}{\sqrt{2\pi\sigma^2}} \exp \left(-\frac{(y - \mu)^2}{2\sigma^2} \right), \quad (2.27)$$

where μ is the mean and σ^2 is variance of the distribution. To convert Eq. (2.26) to the form of the Gaussian distribution, the following substitutions can be done:

$$\sigma_y = \sqrt{2K_y \frac{x}{U}} \quad (2.28)$$

$$\sigma_z = \sqrt{2K_z \frac{x}{U}} \quad (2.29)$$

The resulting equation (Eq. 2.30) is the equation of the so-called *Gaussian plume model*, which is often used to predict the concentration field above flat-open terrain or above homogeneous roughness resulting from a continuous release.

$$\bar{c}(x, y, z) = \frac{Q}{2\pi\sigma_y\sigma_zU} \exp\left[-\frac{y^2}{2\sigma_y^2} - \frac{(z - H_s)^2}{2\sigma_z^2}\right]. \quad (2.30)$$

Once the plume reaches zero height, it is reflected from the ground. This reflection is not taken into consideration by Eq. (2.30). The Gaussian plume model and its applicability in urban environments will be discussed in Chapter 4.1.1, where the reflection of the ground will be considered in Eq. 4.1.

Solution of the averaged transport equation for puff releases from point sources

The duration of a puff (or instantaneous) release, such as an explosion, is infinitesimally small. The characteristics of puff releases are discussed in detail in Chapter 3.1.3.

The assumptions 1-3 from those introduced for the continuous releases in the previous chapter (see page 16) apply to puff releases as well. There is a fourth assumption, which can be made for puff releases:

4. $u_i = 0$, the coordinate system is moving with the mean flow.

Considering the assumptions, the transport equation for a puff release can be simplified to

$$\frac{\partial \bar{c}}{\partial t} = K_i \nabla_i \nabla_i \bar{c}. \quad (2.31)$$

Eq. (2.31) is also known as Fick's Second Law, which implies that the concentration field is determined by the diffusion terms only. Substituting $t=x/U$ into Eq. (2.31) results in the averaged and simplified transport equation derived for continuous releases (Eq. 2.25). At each distance from the source (Δx_m), the concentration distribution of a continuous release can be modeled with the simplified transport equation of puff releases by substituting $\Delta x_m = Ut_m$ (Etling, 2008).

By fixing the release location (x_r, y_r, z_r) and the released amount, Q at $t=0$, Eq. (2.31) can be solved analytically:

$$\bar{c}(x, y, z, t) = \frac{Q}{\sqrt{(4\pi t)^3} \sqrt{K_x K_y K_z}} \exp\left[-\frac{(x-x_r)^2}{4K_x t} - \frac{(y-y_r)^2}{4K_y t} - \frac{(z-z_r)^2}{4K_z t}\right]. \quad (2.32)$$

Eq. (2.31) shows that the spatial distribution of the concentration can be described by an exponential function in each direction. The derivation of the Gaussian puff model introducing further assumptions to Eq. (2.31) can be found in several text books and review articles, such as Hanna et al. (1982), Etling (2008) or Stockie (2011).

3 Methodology

Small-scale modeling will be introduced in this chapter focusing on flow and concentration measurements in boundary-layer wind tunnels. The wind tunnel model geometries will be introduced and the evaluation method to investigate transient transport processes is discussed. At the end of the chapter, the resulting data sets are summarized.

Approaches to investigate transport and dispersion in urban environments

The ability of producing an exact prediction of the transient concentration field in an urban environment is a challenge not yet accomplished due to the complexity of the phenomena. Experimental and mathematical approaches exist to examine physical processes in the atmosphere.

In situ (full-scale or field) measurements can grasp the complexity of the processes. On the other hand, the costs of field tests tend to be high and the inherent fluctuations of the flow field and boundary conditions result in poor statistical representativeness (Schatzmann et al., 2000).

Mathematical and physical *modeling* of atmospheric transport reduces the degrees of freedom of the problem by simplifying the phenomena (Petersen, 2013). The analytical solution of the *mathematical models* involving the set of governing equations introduced in Chapter 2.1 is yet to be found for boundary conditions typical for atmospheric flows. Therefore, numerical methods are developed to estimate the solution of these models. *Physical modeling* can be a small-scale field measurement (such as in Macdonald, 1998) or a wind tunnel experiment.

Why wind tunnel?

Unlike field experiments, during wind tunnel measurements the mean boundary conditions determining the transport and dispersion phenomena can be controlled. Consequently, the statistical representativeness of the data can be adjusted to the demands of the problem, and the effect of precise systematic variations of the boundary conditions can be investigated separately. On the other hand, wind tunnel modeling is a simplification of the case measured *in situ*.

Another advantage of wind tunnel experiments is the similarity of the dimensional governing equations to those in full scale, scaled by similarity parameters. Careful adjustments and testing is still required to ensure similarity to full-scale conditions (see Chapter 3.1.1). Numerical models developed for atmospheric processes on the other hand are based on assumptions, which must be case-specifically validated with proper data. The advantage of numerical simulations is the volumetric data-coverage, which is rather difficult to achieve in the wind tunnel.

Bearing the advantages and disadvantages in mind, I decided to base my research on wind tunnel data. The majority of the results included in this thesis requires the beneficial properties of wind tunnel measurements. Statistical characteristics are investigated to characterize local-scale transient processes, therefore the statistical representativeness of the results is crucial. Controlling and systematically changing the boundary conditions, such as geometrical modifications or changing the release duration, were extensively investigated.

3.1 Measurement and characterization of scalar transport in urban environments

3.1.1 Requirements of small-scale modeling

The purpose of small-scale modeling is to acquire information about the full-scale process. Therefore, small-scale modeling requires *similarity* between the modeled process and the model itself. Two transport processes are similar, if the functions describing velocity, pressure and concentration in space and time are similar. To ensure the similarity of the functions, two requirements must be fulfilled. One necessary condition is the *similarity of the partial differential equations* characterizing the processes in model and full scale. The other necessity is the *similarity of the initial and boundary conditions* (Lajos, 2008).

If the non-dimensional forms of two equations are equal, then the dimensional equations are similar. Nondimensionalizing the governing equations by introducing appropriate reference values produces *dimensionless parameters* characteristic for the process investigated. If these dimensionless parameters are equal for the model and the full-scale problems, then the dimensionless governing equations will also be the same.

The simplified dimensional governing equations characterizing transport and dispersion processes in urban environments (the transport equation, the continuity and the Navier-Stokes equation, Eq. 2.6, 2.7 and 2.8) can be nondimensionalized by the reference values of concentration C_{ref} , length scale L_{ref} and velocity U_{ref} . Introducing the following dimensionless variables, the non-dimensional equations can be derived:

$$c^* = \frac{c}{C_{ref}}; t^* = t \frac{U_{ref}}{L_{ref}}; x_i^* = \frac{x_i}{L_{ref}}; u_i^* = \frac{u_i}{U_{ref}}; p^* = \frac{p}{\rho U_{ref}^2}$$

If a fluid with constant density fills the flow field completely, the Navier-Stokes equation for the fluid in hydrostatic equilibrium will be

$$0 = g_i - \frac{1}{\rho} \nabla_i p_{he}, \quad (3.1)$$

where p_{he} is the pressure in hydrostatic equilibrium (Lajos, 2008). When subtracting Eq. (3.1) from Eq. (2.8), the Navier-Stokes will have the form

$$\frac{\partial u_i}{\partial t} + u_j \nabla_j u_i = \frac{1}{\rho} \nabla_i p_{mod} + \nu \nabla_j \nabla_j u_i, \quad (3.2)$$

where $p_{mod} = p - p_{he}$ is the modified pressure, including the effects of the field force acting on the fluid.

The non-dimensional, simplified Navier-Stokes equation will then be

$$\frac{\partial u_i^*}{\partial t^*} + u_j^* \nabla_j^* u_i^* = -\nabla_i^* p_{mod}^* + \frac{\nu}{U_{ref} L_{ref}} \nabla_j^* \nabla_j^* u_i^*, \quad (3.3)$$

where

$$\nabla_i^* \equiv \frac{\partial}{\partial x_i^*}. \quad (3.4)$$

The non-dimensional transport equation (Eq. 3.5) can be derived from Eq. (2.6).

$$\frac{\partial c^*}{\partial t^*} + u_i^* \nabla_i^* c^* = \frac{D}{L_{ref} U_{ref}} \nabla_i^* \nabla_i^* c^* \quad (3.5)$$

Dimensionless parameters

The non-dimensional equations describing the small- and full-scale processes will be the same, if the parameters occurring in the equations are equal.

The parameter of the non-dimensional simplified Navier-Stokes equation¹ (Eq. 3.3) is the *Reynolds number*

$$\text{Re} = \frac{U_{ref} L_{ref}}{\nu}. \quad (3.6)$$

The parameter of the non-dimensional transport equation (Eq. 3.5) is the *Reynolds-Schmidt product*

¹ Without the assumptions of neutral stratification and negligible Coriolis force and buoyancy forces, the Rossby number

$$\text{Ro} = \frac{U_{ref}}{L_{ref} \Omega_{ref}},$$

where Ω_{ref} is the reference angular velocity, and the Froude-number

$$\text{Fr} = \frac{U_{ref}}{\sqrt{g L_{ref}}}$$

would also appear in the non-dimensional Navier-Stokes equation.

$$\text{Re Sc} = \frac{U_{ref} L_{ref}}{D} \quad (3.7)$$

Due to the large-scale differences, reaching Reynolds-number equality between full scale and wind tunnel scale demands unfeasibly high-speed flow where compressibility cannot be neglected anymore. The *Reynolds-number independence* hypothesis introduced by Townsend (1956) based on Kolmogorov's hypotheses (Kolmogorov, 1991) states that if thermal and Coriolis effects are negligible, the turbulent flow structure is self-similar above a critical Reynolds number, Re_{crit} (Snyder, 1981). However, there are two phenomena that are Reynolds-number dependent even above Re_{crit} : the very small-scale, *dissipative eddies* and the *viscous (laminar) sublayer* close to the surfaces.

The effect of the viscous sublayer on the bulk turbulent flow is negligible and the size of the sublayer can be decreased using aerodynamically rough-surfaced models.

The decreasing Reynolds number decreases the width of the turbulent energy spectrum (I/η) by cutting the spectral range of the high-frequency side of the spectrum, while the integral-scale eddies change only very slowly until the Reynolds number reaches Re_{crit} . The reduction of the Kolmogorov length scale can be quantified by Eq. (3.8) according to Snyder (1981). Nonetheless, the Kolmogorov scales of wind tunnel measurements are typically significantly smaller than the eddies considerably contributing to the spread of the contaminant at full scale.

$$\frac{\eta_{FS}}{\eta_m} \approx \left(\frac{L_{FS}}{L_m} \right)^{\frac{1}{4}} \quad (3.8)$$

To set the Reynolds-Schmidt product equal to full-scale conditions in the wind tunnel is also difficult – mainly because of the presence of the Reynolds-number within the formula. The Schmidt number is a property of the fluid, representing the ratio of the momentum diffusivity and the mass diffusivity. Most gases dispersing in air have Schmidt numbers close to one (Snyder, 1981). Therefore, keeping the Schmidt number close to its full-scale value in a wind tunnel measurement can be generally satisfied. The difficult part is again matching the Reynolds number. Similar to the Reynolds-number independence theory, with certain restrictions, if the Reynolds number is high enough, the equality of the Reynolds-Schmidt product between the scales can be disregarded. Above a critical Reynolds number “molecular diffusion will contribute very little to the bulk contaminant transfer; its main function is to smooth out the very small-scale discontinuities of concentration” (Snyder, 1981).

Boundary conditions

Due to the limited knowledge about the differential equations describing the transport and dispersion in the atmosphere, it is impossible to specify, which boundary conditions are necessary to make the problem determinate (Batchelor, 1953). However, even the information about the boundary conditions certainly needed to be identified for determination (such as the

concentration values at the initial time at the whole fluid and at all spatial boundaries as the function of time) is never available from the full-scale case. Still, following case-specific requirements, (limited) similarity to full-scale conditions can be achieved.

The investigated problem defines the boundary conditions and the degree of strictness of the similarity necessary throughout the wind tunnel measurements. To analyze the processes in urban environments, taking into consideration the assumptions made in Chapter 2.1.1, the similarity of the *geometry* and the *pressure, velocity and concentration field* must be fulfilled. Guidelines such as VDI 3783/12 (2000) and the handbook of Snyder (1981) give general guidance to achieve these similarities. To ensure geometrical similarity, the measurements are carried out on a small-scale model of the investigated geometry. The similarity of the pressure and the velocity field is achieved by geometrical similarity, Reynolds number independent flow field and the similarity of the inflow profile to ensure that the model-scale and full-scale initial and boundary conditions of the non-dimensional Navier-Stokes equations (Eq. 3.3) are the same. Furthermore, minimized longitudinal pressure gradient in the wind tunnel and sufficiently low blockage ratio needs to be achieved in the wind tunnel in order to simulate full scale flow conditions. The *blockage ratio* (β) is the ratio between the projected area of the model geometry with a vector parallel to the main wind direction (A_m) and the cross section of the wind tunnel (A_{WT}), (VDI 3783/12, 2000):

$$\beta = \frac{A_m}{A_{WT}} . \quad (3.9)$$

The concentration field similarity is assured by the similarity of the model geometry (including the geometry of the source) and the flow field, Reynolds number independent concentration field and similarity of the flow rate and release duration.

3.1.2 Concentration measurements in a boundary-layer wind tunnel

The aim of the measurements defines the experimental procedure. The aim of this thesis is to characterize the phenomena of scalar transport in urban areas during accidental releases. The measurements were therefore carried out in a wind tunnel specifically intended to model atmospheric flows. The scalar transport of a gas was characterized based on the results of concentration measurements. Investigating both the quasi-stationary and the time-dependent concentration field gives a detailed picture of scalar transport in urban environments.

Boundary-layer wind tunnel

Boundary-layer wind tunnels are specifically designed to model atmospheric flow and transport phenomena. Figure 3.1 shows the open-return-, suction-type boundary layer wind tunnel with a closed test section of the Environmental Wind Tunnel Laboratory in Hamburg. The air enters the wind tunnel on the left side of Figure 3.1. It flows through the intake nozzle with a honeycomb and the contraction section. These sections lower the turbulence intensity and the

velocity gradients by homogenizing the incoming flow. After the contraction, at the beginning of the approach flow section, so-called spires are used for pre-shaping the desired wind velocity profile and for generating large-scale vortices. Along the approach flow section, roughness elements on the wind tunnel floor produce small-scale vortices and drag similar to full-scale surface roughness on the inflow. The spires and the roughness elements together establish the velocity and turbulence profile of the approach flow. The scale model of interest is placed into the test section, where the measurements are carried out. The ceiling of the boundary-layer wind tunnel is adjustable to compensate for aerodynamic blockage introduced by the model and minimize the longitudinal pressure gradient in the test section. The air exits the wind tunnel through a fan with diffusor, which is driving the wind tunnel flow.

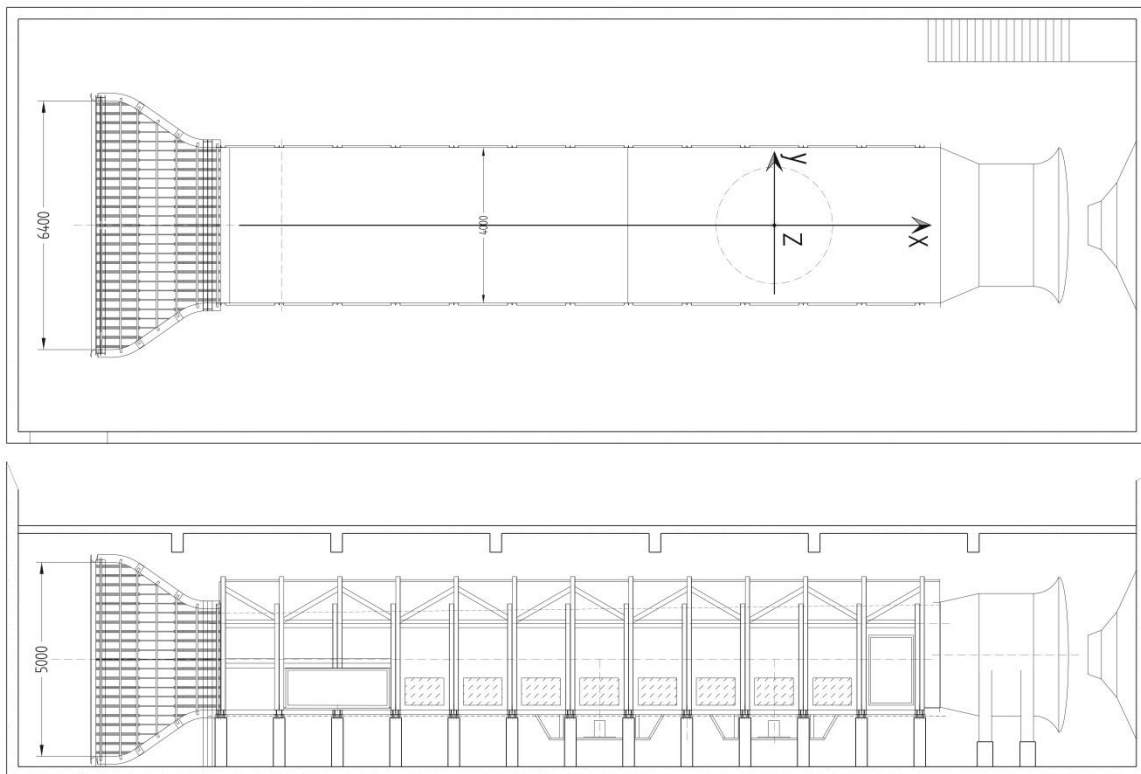


Figure 3.1: Sketch of the Wotan boundary-layer wind tunnel (Harms, 2010)

Capturing transient phenomena of scalar transport in the wind tunnel

Wind tunnel data needs to satisfy two basic criteria to be qualified for characterizing transient phenomena. It must be *statistically representative of the investigated scenario* and it must have *sufficient temporal resolution* to acquire the characteristics of time dependence.

To be representative of the investigated scenario, the requirements introduced in Chapter 3.1.1 have to be fulfilled. To ensure the statistical representativeness of the results, the boundary conditions have to be quasi-stationary providing constant mean flow and concentration fields throughout the measurement. Under quasi-stationary conditions, the statistical representativeness

of the results can be improved with longer continuous release measurements and larger ensemble size of the puff releases (see Chapter 3.2.4).

The temporal resolution of the measurements depends on the model scale and the measurement device. There are several devices to measure the flow and concentration field with high resolution. The data in this thesis were measured using *Laser Doppler Velocimetry (LDV)* (Durst et al., 1976) to capture the velocity and *fast-Flame Ionization Detection (fast FID)* (Cheng et al., 1998) to record concentration time series. Both devices take single-point measurements with sufficiently high temporal resolution to evaluate the statistical measures of the characteristics of transient dispersion described in Chapter 3.1.3 and 3.1.4.

To simulate scalar transport, a “source term” is needed (Eq. 2.5). The spatial dimension of the tracer gas source (point, line, area or volume) and the release duration (from instantaneous to continuous) is chosen based on the phenomena of interest. Accidental releases in urban areas are usually local sources of limited extent. Therefore, modeling them as point sources gives a good estimate of the phenomena. However, the concentration and flow field in the direct vicinity of the source is only transferable to full scale if the dimensionless geometry and initial velocity of the release is the same in model scale. During the measurements for this thesis, point sources with *negligible initial momentum* were mounted in the urban areas to model accidental releases. *Continuous, short-term* and *instantaneous (puff) releases* were measured. Figure 3.2 exemplarily shows parts of measured concentration time series of a continuous release and a repetitive instantaneous release measurement. During the continuous release measurement (Figure 3.2.a) the trigger signal of the tracer gas release is constant, indicating a steady flow rate of the measurement gas. During short-term release and puff measurements (Figure 3.2.b), the source is only open for a short time resulting in a non-stationary concentration field.

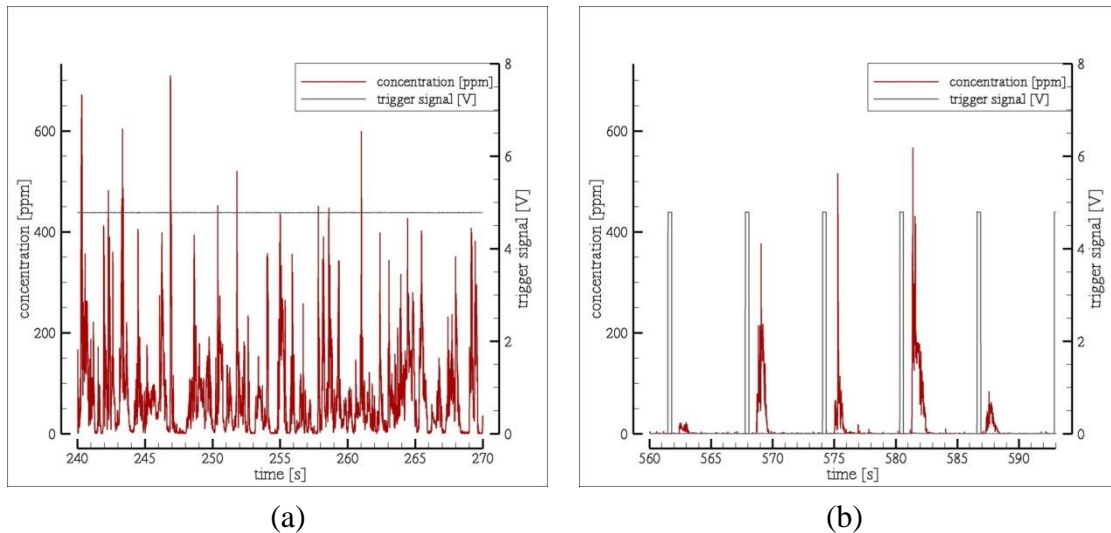


Figure 3.2 Parts of concentration time series of a continuous release (a) and a puff release (b) measurement. Results are in model scale.

3.1.3 Characteristic parameters of dispersion

This chapter introduces the parameters used for describing continuous, puff and short-term releases. To produce scale-independent results, non-dimensional parameters can be applied. The non-dimensional forms of the parameters can be derived by nondimensionalizing the governing equations (see Chapter 3.1.1) or via dimensional analysis. Besides deriving the non-dimensional parameters, the similarities and differences between the characteristics of the three release scenarios are also described.

Continuous release measurements

To achieve and acquire quasi-stationary concentration fields, the release flow rate is kept constant during a continuous release measurement. Hence, the fluctuation of the concentration field is a result of the turbulent flow field. Therefore, time is only considered as a measure of the frequency of occurrence of characteristic events and not as an independent variable. In case of continuous releases the aim of the measurements is to identify the statistics of the concentration time series, such as the mean and extreme values.

For achieving generalized results independent from scale and boundary conditions, the measured concentration was converted to dimensionless values determined from the transport equation. Assuming constant diffusion coefficient and incompressible flow considering the term of sources and sinks, Eq. (2.5) can be simplified:

$$\frac{\partial c}{\partial t} + u_i \nabla_i c = D \nabla_i \nabla_i c + R_T. \quad (3.10)$$

Eq. (3.10) can be nondimensionalized in a similar manner to Eq. (3.5), using L_{ref} , C_{ref} and U_{ref} .

$$\frac{\partial c^*}{\partial t^*} + u_i^* \nabla_i^* c^* = \frac{D}{L_{ref} U_{ref}} \nabla_i^* \nabla_i^* c^* + \frac{R_T L_{ref}}{C_{ref} U_{ref}} \quad (3.11)$$

In case of a continuous release from a point source with negligible initial velocity compared to the wind velocity around the source, with Q flow rate, the source term can be written as

$$R_T = \frac{Q}{L_{ref}^3}, \quad (3.12)$$

Substituting Eq. (3.12) into Eq. (3.11), the *dimensionless concentration* can be defined based on the last term of the right-hand side:

$$C^* = \frac{c U_{ref} L_{ref}^2}{Q}, \quad (3.13)$$

where c is the measured concentration to be nondimensionalized.

Puff release measurements

To investigate the non-stationary concentration field, “very short-term” releases (0.3 s release duration at model scale) were measured to model instantaneous (puff) releases. In this case not only concentration statistics, but the *duration between specific events* (such as the time between release and signal detection) can also be evaluated.

Defining the time of the occurrence of a characteristic event, such as the arrival time or the leaving time of a puff at a measurement location, is not straightforward. A detailed literature review on puff analysis can be found in Berbekar et al. (2015a). The most common practice to define the characteristic times is to set a threshold criterion. The puff is considered to be present at the measurement location, when the concentration is exceeding the chosen threshold.

In this thesis, the puffs are considered as *instantaneous* releases, and the release duration, T_{rel} is assumed to be infinitesimal, as the release duration is significantly shorter than the phenomena governing the tracer transport. The effect of release duration on the puff characteristics is investigated in Chapter 3.1.3.

The *dosage-based criterion* introduced by Harms (2010) was shown to be appropriate for instantaneous releases (Berkar et al., 2015a) and therefore is applied throughout this thesis. The dosage (dos [ppm · s], Eq.3.14) of a puff at a certain measurement location is the integral of the concentration (c [ppm], given in parts per million by volume) measured at a location over time (t [s]):

$$dos = \int_0^T c(t) dt, \quad (3.14)$$

where T represents the end of the measurement (detection period) after the cloud of material has left the measurement location (Figure 3.3).

Apart from the peak time, all characteristic times of the puff depend on the dosage-based criterion. Choosing the 5% and the 95% of the dosage as relative thresholds for the presence of the puff, the following parameters can be defined (Harms, 2010):

- dosage (dos [ppm · s]): the time-integrated concentration of tracer gas over the detection period,
- peak concentration (pc [ppm]): the highest concentration for the minimum available instrument resolution occurring at the measurement location during the detection period,
- arrival time (at [s]): the time between the beginning of the puff release and when 5% of the total dosage of the puff has reached the measurement location,
- peak time (pt [s]): the time between the beginning of the puff release and when the peak concentration occurs at the measurement location,
- leaving time (lt [s]): the time after the beginning of the puff release when 95% of the total observed dosage of the puff is recorded at the measurement location,

- ascent time ($asct$ [s]): the time interval between the arrival time and the peak time,
- descent time ($dsct$ [s]): the period between the peak time and the leaving time,
- duration (du [s]): the time interval between the arrival time and the leaving time.

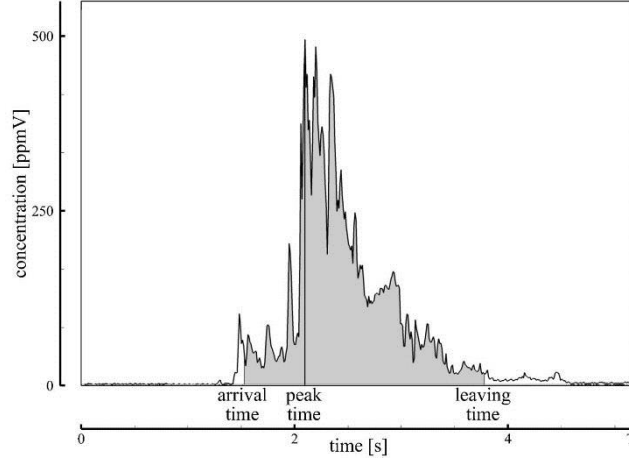


Figure 3.3 The peak time and the dosage-based arrival time and leaving time indicated in a puff measurement time series. (Based on Figure 4 in the paper of Berbekar et al., 2015a).

Dimensional analysis (Buckingham, 1914) according to Rayleigh’s method (Mendoza, 1994) was applied to gain the conversion factors for the dosage-based puff parameters to obtain dimensionless values. If f is a function of the physical properties Q_1, Q_2, \dots, Q_m , forming a homogeneous equation, it can be rearranged as

$$f \propto Q_1^a Q_2^b \cdots Q_m^h, \quad (3.15)$$

where a, b, \dots, h are constant exponents. If the relation

$$Q_i = \alpha \prod_{j=1, j \neq i}^{m-1} Q_j^{R_{ji}}, \quad (3.16)$$

exists with Q_1, Q_2, \dots, Q_m forming a homogeneous equation involving n physical fundamental dimensions, then the power product relation

$$P_i = \alpha \prod_{j=1, j \neq i}^{m-n-1} P_j^{R_{ji}}, \quad (3.17)$$

also exists. The $m - n - 1$ dimensionless P-products can be formed from Q_1, Q_2, \dots, Q_m . R_{ij} are constant exponents and α is a dimensionless constant (Mendoza, 1994). To define α , the dimensionless quantity, the Q_1, Q_2, \dots, Q_m physical properties have to be identified.

For the puff parameters, the independent variables are the reference velocity of the approach flow (U_{ref} [m/s]), the characteristic (or reference) length scale of the ambient boundary layer (L_{ref} [m]), the amount of the released tracer (V [kg]) and the release duration (T_{rel} [s]). Although the release

duration was considered infinitesimal and it was kept constant throughout the measurements, its effect on the dependent variable is still worth to be investigated.

To determine the dimensionless dosage (dos^*), the following relation can be written:

$$dos = dos^* U_{ref}^a V^b L_{ref}^c T_{ref}^d. \quad (3.18)$$

The fundamental physical dimensions occurring in Eq. (3.18) are mass (M), length (L) and time (T). Substituting these dimensions of the scaling variables to Eq. (3.18) results in

$$M^1 T^1 L^{-3} = dos^* (L^1 T^{-1})^a M^b L^c T^d. \quad (3.19)$$

To find dos^* , a system of equations based on the exponents of the physical fundamental dimensions in Eq. (3.19) is solved:

$$\mathbf{1} = \mathbf{b} \quad (3.20)$$

for mass,

$$-3 = \mathbf{a} + \mathbf{c} \quad (3.21)$$

for length and

$$\mathbf{1} = -\mathbf{a} + \mathbf{d} \quad (3.22)$$

for time. From experimental analysis, $a=-1$ is found (Figure 3.4). Now the number of unknowns and equations are equal, therefore the other exponents can be determined: $b=1$, $c=-2$, $d=0$. The dimensionless dosage therefore has the form

$$dos^* = dos \frac{U_{ref} L_{ref}^2}{V}. \quad (3.23)$$

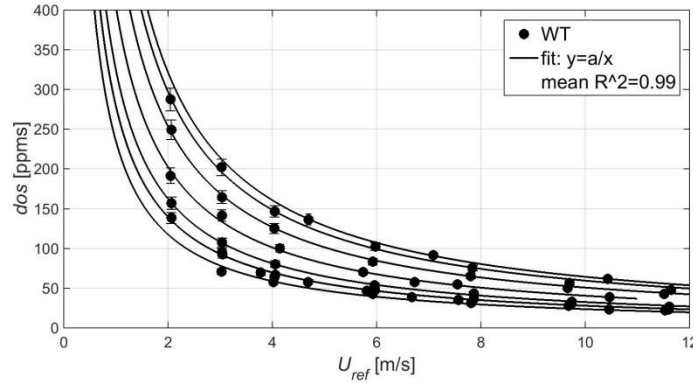


Figure 3.4 The relationship between the dosage and the reference wind speed in model scale for various measurement locations. The quality of the fit of $f(x)=a/x$ is characterized by the R^2 value. The data for this graph was taken from the measurements described in Harms et al. (2011) and Harms (2010).

In the same manner, the characteristic times (arrival time, peak time, leaving time, duration, ascent time and descent time) can be nondimensionalized (Berbekar et al., 2015a):

$$t^* = t \frac{U_{ref}}{L_{ref}}. \quad (3.24)$$

Eq. (3.24) also converts the time step of the measured concentration time series. Eq. (3.24) is the general formula to convert time scales in fluid mechanics, and by substituting the frequency ($f=1/t$), Eq. (3.24) turns into the reciprocal of the Strouhal number (Eq. 3.25).

$$Str == \frac{f L_{ref}}{U_{ref}}. \quad (3.25)$$

The dimensional analysis of the concentration statistics (such as the mean or peak concentration) results in an unbalanced set of equations.

$$pc = pc^* U_{ref}^a V^b L_{ref}^c T_{rel}^d. \quad (3.26)$$

$$M^1 L^{-3} = pc^* (L^1 T^{-1})^a M^b L^c T^d \quad (3.27)$$

From Eq. (3.27) we can see that $b = 1$, therefore the concentration and the released amount of tracer gas have a linear relationship. The remaining parameters can be defined by finding the relationship between the concentration and the reference wind speed (Figure 3.5). To eliminate the effect of the source term in Figure 3.5, the values are divided by the released amount. For the relationship between the concentration and the reference wind speed for puff releases (Figure 3.5.a) a linear fit gives a good correlation, however, the exponent a is small (-0.32). Therefore, it can be assumed that the peak concentration in case of instantaneous releases does not depend on the reference wind speed within the measurement range of a wind tunnel experiment. For continuous releases, the relationship between the concentration and the reference wind speed is rational (Figure 3.5.b). If $a = -1$ is substituted to Eq. (3.27), the resulting dimensionless formula will be the dimensionless concentration derived from the transport equation previously (Eq. 3.13).

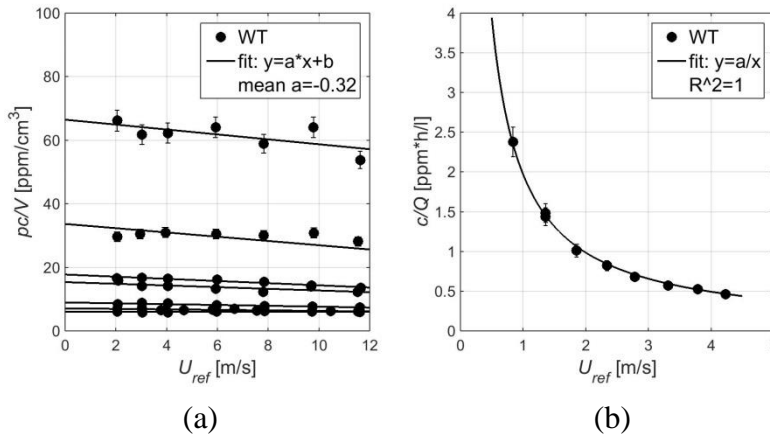


Figure 3.5 Exemplary results for the relationship between the concentration and the reference wind speed in model scale for puffs (a) and for continuous releases (b). The goodness of the fit for (b) is characterized by the R^2 value.

The puff results are from the measurements described in Harms et al. (2011) and Harms (2010). The continuous release case was measured within the Hamburg model.

Based on the dimensional analysis, the dimensionless peak concentration for puff releases has the form

$$pc^* = pc \frac{L_{ref}^3}{V}. \quad (3.28)$$

Eq. (3.28) also converts the concentration values of the measured time series.

Examples for an experimental verification of the derived dimensionless puff parameters are shown in Harms (2010) and Berbekar et al. (2015a).

Although it is a fair assumption that the peak concentration does not depend on the velocity, the release duration, similar to the time-dependent variables (Eq. 3.24), is scaled by the wind speed. Therefore, the mean approach flow velocity was constant during all puff measurements to ensure identical dimensionless release durations in case of a conversion to full scale.

Although the physical meaning of the ensemble average of the dimensionless puff time series is questionable, it characterizes well the average time dependence of the measured concentration. The concentration at the i 'th time step of the mean concentration time series of n independent puff concentration time series with the same quasi-stationary boundary conditions is

$$C^*(t_i^*) = \frac{\sum_{j=1}^n C_j^*(t_i^*)}{n}. \quad (3.29)$$

Short-term release measurements

Short-term releases are, in terms of release duration, in-between puffs and continuous releases and characterized by finite release duration. As the release duration is extended, the characteristics of continuous releases are more appropriate to evaluate short-term releases, than puff parameters. According to Robins et al. (2013), dispersion shows puff-like behavior (corresponding to instantaneous releases), if the arrival time (or travel time) is significantly longer than the release duration. If the release duration exceeds the arrival time, the dispersion has a plume-like behavior (corresponding to a continuous release).

Figure 3.6 shows the relationship between the peak concentration related to the flow rate (pc/Q) and the release duration (T_{rel}). For puffs, according to Eq. (3.28), the pc/Q value increases with increasing release duration. The longer the release, the more the relation deviates from a linear correlation. The reason behind this is that with increasing release duration with respect to the arrival time, the dispersion is changing its behavior from puff to plume. Consequently, as the release duration increases, its effect on the peak concentration decreases until the puff release is turning into a continuous release and the peak concentration becomes independent from the duration of the release (see Eq. 3.13).

Figure 3.6 shows similar behavior for various test cases. Figure 3.6.a shows the relationship for the measurements described in Harms (2010), focusing on puff releases with identical release flow rates. The results of Figure 3.6.b and c were measured within the various measurement campaigns of the Hamburg test case described in Chapter 3.2.5. Figure 3.6.b shows the results of puff releases with identical release flow rates containing long release durations (up to $T_{rel}=8.2at$) as well. Finally, during the measurements of Figure 3.6.c, the released amount of tracer gas was kept constant. All results show the behavior of the puff releases turning into plumes, while the linear relationship between pc/Q and T_{rel} disappears. The linear fits are estimated from the points where $at > 2T_{rel}$ is true, considering the criterion of Robins et al. (2013) for puff-like behaviour, namely that the arrival time is significantly longer than the release duration.

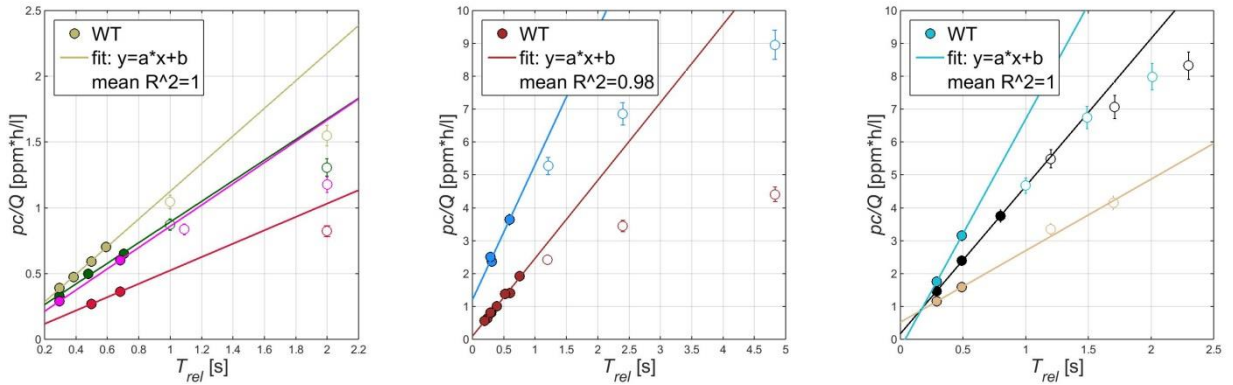


Figure 3.6 The relationship between the peak concentration related to the flow rate (pc/Q) and the release duration (T_{rel}) in model scale for short-term releases. The results are from the measurements described in (Frank Harms, 2010) (a) and the first (b) and the second (c) campaign of the Hamburg measurements (see Chapter 3.2.5). The points without marker face coloring were not considered for the linear fitting.

Based on the results, as long as a linear relationship exists between pc/Q and T_{rel} , the concentration values can be nondimensionalized by Eq. (3.28). For longer release durations (longer than about $at/2$), the concentration can be nondimensionalized, similar to continuous release measurements, according to Eq. (3.13).

Defining the time-dependent variables (such as duration, peak time or arrival time) is also not straightforward for short-term releases. In this thesis, the focus is on the part of the short-term release measurement time series, where the concentration decreases after a release. Therefore, only the definition of residence time (also called retention time) will be addressed (see Chapter 4.2.1). Further suggestions on the definition of time-dependent variables for short-term releases can be found in Berbekar et al. (2015b).

3.1.4 Relevant statistics

To describe the features of a data set quantitatively, descriptive statistics can be applied (Mann, 1992). The data analysis can be characterized based on the number of variables. The most

common measures of univariate analysis are the measures of central tendency (such as the mean or the median) and the measures of variability (such as the higher-order moments and the extremes). When a sample consists of more than one variable, the relationships between variables are characterized with measures such as covariance or correlation. In this thesis, the variables are considered separately, therefore univariate analysis was carried out.

Converting the results into dimensionless parameters makes them independent from the scale. However, to acquire generalizable data, the results should be statistically representative. In a steady-state inviscid laminar flow, one measurement data point would be enough to characterize the velocity or the concentration at a single point, if the measurement technique had no uncertainty. In a turbulent boundary layer the properties can be described with a distribution of the results, rather than a single value. To obtain statistically representative data, the distribution of measured values must be representative of the real distribution at the measurement location. This can be achieved by ensuring a sufficiently large sample size. On the other hand, when analyzing the data, the derived statistics have to be representative of the distribution. Therefore, the sample size must be large enough to be able to define the statistics that are representative of the whole distribution.

The mean of the distribution is a robust statistic, however in most atmospheric transport processes the variability is just as important to characterize. Although the extreme values can be crucial in some aspects (such as extreme concentrations in hazmat release situations), they are highly dependent on the temporal resolution of the detection device and the sample size. In some specific cases the extreme value of the distribution can be predicted (see Chapter 4.1.3), but it has a limited applicability to urban dispersion and a high uncertainty. Therefore, the scatter of the data will be characterized by the standard deviation and the high concentrations will be represented by higher percentiles, such as the 95th or the 99th percentile.

As an example, Figure 3.7 shows the concentration distribution of a continuous release measurement during the Michelstadt campaign. The mean, standard deviation, 95th percentile and the maximum of the distribution are also marked on the figure. As for all histograms in this thesis, the bin size was determined using the Freedman-Diaconis rule (Freedman and Diaconis, 1981).

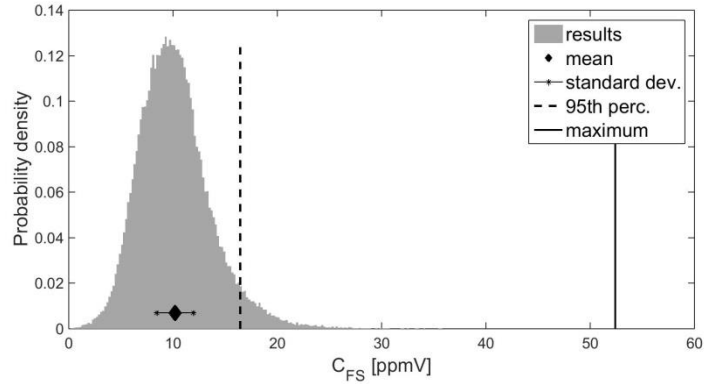


Figure 3.7 The mean, standard deviation, 95th percentile and the maximum of the concentration distribution resulting from a continuous release measurement during the Michelstadt campaign.

3.2 Test cases

3.2.1 Model geometries

The results of two wind tunnel test cases, Michelstadt (MS) and the inner city of Hamburg (HH), are analyzed in this thesis. Both test cases were measured in multiple campaigns with the aim of creating validation data sets for numerical models and gaining insight into transient dispersion phenomena in complex urban environments. The models were designed, produced and had been set up in the wind tunnel already prior to my PhD studies. Therefore, the extensive pretesting and corresponding measurements were focusing on the reproduction of the boundary conditions and results from the previous campaigns.

Michelstadt model

Michelstadt (Figure 3.8) is a 1:225 model of a semi-idealized Central European city designed by Bastigkeit (2011). The model contains 60 flat-roof buildings surrounding inner courtyards. The full-scale width of each building is 15 m, while the building height varies between 15 m, 18 m and 24 m (Bastigkeit, 2011). The streets are 18 m and 24 m wide, providing street-canyon ratios between 0.625 and 1.33 (Hertwig et al., 2012). According to Oke (1988), wake interference and skimming flow regimes are expected to dominate in such geometry, meaning that due to the building density, the flow above the geometry has limited access to the spaces between the buildings (Britter and Hanna, 2003).

The design of the model is based on the typical morphology of the residential areas in Central European cities (Di Sabatino et al., 2010), such as Hannover, Prague or Vienna. Although the model is a simplification of an urban geometry, it is sufficiently complex to represent the typical transient flow and transport phenomena in urban environments (see e.g. Hertwig et al.,

2012 and Efthimiou et al., 2015). More details on the geometry and on previous measurement campaigns can be found in the dissertation of Bastigkeit (2011).

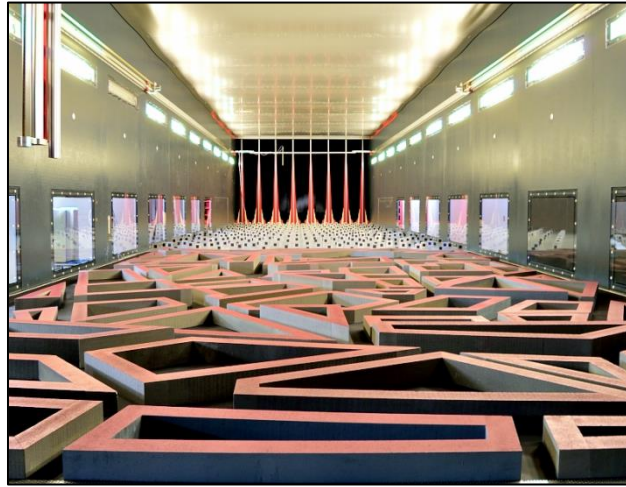
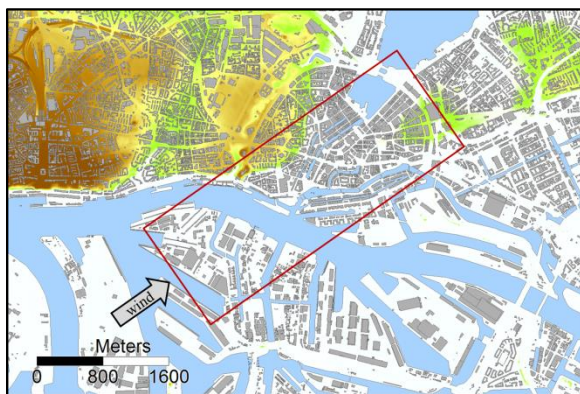


Figure 3.8 Michelstadt model in the wind tunnel

Hamburg (HH) model

The 1:350 model covers a 3675 m long and 1400 m wide area in full scale within the inner city of Hamburg (Figure 3.9.a). Figure 3.9.a was created using SAGA GIS (Conrad et al., 2015), as the other plots in this thesis illustrating the model geometries, unless stated otherwise. The wind tunnel model (Figure 3.9.b) was constructed based on the 3D data set of the buildings and topography provided by the *Landesbetrieb Geoinformation und Vermessung*. The precision of the building models is 0.5 m in full scale, and the horizontal resolution of the topography data is 5 m in full-scale dimensions. The direction of the mean approach flow is 235° . More details on the model, the boundary layer characteristics and the previous measurement campaigns can be found in Hertwig (2013).



(a)



(b)

Figure 3.9 Map of the area modeled in the wind tunnel (a). Hamburg model in the wind tunnel (b).

3.2.2 Wind tunnel facility

The test cases were measured in the “Wotan” boundary-layer wind tunnel of the Environmental Wind Tunnel Laboratory in Hamburg (Figure 3.1). The wind tunnel test section is 4 m wide and its approach flow and test sections together are 18 m long. The height of the test section can be adjusted between 2.75 m and 3.25 m. The axial fan at the end of the tunnel generates a flow with a maximum wind speed of 20 m/s (Harms, 2010).

The spires and roughness elements placed in the approach flow section of the wind tunnel ensure an inflow similar to the full-scale urban boundary layer assumed in Hamburg (Hertwig, 2013). The model geometry is made from dense extruded polystyrene foam. The surfaces of the buildings are aerodynamically rough to minimize the thickness of the viscous sub-layer (see Chapter 3.1.1).

A coordinate system for the test section of the wind tunnel was defined. The unit vector of the x axis is parallel to and pointing in the direction of the mean velocity vector of the approach flow. The y coordinate defines the distance in lateral direction from the centerline of the wind tunnel. The z coordinate is equal to the height above the wind tunnel floor.

3.2.3 Preliminary measurements

The aim of the pretests was to properly reproduce the boundary conditions and results from preceding test campaigns. To achieve this aim, not only the criteria of wind tunnel modeling introduced in Chapter 3.1.1 have to be fulfilled, but the characteristics of the flow and concentration field have to be the same as in the previous campaigns. The longitudinal pressure gradient as well as the lateral homogeneity and the Reynolds-number independence of the flow field are investigated first. In the second step, vertical velocity profiles at the same x and y coordinates are compared between the previous and the new campaigns. Finally, the results of continuous and puff release measurements are compared. For the first step, only the results of the Hamburg measurements are shown, but with similar results, the requirements were fulfilled for the Michelstadt test case as well.

Pressure gradient

The wind tunnel walls and the model geometry cause a blockage effect on the wind tunnel flow (VDI 3783/12, 2000). If the cross-sectional area of the wind tunnel is constant along the approach flow and test section, the static pressure will decrease in flow direction. Therefore, the height of the ceiling of the approach flow and test section in Wotan can be varied to minimize the *longitudinal pressure gradient*. According to VDI 3783/12 (2000), the longitudinal pressure gradient in the wind tunnel has to fulfill the following criteria:

$$p_{\delta}^* = \left| \frac{\frac{\partial p}{\partial x} \delta}{\frac{\rho}{2} U_{\delta}^2} \right| \leq 0.05, \quad (3.30)$$

where p_{δ}^* is the dimensionless longitudinal pressure, δ is the thickness of the modeled boundary layer and U_{δ} is the wind speed at δ height. The p_{δ}^* profile in the wind tunnel measured for the Hamburg test case is shown in Figure 3.10. The model geometry starts at $x_{FS} = 7.5$ m.

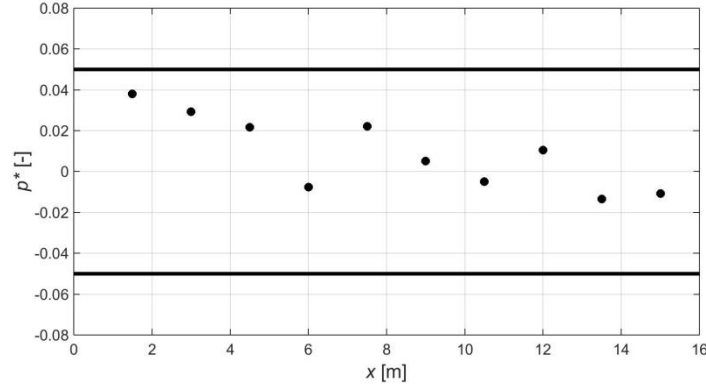


Figure 3.10 The dimensionless longitudinal pressure gradient of the wind tunnel during the measurements of the Hamburg test case. The thick solid lines represent the Eq. (3.30) criterion. The x axis represents the distance from the upwind side of the approach flow section of the wind tunnel.

Flow measurements

A 2D fiber-optic Laser Doppler Anemometer (LDA) was used to measure the components of the velocity vectors. First the u_x and u_y components and then the u_x and u_z components were measured simultaneously. A reference wind speed was measured at the entrance of the approach flow section using a Prandtl tube. The mean velocity measured with the Prandtl tube is scaled to a representative reference velocity (U_{ref}) upwind of the core model area within the modeled ABL flow.

The focus of the flow measurements was to optimize the arrangement of the spires and roughness elements in order to improve the characteristics of the approach flow, to verify the reproducibility of the results from previous campaigns and to document compliance with the criteria of lateral homogeneity and Reynolds-number independence of the flow.

The *lateral velocity profile* measured in the wind tunnel during the Hamburg test case is plotted in Figure 3.11.a. The scatter bars represent $\pm 2\%$ of the mean velocity. Except for the outer edges, the velocity deviation in lateral direction was found to be smaller than $\pm 2\%$.

To identify the velocity corresponding to Re_{crit} , where *Reynolds-number independence* of the flow is reached, the velocity was measured at various locations at a range of reference wind speeds. The dimensionless velocity at an exemplary measurement point is plotted against the

reference wind speed in Figure 3.11.b. At the given location, the flow is Reynolds-number independent for wind speeds above $U_{ref} = 1.9$ m/s.

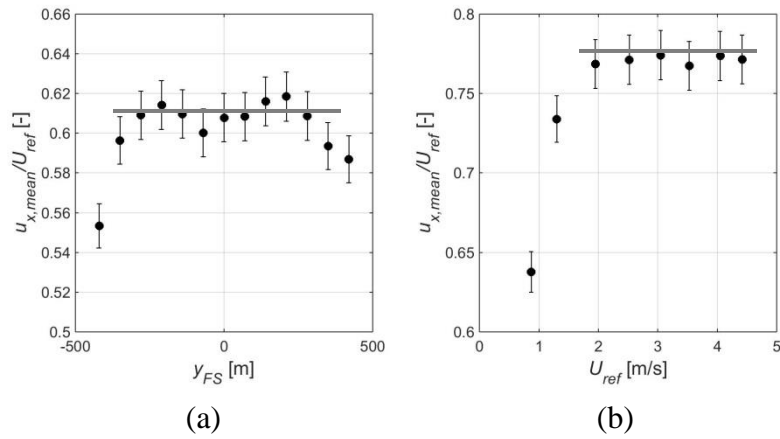


Figure 3.11 The lateral velocity profile in the wind tunnel (a) and the profile of a Reynolds-number independence test (b) during the wind tunnel measurements of the Hamburg test case. (The gray lines are only plotted as visual aids, and have no physical or mathematical meaning.)

The results show, that the longitudinal pressure gradient and the lateral inhomogeneity of the mean velocity are within the criteria of the current wind tunnel measurement standards, the flow is Reynolds-number independent, the setup of the roughness elements and the model geometry are identical (within an uncertainty of 2 mm). This suggests, that the velocity field of the previous campaign should be reproducible within the uncertainty of the measurements. Vertical velocity profiles were measured at multiple locations to compare the flow field of the previous and the new measurement campaigns. Statistical characteristics of the measured velocity component u_x are plotted for one exemplary profile measured in the Hamburg test case (Figure 3.12) and the Michelstadt test case (Figure 3.13). Similar comparisons were carried out for each measurement location and each velocity component.

For the Hamburg test case, instead of uncertainty bars, results of multiple measurements are plotted at the same locations. The scatter of these measurements is a representative measure of the reproducibility of the results at the given location. According to Figure 3.12, the difference between the results of the two campaigns is in the same order of magnitude as the scatter of the measurements within a single campaign.

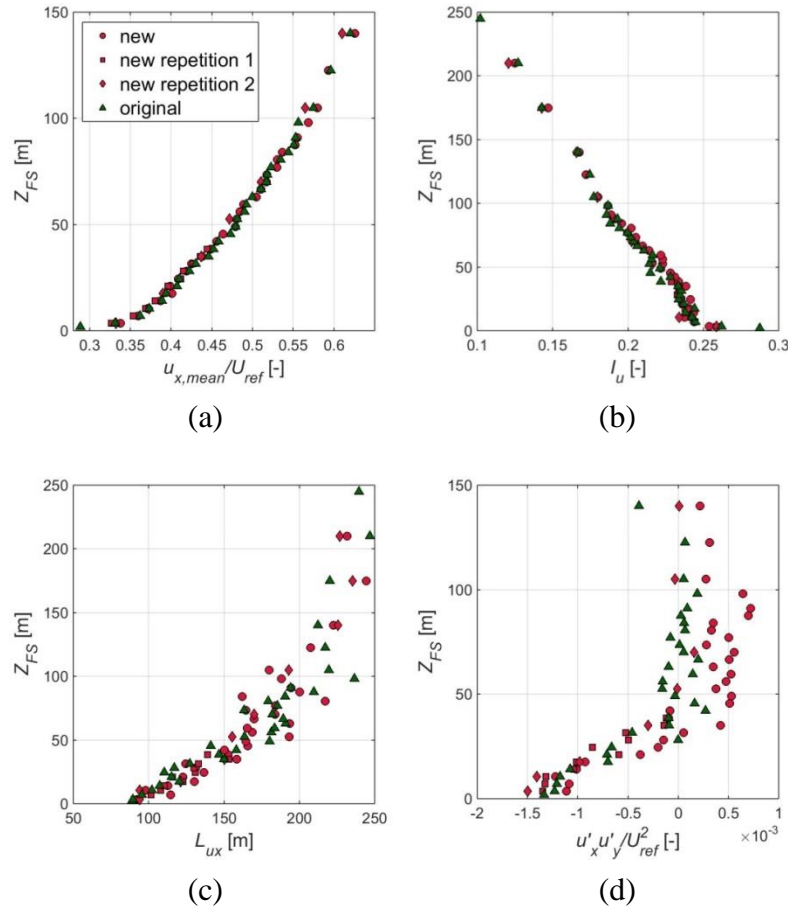


Figure 3.12: Comparison between the previous and new campaigns of vertical profiles of statistical measures of the velocity component u_x for the Hamburg model: mean velocity (a), turbulence intensity (b), integral length scale of turbulence (c) and flux (d).

For the Michelstadt test case, no repeated profiles are available. In Bastigkeit (2011) the uncertainty of the x component of the mean velocity is documented to be 2.45%. In Figure 3.13.a, this uncertainty is plotted as the error bars of the results, although due to the small values they are hardly visible.

Based on Figure 3.12, Figure 3.13 and the comparisons at other measurement locations and velocity components, the flow fields of the new measurement campaigns sufficiently reproduce the flow fields of the previous campaigns within the uncertainty of a single campaign. It is worth noting that the measurements were carried out within the model geometry, causing a deviation from typical approach flow boundary-layer characteristics, such as constant shear or the integral length scales corresponding to different roughness length (see Chapter 2.2.2).

Since the focus of this thesis is the investigation of transport phenomena by analyzing the concentration field, velocity measurements were only carried out to ensure the reproducibility of results of the previous campaigns. This enables results from different independent measurement campaigns to be combined to form a large set of experimental data. A detailed analysis of the

approach flow and the flow field within the models can be found in Bastigkeit (2011) for Michelstadt and in Hertwig (2013) for the Hamburg test case.

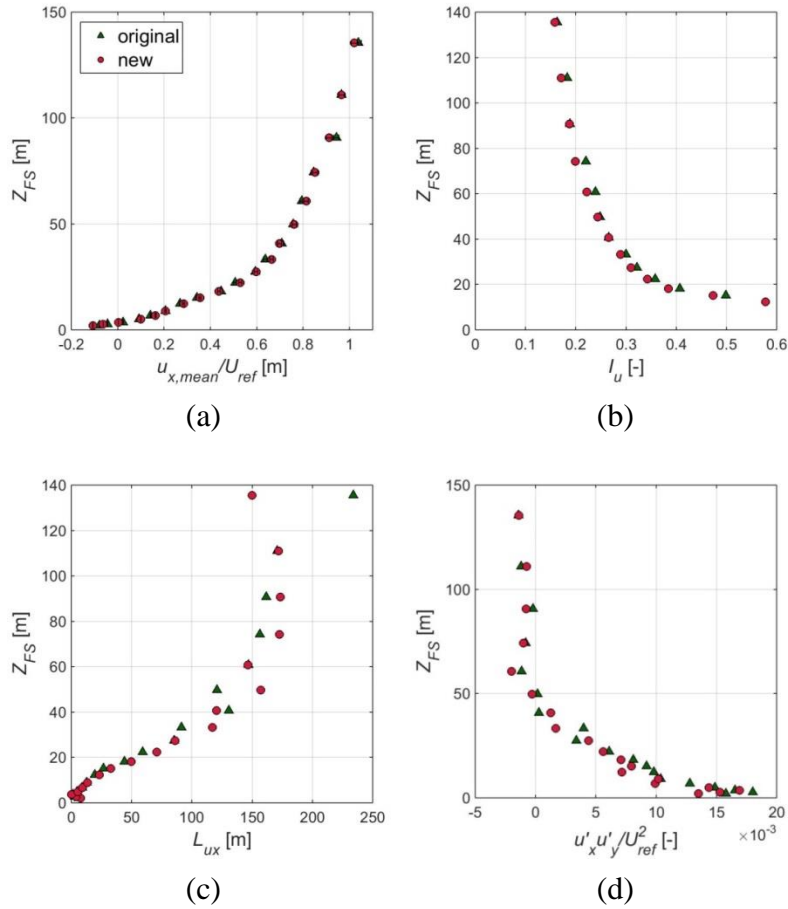


Figure 3.13 Comparison between the previous and new campaigns of vertical profiles of statistical measures of the velocity component u_x for the Michelstadt model: mean velocity (a), turbulence intensity (b), integral length scale of turbulence (c) and flux (d).

Concentration measurements

To simulate scalar transport, fast solenoid micro-valves were mounted in the model acting as ground-level point sources of ethane tracer gas (Berbekar et al., 2015a). Ethane is a non-reactive tracer with a density close to air, resulting in non-buoyant dispersion. A laboratory-grade electronic mass flow controller was used to adjust and monitor precisely the amount of the released tracer. A bypass release configuration ensured the stability and the repeatability of the puff release rates. The exhaust velocity and the corresponding momentum of the released material were significantly lower than the wind velocity around the source, modeling a passive emission. A fast FID with approximately 1 ppm detection sensitivity in model scale (considering the sensitivity, amplification and calibration) was used to measure the instantaneous concentration time series point by point within the model area. The background concentration

was permanently monitored with an additional FID in the approach flow section, and background concentration was subtracted from the measured values before further analysis.

Reynolds-number independency of concentration measurement results was tested in a similar manner as for the flow field. Due to the higher uncertainty of the concentration measurements, it is hard to define the value of Re_{crit} based on Figure 3.14. However, it is clear that above the Re_{crit} of the flow field (Figure 3.11.b) the mean concentration is also constant within the extent of the uncertainty.

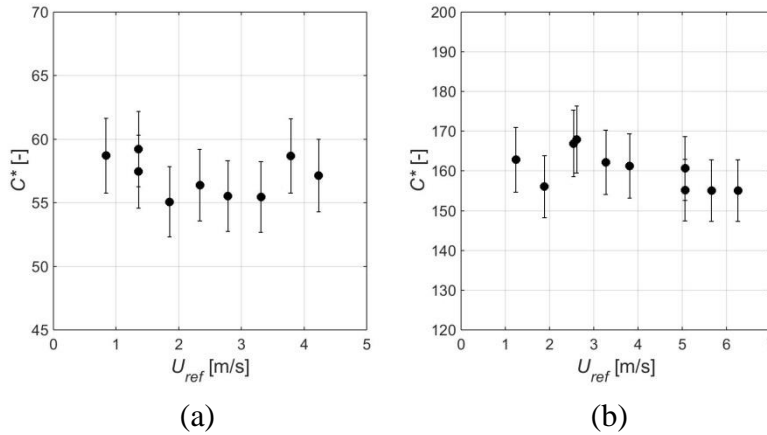


Figure 3.14 Exemplary concentration measurements of the Reynolds-number independence tests for the Michelstadt (a) and the Hamburg (b) test case.

3.2.4 Representativeness and reproducibility

The result of a measurement provides an estimate of the true value. Therefore, measurement results are only comprehensive if their uncertainty is defined (JCGM, 2008).

For both test cases, the uncertainty was estimated applying “within-laboratory reproducibility conditions” (Hasselbarth et al., 2006). The following conditions applied:

- same measurement procedure,
- same laboratory,
- partially different equipment,
- different operators,
- different environmental conditions,
- different calibration curves.

Significant efforts were made to minimize systematic uncertainties and to minimize and quantify random uncertainties. Precise positioning of the geometry and the probes, frequent calibration of the measurement equipment using independent standards, tracking the changes of the environmental conditions, reproducing the approach flow of the previous campaigns and

using high-precision measurement equipment are only a few examples for the experimental efforts spent to decrease the uncertainties of the concentration measurements.

The *random uncertainty* of the statistical characteristics is partially caused by the turbulent fluctuation of the flow field. This can be decreased with larger sample size if the mean boundary conditions are constant. For measurements with continuous release, longer measurement duration ensures lower variability of statistics (Figure 3.15.a). For puff measurements, the uncertainty caused by turbulence can be decreased by larger ensemble size of the releases (Figure 3.15.b).

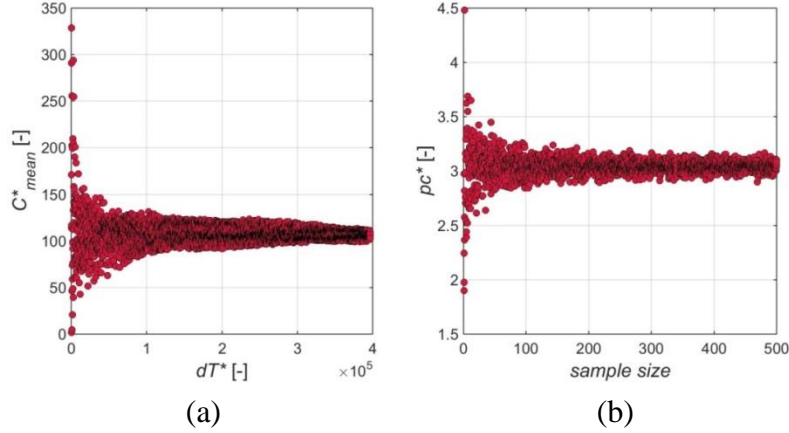


Figure 3.15 Exemplary convergence plots of the mean concentration for continuous releases (a) and peak concentration for puff releases (b).

The continuous release measurement evaluated for Figure 3.15.a was three times longer than the average length of all measurements. dT^* represents the nondimensional averaging times. For each dT^* value, four parts with dT^* duration are randomly selected from the whole concentration time series. Each partial time series is averaged over time and the results are plotted on Figure 3.15.a. As expected according to Harms et al. (2011), the variability of the mean values decreases proportionally to $1/\sqrt{dT^*}$ with increasing averaging times. For each dT^* the *coefficient of variation* (standard deviation relative to the mean) was calculated:

$$c_v = \frac{\sigma_{C^*}}{\mu_{C^*}}. \quad (3.31)$$

The average c_v for the typical measurement length range (dT^* is between $2 \cdot 10^5$ and $3 \cdot 10^5$) was found to be 5%.

The convergence test for the puff releases is demonstrated on the variability of the peak concentrations (pc^*) recorded at a location, where 2400 puffs were measured (Figure 3.15.b). For each sample size on the x axis, four samples containing randomly selected values are considered. On Figure 3.15.b the average value of each sample is plotted. The typical sample size of a measurement was between 200 and 300. The average coefficient of variation for this interval is 1.7 %.

Due to the random sample selection, Figure 3.15 and the c_v values change with each repetition of evaluation. However, at the typical measurement length of the continuous releases and ensemble size of the puff releases, the scatter of the c_v values is negligible. The difference between the maximum and the minimum c_v values of 20 repetitions was 0.55% for the mean concentration of continuous release measurements.

There are effects (e.g. the precision of placing the model buildings) whose influence on the measurement uncertainty is hard to quantify if only the theoretical uncertainty of the instruments is considered. Therefore, to quantify the overall uncertainty of the concentration measurements, *type A* evaluation method was applied according to Taylor and Kuyatt (1994). During a type A evaluation, the measurements are repeated at various locations multiple times. Repetition measurements were carried out with different calibration curves, different environmental conditions and even in different campaigns. For each location, the standard deviation of the distribution of the characteristic statistical parameters (such as mean or maximum concentration) was determined. The standard deviations of all measurement locations for each statistical parameter form folded-normal distributions (Figure 3.16).

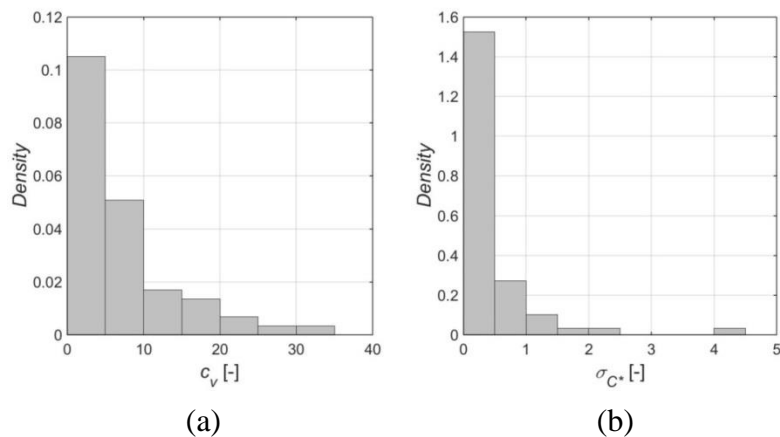


Figure 3.16 Exemplary distributions of standard deviations of the mean concentration (a) and coefficients of variation (b) for the continuous release repetition measurements of the Hamburg test case.

Defining the uncertainty of the dimensionless concentration is not straightforward. The measurement equipment has an absolute uncertainty, which would suggest defining the uncertainty of the results as an absolute value as well. However, during the wind tunnel measurements, the flow rate of the gas and the velocity of the approach flow were varied to keep the measured concentration in the optimal measurement range of the equipment. While nondimensionalizing the concentration with the flow rate and the velocity, the uncertainty of the FID must also be nondimensionalized, resulting in a mixture of absolute and relative uncertainty.

Table 3.1 Uncertainty values of selected statistical parameters characterizing continuous release measurements within the different campaigns.

campaign	C* mean relative [%]	C* mean absolute [-]	pc* [%]	C* 95 [%]
MS	10.8	16.2	35.2	7.8
HH previous	15.5	3.0	39.1	18.9
HH new	7.6	5.9	31.0	8.2
HH all	15.7	5.4	27.1	18.5

Generally, the relative uncertainty values are considered while presenting the results. However, if the statistics characterizing continuous release measurements are below the absolute uncertainty of the mean concentration, then this uncertainty is applied to make sure that the absolute uncertainty of the measurement device is not neglected.

The relative uncertainty of each statistical characteristic is defined as the 90th percentile of the distribution of the coefficients of variation (c_v). The absolute uncertainties of the statistics are defined as the mean of the distribution of the coefficients of variation. The relative and absolute uncertainties for some of the statistical characteristics of continuous release measurements are listed in Table 3.1.

According to Table 3.1, the relative uncertainty of the previous measurements in the Hamburg model is twice as high as the uncertainty of the new campaign. In the preceding measurements substantial effort was dedicated to identify areas possibly affected by a ground level release by tracking the edges of dispersion plumes. Therefore, numerous measurements were carried out at locations with extremely low concentration values, resulting in high relative uncertainties compared to the results of the new campaign, where most measurements were carried out well within the area exposed by the release.

Since the characteristics of puff measurements depend on both concentration and time, relative uncertainties were considered for these parameters (Table 3.2).

Table 3.2 Uncertainty values of some statistical parameters characterizing puff release measurements within the different campaigns.

campaign	pc* [%]	dos* [%]	at* [%]	pt* [%]
MS	10.9	8.9	3.1	3.4
HH previous	7.4	8.6	2.1	2.3
HH new	8.4	7.9	2.4	3.1
HH all	9.1	14.6	3.1	3.3

According to Table 3.1 and Table 3.2 the overall uncertainty is indeed higher than the random variability caused by the fluctuation of the flow field.

The uncertainty of quantities defined as the function of independent measured variables is calculated based on the error propagation formula (Taylor, 1983). The absolute error of an R_Q quantity defined as a function of n number of x_i variables is

$$\delta R_Q = \sqrt{\sum_{i=1}^n \left(\delta x_i \frac{\partial R_Q}{\partial x_i} \right)^2}. \quad (3.32)$$

The reproducibility of the two campaigns of the Hamburg test case does not differ significantly from the reproducibility of the whole data set. This implies that the concentration field from the previous measurements was successfully reproduced. In Figure 3.17 the 95th percentiles of the concentration distributions at various measurement locations are compared for the two campaigns of the Hamburg test case. Although most results fall within the uncertainty, in case of S9, a source located at the junction of two streets, the reproducibility is worse at some measurement locations. The reason of this discrepancy was not investigated further, due to the limited amount of available data.

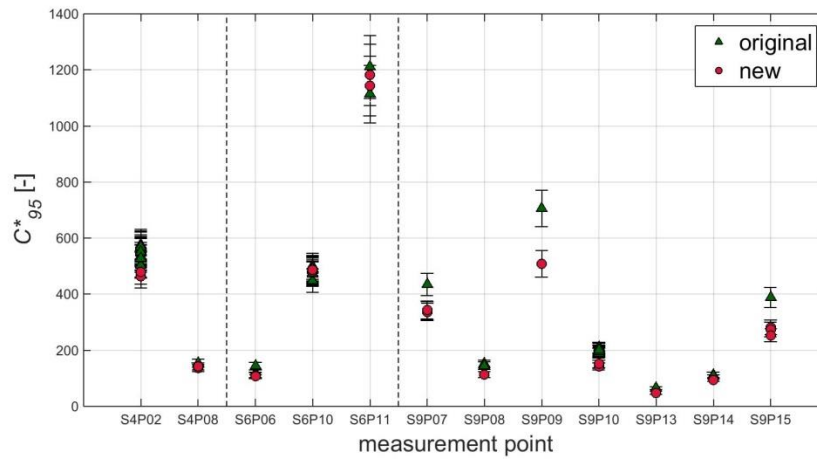


Figure 3.17 95th percentiles of the concentration distributions, taken from the two measurement campaigns of the Hamburg test case.

3.2.5 Data sets

This section only focuses on the data set that was considered for this thesis and does not give a full overview of all the wind tunnel experiments carried out in the two wind tunnel model geometries. An overview of the selected measurements is listed in Table 3.3.

Table 3.3 Statistics of the measurements carried out on the two model geometries

campaign	wind directions	sources	geometry types	continuous releases	puff releases	decay tests	measurement planes	vertical profiles
HH all	1	6	5	666	189	41	3	13
Michelstadt	2	6	1	431	72	0	2	7

Michelstadt

The Michelstadt data set consists of two wind directions with 180° difference (Figure 3.18). Six source locations were in use in continuous and puff release modes. Most measurements were carried out at half-building height (7.5 m in full scale). An additional plane was measured for one source location inside a courtyard at 52.4 m height. 7 vertical profiles are also part of the measurements.

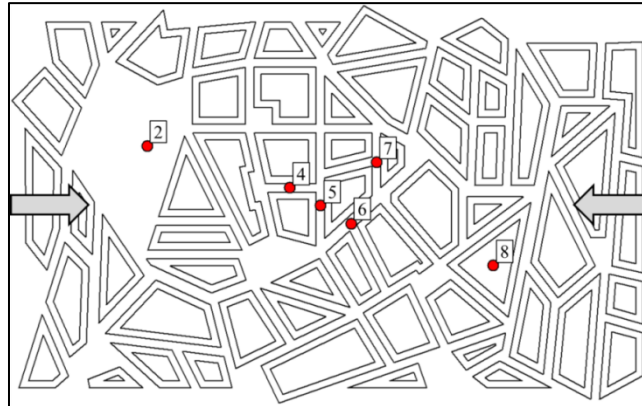


Figure 3.18 The geometry of Michelstadt. The arrows indicate the two measured wind directions and the sources are marked with dots. The labels are the names of the source locations.

Hamburg

Only the most typical wind direction of Hamburg, 235° (Figure 3.9) was chosen for the measurements (Hertwig, 2013). The results of six sources were included in the data set (Figure 3.19). Continuous, puff and finite-duration releases were measured. The main horizontal measurement plane is at pedestrian level (2.1 m in full scale). Two additional horizontal planes and numerous vertical profiles were also measured.

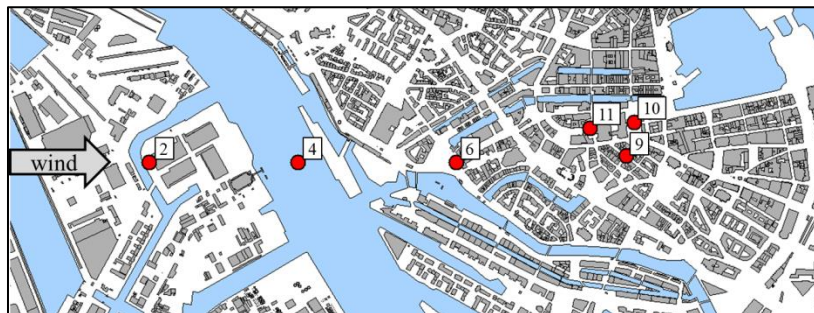


Figure 3.19 The area of the Hamburg model. The red dots represent the release locations. The labels are the names of the source locations.

Measurements were carried out on five geometrical configurations (Figure 3.20 to Figure 3.24). The high-resolution buildings were gradually substituted by Level of Detail 1 (LoD1) geometry. The LoD1 data set consists of buildings with flat roofs, and the outline is defined based on digital field map measured by airborne laser scanning. The buildings replaced by LoD1

models are highlighted in Figure 3.21 to Figure 3.23. With each phase, the number of simplified buildings increases in the model. The purpose of this study was to identify the effects of geometry changes and simplifications on dispersion and trace gas transport. Numerical modeling is widely used to predict transport and dispersion in urban areas (Lateb et al., 2015). However, the city geometries considered by the models are simplifications of the full-scale building structure. This simplification is due to the limited resolution of the input data and the discretization of the modeled fluid volume. By changing the geometry step-by-step, the tendency of the effects can be studied as well.



Figure 3.20 Original, high resolution geometry.



Figure 3.21 Phase 1 geometry.



Figure 3.22 Phase 2 geometry.

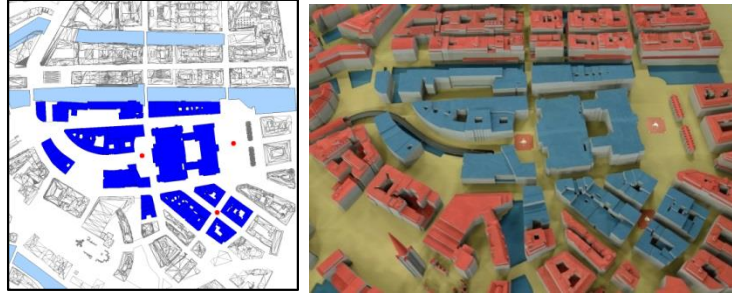


Figure 3.23 Phase 3 geometry.

A further test case (Phase 0, Figure 3.24) was also measured. In this case one building (the city hall of Hamburg) was entirely removed from the high-resolution geometry. The purpose of the measurements was to identify the effects of fundamental changes in the city geometry on the dispersion characteristics.



Figure 3.24 Phase 0 geometry, where the city hall is missing.

The difference between the high resolution and the LoD1 geometries is illustrated by the two models of the city hall of Hamburg. The real structure of the city hall is quite complex (Figure 3.25.a). Figure 3.25.b and c shows the high-resolution and LoD1 wind tunnel model of the city hall respectively. The tower of the building is completely missing from the LoD1 geometry.

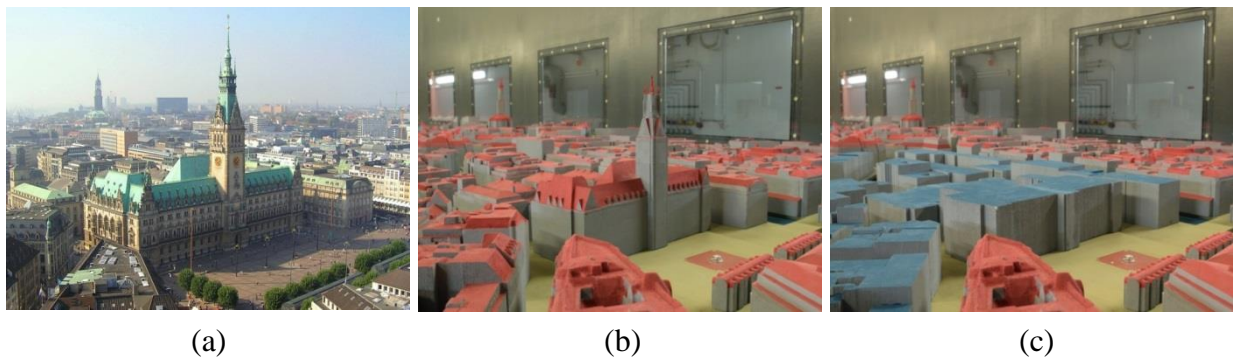


Figure 3.25 The city hall of Hamburg (a, source: Wikipedia, 2016a). The model of the city hall in the high-resolved (b) and LoD1 (c) geometries.

3.2.6 Model validation based on the data sets

Numerical models are often used to predict the dispersion of airborne materials within urban environments. As described previously in Chapter 3.2.5, the mathematical models developed for atmospheric processes are based on assumptions, which have to be case-specifically validated using qualified reference data. Commonly accepted guidelines for the validation of generic flow and dispersion models exist. Hasselman et al. (2002) describe a hierarchical approach for model validations in general, whereas Oberkampf and Trucano (2002) give an overview of the verification and validation of CFD models. General guidelines focusing on urban flow and dispersion modeling also exist and are applied by modelers (e.g. Schatzmann and Britter, 2011; Schatzmann and Olesen, 2010; Britter and Schatzmann, 2007; Schlünzen et al., 2004; Schatzmann and Leitl, 2002). The guidelines give general information on how to proceed in order to validate a model properly.

Even though one of the common criteria of the guidelines of model validation is to compare the results of the model to validation data of sufficient quality, the definition of proper validation data is in most cases not described in detail. The existing standards of physical modeling do not necessarily cover all criteria required to produce validation data sets qualified for state-of-the-art models (Leitl, 2009). Schatzmann and Leitl (2011) give a general description of a proper wind tunnel validation data set for numerical models. However, some aspects specifically important for modeling local-scale accidental releases, such as dispersion from an instantaneous source, are not discussed.

The COST Action ES1006 was an international cooperation focusing on the evaluation, improvement and guidance for the use of local-scale emergency prediction and response tools for airborne hazards in built environments. This goal can only be accomplished if the models are evaluated with application-specific high-quality validation data. A specific set of reference data requirements were introduced within the COST Action ES1006, which focuses on the validation of numerical models with various complexity applied for local-scale hazmat dispersion (COST ES1006, 2015c).

Although many full-scale and wind tunnel measurement results are used as reference data sets for model validation, many do not satisfy the requirements of a reference data set and are usually insufficient to validate local-scale emergency response tools (COST ES1006, 2015c). As discussed previously in the introduction of Chapter 3, field measurement data, even from large campaigns, such as the BUBBLE experiment (Rotach et al., 2004), the Joint Urban 2003 (Allwine et al., 2004) and the Thorney Island (McQuaid, 1985 and Puttock, 1985) case studies, do not have the necessary statistical representativeness (Schatzmann et al., 2000) for proper model validation.

The entire Michelstadt and Hamburg data sets (the results presented in this thesis together with previous measurement campaigns: Hertwig, 2013, Hertwig et al., 2012 and Bastigkeit, 2011) satisfy the criteria of a qualified validation data set according to the above-mentioned references.

The measurements are specified to evaluate emergency response tools used in case of an airborne release in urban environments.

Michelstadt data set

One of the purposes of the concentration measurements within the Michelstadt model was to provide a high-quality data set to be used by the COST Action ES1006 for model validation (Berbekar et al., 2013). The results of the first measurement campaign with 0° wind direction was provided as so-called "non-blind test data" to the modelers. This part of the data set can be used for an adaptive model validation or calibration, because the models can be adjusted to match the wind tunnel results. The results of the second test series (180° wind direction) were used as blind test. Only a minimum set of boundary conditions and wind velocity measurements at three measurement locations were available to the modelers to resemble a real emergency, when only limited data are available. Particularly the results of the blind validation exercise supported a realistic assessment of the uncertainties related to local-scale hazmat dispersion modeling in complex urban structures. Furthermore, the systematic test database enabled the identification of the sources of modeling uncertainty. As a part of the Action's work, a dedicated model evaluation protocol for a quantitative assessment of modeling performance was also developed (COST ES1006, 2015c).

One of the purposes of the COST Action ES1006 is to provide information for the end users about the applicability of the different modeling methods used for predicting the transport of airborne hazards in an urban area. The compared models are based on significantly different mathematical and numerical methods and concepts. The conceptual differences cause further variations as far as the type and extent of boundary conditions, preparation time before running the models, the CPU time and the expertise required to run the models are concerned. Likewise, the information quantity and quality provided as a result and the expected accuracy and reliability of the results might be substantially different. Since the purpose of the measurements was to create data to be used within the scope of the COST Action ES1006, the data set had to be qualified to serve the validation and the comparison of all different models. Furthermore, the comparison had to be evaluated in a way, which is clear for anybody, even outside the modeling community.

The validation data set for the COST Action ES1006 included time series, mean values, frequency distributions of measured and derived quantities, and statistical characteristics of the measurement results. The detailed description of the validation data set and the results of the evaluation exercise can be found in (COST ES1006, 2015b). Further examples of model validations based on the Michelstadt data set is shown by Efthimiou et al. (2015) and Rakai (2014).

Hamburg data set

The Hamburg data set was designed to validate CT-Analyst, an emergency response tool and the underlying LES code FAST3D-CT. CT-Analyst provides instantaneous predictions of chemical, biological, and radiological agent transport in urban settings (source: website of the NRL). CT-Analyst and FAST3D-CT have been extensively validated (see for example Harms et al., 2011; Leitl et al., 2012; Hertwig, 2013 and Leitl et al. 2016). Harms et al. (2011) evaluated the performance of CT-Analyst within Oklahoma City based on the wind tunnel measurements replicating the Joint Urban 2003 field test (Allwine et al., 2004). The aim of the previous campaign of the Hamburg measurements was to validate the FAST3D-CT LES code within a European urban environment (Hertwig, 2013). Hertwig (2013) also describes the requirements of a validation data set for LES models. CT-Analyst is capable of producing maps of the affected area among others. Within the previous campaign of the Hamburg measurements the prediction of the affected area was also validated (Leitl et al., 2012).

CT-Analyst can predict the time-resolved concentration field. Some time-dependent characteristics of the predictions, such as the puff parameters, were already compared with wind tunnel measurements. Details about previous comparisons can be found in Harms et al. (2011) and Leitl et al. (2012). However, the concentration decrease after a release has stopped is an important aspect for the end users of CT-Analyst that has not been thoroughly investigated before.

One of the purposes of the new campaign of the Hamburg measurements was therefore to test this ability. The short-term releases described in Chapter 4.2 were the basis of the evaluation. The details of the comparisons and validation can be found in Leitl et al., 2016. The results of the comparisons show that CT-Analyst can reliably predict the start of the concentration decay after the end of the release. The model provides a conservative estimate of the concentration time series after the decay starts.

4 Results and discussion

In this chapter the results of the previously presented Michelstadt and Hamburg measurements are evaluated to investigate hazmat transport in urban environments. Statistical analysis of spatial and frequency distribution of the measured concentration are discussed and modeled by various probability density functions. An evaluation method for the decay of the concentration time series is presented and applied on the measurements. The effects of geometrical simplifications and modifications on the transient dispersion field during various release scenarios are also investigated to derive general conclusions.

4.1 Statistical analysis of continuous release measurements

In a broad sense, every evaluation of the results presented in this thesis is a statistical analysis, since some statistical characteristic is derived to describe the measured distributions. The focus of this chapter is on the investigation of the measured concentration distributions and to study the predictability and the relationships between various statistical characteristics.

4.1.1 Spatial distribution of concentration

The vertical and crosswind concentration profiles resulting from a continuous point source release above a flat-open terrain or homogeneous roughness can be described by the Gaussian distribution (Eq. 2.30) derived from the averaged transport equation in Chapter 2.2.2.

According to Hanna et al. (1982), the Gaussian model originates from Gifford (1961), Pasquill (1961 and 1974) and Sutton (1932). The generalized Gaussian dispersion equation for a continuous point-source plume (considering the reflection of the ground, but not considering vertical dispersion reflection due to inversion) has the form

$$C(x, y, z) = \frac{Q}{U_{ref}} \frac{1}{2\pi\sigma_y\sigma_z} \exp\left(\frac{-y^2}{2\sigma_y^2}\right) \left[\exp\left(\frac{-(z-H_s)^2}{2\sigma_z^2}\right) + \exp\left(\frac{-(z+H_s)^2}{2\sigma_z^2}\right) \right], \quad (4.1)$$

where C is the concentration, x is the coordinate parallel to the direction of the approach flow, y is the horizontal coordinate perpendicular to the direction of the approach flow and z is the vertical coordinate corresponding to the height above ground (see Figure 4.1). The coordinates of the source are $(0, 0, H_s)$. Q stands for the release flow rate, U_{ref} is the mean wind velocity

component parallel to the main wind direction of the approach flow at H_S height, σ_y is the horizontal dispersion coefficient and σ_z is the vertical dispersion coefficient. In case of ground-level point sources ($H = 0$), Eq. (4.1) can be simplified to

$$C(x, y, z) = \frac{Q}{U_{ref}} \frac{1}{\pi\sigma_y\sigma_z} \exp\left(\frac{-y^2}{2\sigma_y^2}\right) \exp\left(\frac{-z^2}{2\sigma_z^2}\right). \quad (4.2)$$

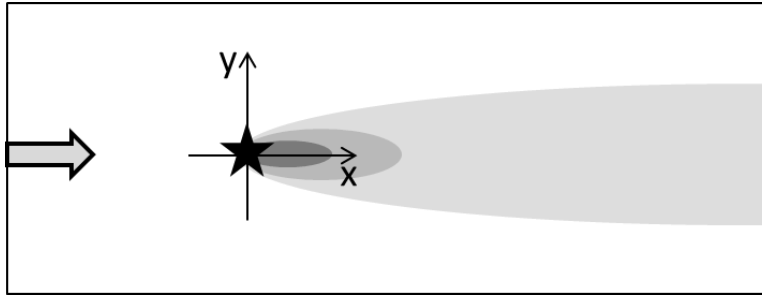


Figure 4.1 Definition of coordinate system for a point source release on a flat-open terrain. The source is marked with a black star and the wind direction is pointing from left to right. The arrow shows the wind direction of the approach flow and the shades of grey correspond to the expected concentration levels.

Applicability of the Gaussian distribution in urban environments

The Gaussian plume model (Eq. 4.2) only applies if the following constraints are met (Beychok, 1944):

- a. The vertical and crosswind diffusions follow Gaussian distributions.
- b. Downwind diffusion is negligible.
- c. The source term is continuous and constant.
- d. Mean horizontal velocity and mean wind direction are constant.
- e. No deposition, washout, chemical conversion or absorption of emissions occur and the ground is reflective (i.e. all emissions are conserved within the plume).
- f. No upper barrier to vertical diffusion and no crosswind diffusion barrier.
- g. Homogeneous turbulence through all three dimensions.

These constraints originate from the assumptions that were introduced in Chapter 2.2.2, while deriving and solving the averaged and simplified transport equation for continuous releases.

Let's see how these constraints apply in an urban boundary layer, modeled in a wind tunnel!

Criterion 1: Whether Gaussian distribution describes the vertical and crosswind diffusions properly is an ongoing debate. Many studies show that the concentration profiles in an urban environment, especially near the source location are strongly non-Gaussian (e.g. Balczó and Lajos, 2015; Coceal et al., 2014; Branford et al., 2011; Chavez et al., 2011 and Tseng et al., 2006). On the other hand, far from the source the Gaussian plume model gives a good estimation of the mean concentration profiles (e.g. Britter and Hanna, 2003; Davidson et al., 1995; Davidson et al., 1996; MacDonald et al., 1997 and Macdonald et al., 1998).

Criterion 2: Neglecting the downwind diffusion suggests that advection is the predominant mechanism for downwind transport. This is a fair assumption for flat-open terrains with high wind speeds, however, at low-wind spots (e.g. behind buildings) in a city, the downwind dispersion might have a significant influence on contaminant transport, therefore the criterion is not justifiable.

Criteria 3-5: Although these criteria are not fulfilled during a real accident, in a wind tunnel experiment they are possible to ensure. In case of the continuous release measurements of the Hamburg and Michelstadt test cases, the source release was continuous and constant and the mean flow field and wind direction were also constant. No additional sources or sinks were present and the ground was fully reflective.

Criteria 6-7: The last two criteria cannot be fulfilled in urban settings. When introducing an obstacle in a turbulent flow field, it will act as a diffusion barrier and will cause inhomogeneity in the turbulence.

Due to the limited applicability of the above listed criteria, the Gaussian plume model does not seem suitable for predicting scalar dispersion in an urban environment. However, due to its simplicity and its ability to produce instantaneous results, the Gaussian plume model is often used in practice especially in the context of emergency response to accidental releases. Although it is a general preconception that Gaussian models provide conservative predictions (COST ES1006, 2015a), in the COST Action ES1006 multiple Gaussian plume models were evaluated and the results show that the predictions are not necessarily conservative (COST ES1006, 2015b). It was also found that the Gaussian plume models give significantly worse predictions of the mean concentration patterns in urban environments than other types of models. (The value for fractions within a factor of two of the reference values was as low as 0.09 for the Michelstadt test case according to Trini Castelli et al., 2016, while the acceptance criteria in the document of COST ES1006, 2015b, is above 0.3.) It is unclear, whether the poor predictions were caused by wrong parameter choices or the deviation of the mean concentration profiles from the Gaussian distribution. This question will be analyzed in this thesis.

With additional assumptions, Eq. (4.2) can be further simplified for the x , y and z directions. Equations (4.3 to 4.5) show the parameterized forms of the simplified equations for all directions. The parameters can be defined based on the best fit of the equations on the measured values.

For a simplified equation in x direction (Eq. 4.3) the shape of mean dimensionless concentration profile is assumed to be similar throughout the y axis and the height of the measurement points is neglected. The horizontal and vertical dispersion coefficients (σ_y and σ_z) are modeled as power functions of the distance from the source as suggested originally by Smith (1968). The resulting parameterized equation is a power function.

$$C^*(x) = \frac{a}{bx^b}. \quad (4.3)$$

For the simplified Gaussian plume equation in y direction an extra degree of freedom is introduced with the d parameter, allowing the profile to take its maximum independently from the source location, whereas the Gaussian dispersion equation assumes that the plume centerline is aligned with the source parallel to the main wind direction.

$$C^*(y) = \frac{a}{bc} \exp\left(\frac{-(y-d)^2}{2b^2}\right) \exp\left(\frac{-z^2}{2c^2}\right). \quad (4.4)$$

The parameterized Gaussian distribution profile for the dimensionless concentration in vertical direction has the form

$$C^*(z) = \frac{a}{bc} \exp\left(\frac{-y^2}{2b^2}\right) \exp\left(\frac{-z^2}{2c^2}\right). \quad (4.5)$$

The parameterized equations were fitted on the measurement results. The parameters were determined by nonlinear least squares analysis. Exemplary results are shown in Figure 4.2 to Figure 4.12. Further results can be found in Appendix A. The black dots in the figures indicate the source positions and the squares represent the measurement locations. The mean approach flow direction is pointing from left to right on each map. Where repetition measurements were available, several results are plotted for one measurement location to give a sense of the variability.

Eq. (4.3) gives a reasonable fit for the longitudinal mean concentration profiles within and above the Michelstadt and Hamburg model. The power function does not only describe the concentration distribution within a street canyon parallel to the mean direction of the approach flow (Figure 4.2 and Figure 4.5), it also fits well for points located in different street canyons, separated by buildings (Figure 4.3).

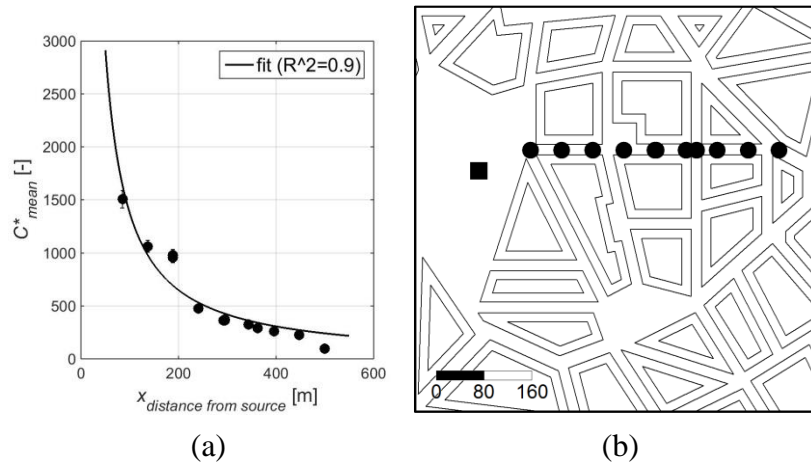


Figure 4.2 Exemplary longitudinal mean concentration profile measured at half-building height in a street canyon of the Michelstadt model (a). The fit of the simplified Gaussian distribution in x direction is indicated with a black line. The locations of the source (square) and measurements (circles) within the model (b). The mean wind direction of the approach flow is from left to right, as for all figures without the indication of the wind direction.

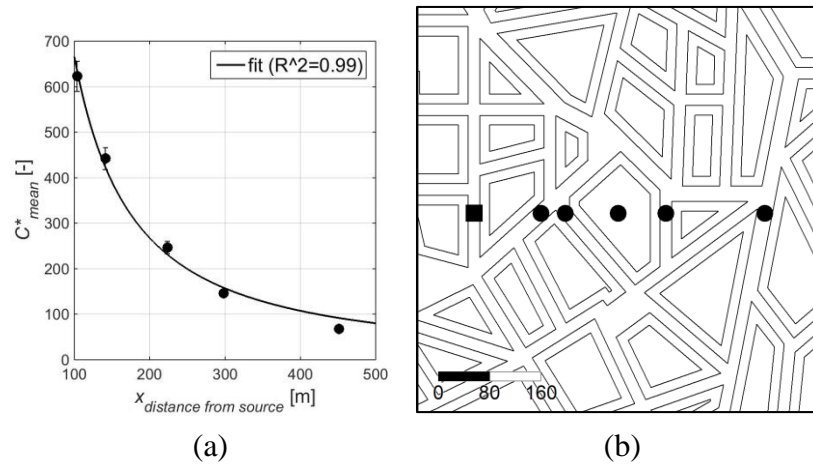


Figure 4.3 Exemplary longitudinal mean concentration profile measured at half-building height within separate street canyons in the Michelstadt model (a). The fit of the simplified Gaussian distribution in x direction is indicated with a black line. The locations of the source (square) and measurements (circles) within the model (b).

There is a deviation from the power law for measurements above building height close to the source location. As Figure 4.4 and Figure 4.6 show, the concentration first increases downwind from the source before it starts decreasing again. In these cases, close to the source the height difference between the measurement point and the source cannot be ignored, suggesting that this assumption of Eq. (4.3) is not applicable. However, once the concentration starts to decrease in downwind direction, the power law gives a good fit on the measurements.

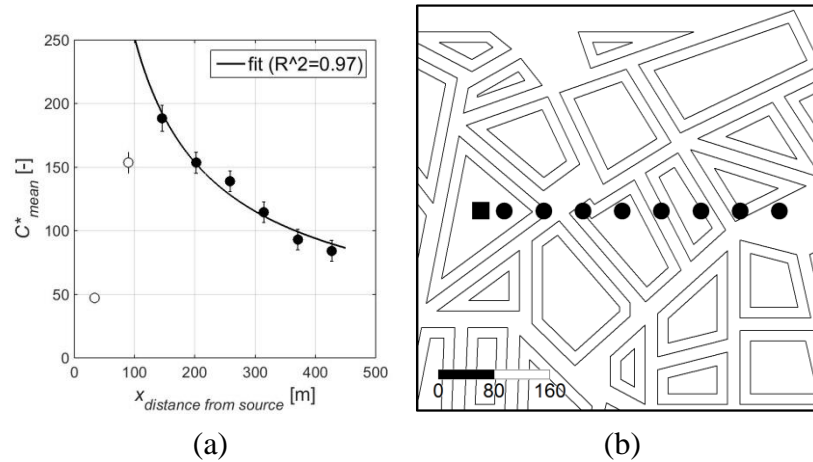


Figure 4.4 Exemplary longitudinal mean concentration profile measured above the buildings of the Michelstadt model at 52.4 m height in full scale (a). The fit of the simplified Gaussian distribution in x direction is indicated with a black line. The locations of the source (square) and measurements (circles) within the model (b).

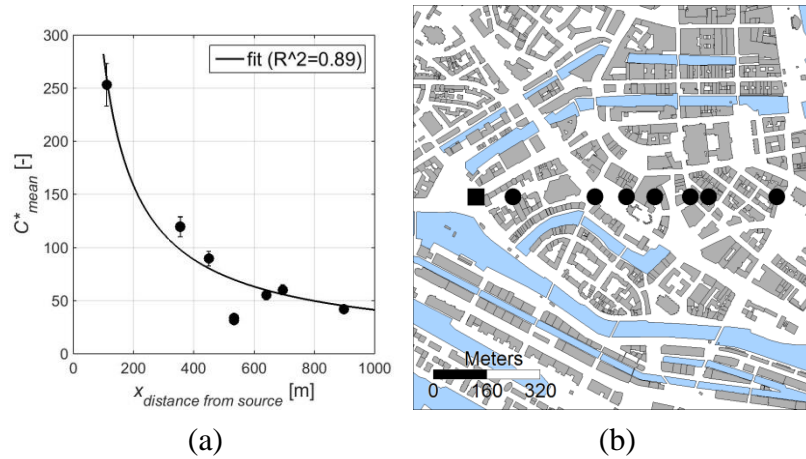


Figure 4.5 Exemplary longitudinal mean concentration profile measured at pedestrian level in the Hamburg model (a). The fit of the simplified Gaussian distribution in x direction is indicated with a black line. The locations of the source (square) and measurements (circles) within the model (b).

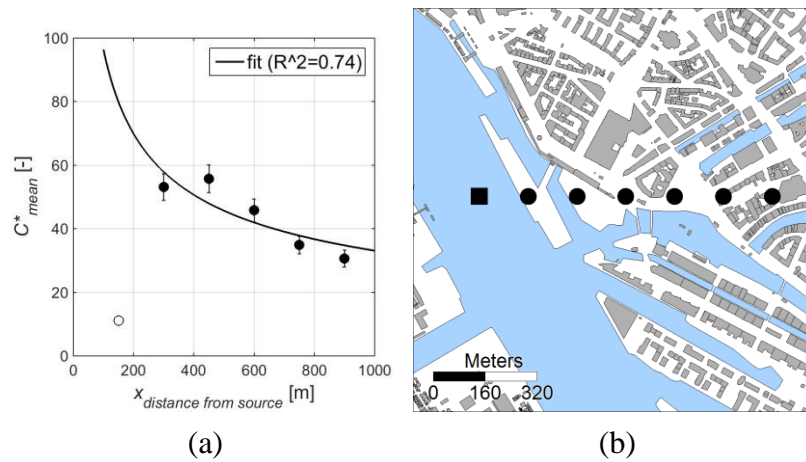


Figure 4.6 Exemplary longitudinal mean concentration profile measured above roof level of the Hamburg model at $z=52.5$ m height in full scale (a). The fit of the simplified Gaussian distribution in x direction is indicated with a black line. The locations of the source (square) and measurements (circles) within the model (b).

On the mean concentration profiles perpendicular to the mean direction of the approach flow, Eq. 4.4 was fitted. The Gaussian distribution fits well on most of the lateral concentration profiles. The Gaussian plume model anticipates the symmetry axis of the mean concentration profile to be aligned with the source location. By introducing an extra degree of freedom to the Gaussian plume model in Eq. (4.4), the maximum of the profile can be misaligned with the source location. In Figure 4.7 to Figure 4.10 a vertical line is indicating the source location. As the figures show, the symmetry axis of the Gaussian distribution is in almost all cases shifted with respect to the source location.

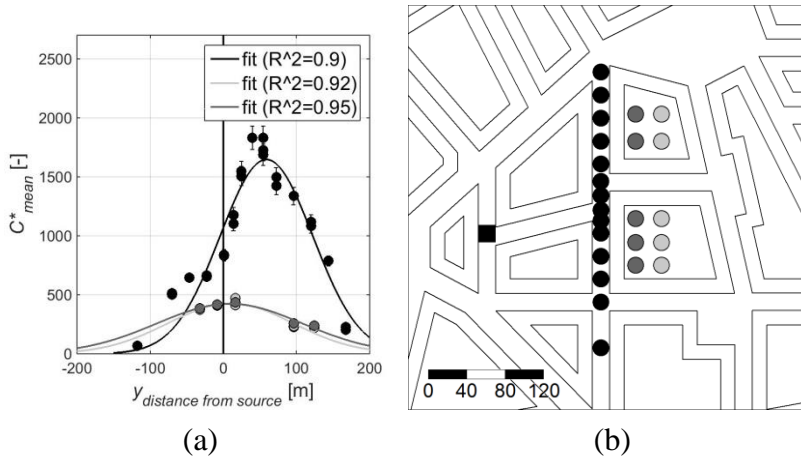


Figure 4.7 Lateral mean concentration profiles measured at half-building height in the Michelstadt model (a). The fits of the simplified Gaussian distribution in y direction are indicated with lines. The locations of the source (square) and measurements (circles) within the model (b).

Similar to the longitudinal profiles, the Gaussian distribution gives a good fit not only for the lateral profiles within the same street canyon (Figure 4.7 and Figure 4.10), but also for profiles, where the measurement points are separated by buildings (Figure 4.7 and Figure 4.9). However, not all lateral profiles can be well modeled by Eq. (4.4). For the results shown in Figure 4.10 as well as Figure 6.5 and Figure 6.6 in Appendix A the quality of the fit is significantly lower, than for the other lateral profiles shown in this thesis.

For the Michelstadt case, the fits are significantly better above the buildings (Figure 4.8) compared to those at half-building height. The same cannot be said about the measurements for the Hamburg test case (Figure 4.9). This is probably due to the smaller height difference between the profiles of Figure 4.9.a and b (10.5 m) compared to the height difference of the profiles in the Michelstadt case (45 m) and that in case of the Hamburg model, for both Figure 4.9.a and b the Gaussian distribution gives a nearly perfect fit, which makes them hard to compare.

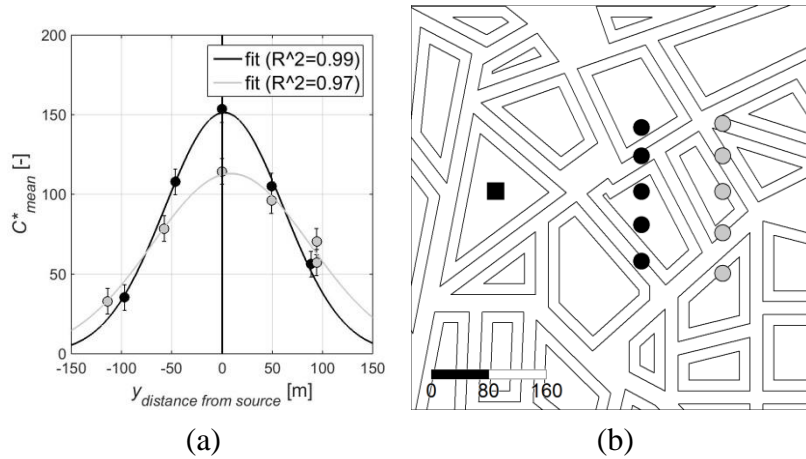


Figure 4.8 Lateral mean concentration profiles measured above the buildings of the Michelstadt model at 52.4 m in full scale (a). The fits of the simplified Gaussian distribution in y direction are indicated with lines. The locations of the source (square) and measurements (circles) within the model (b).

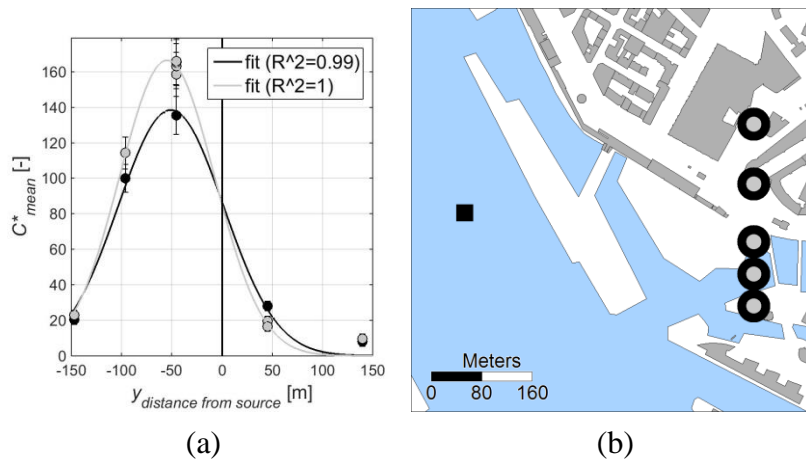


Figure 4.9 Lateral mean concentration profiles measured at pedestrian height (black) and at 12.6-m height (gray) in full scale in the Hamburg model (a). The fits of the simplified Gaussian distribution in y direction are indicated with lines. The locations of the source (square) and measurements (circles) within the model (b).

Eq. (4.5) is fitted on the measured vertical mean concentration profile (Figure 4.11 and Figure 4.12). The Gaussian distribution gives a reasonable fit for the measurements above the buildings; however, the fit within the street canyons is often less concise (e.g. Figure 4.11.b).

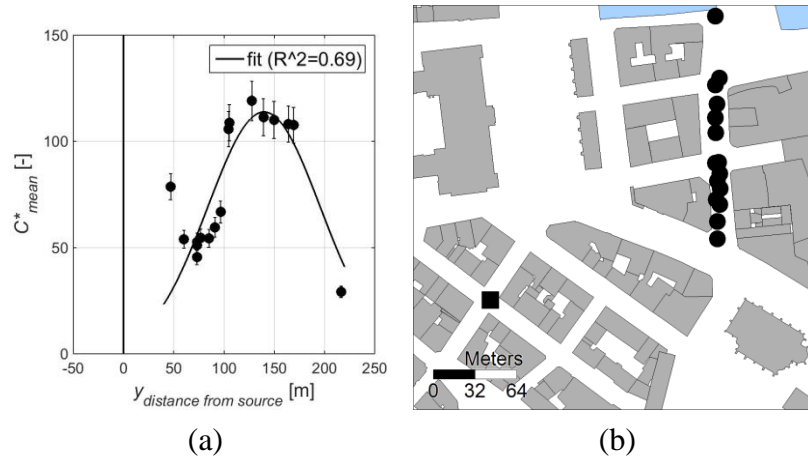


Figure 4.10 Lateral mean concentration profile measured at pedestrian height in the Hamburg model (a). The fit of the simplified Gaussian distribution in y direction is indicated with a black line. The locations of the source (square) and measurements (circles) within the model (b).

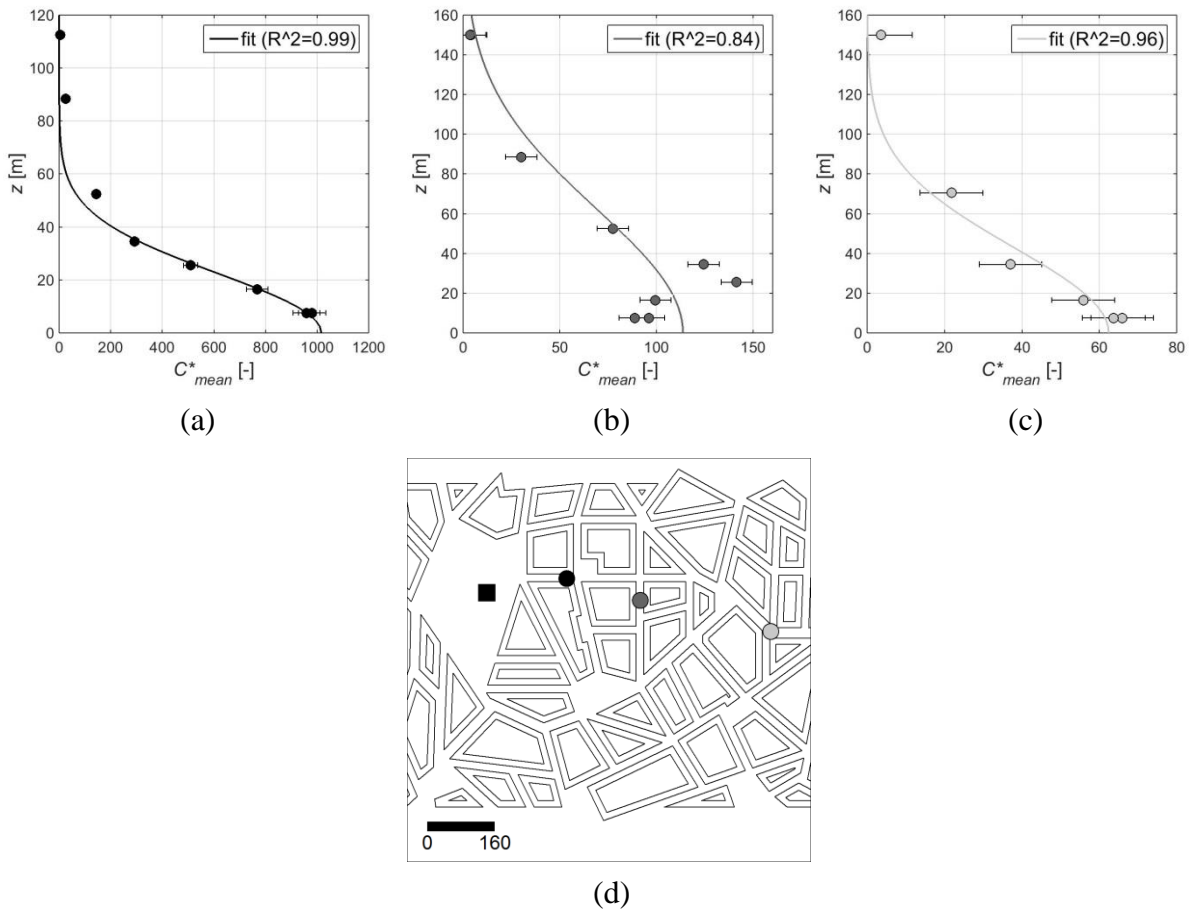


Figure 4.11 Vertical mean concentration profiles measured within the Michelstadt model. The fits of the simplified vertical Gaussian distribution are indicated with lines. The locations of the source (square) and measurements (circles) within the model (b).

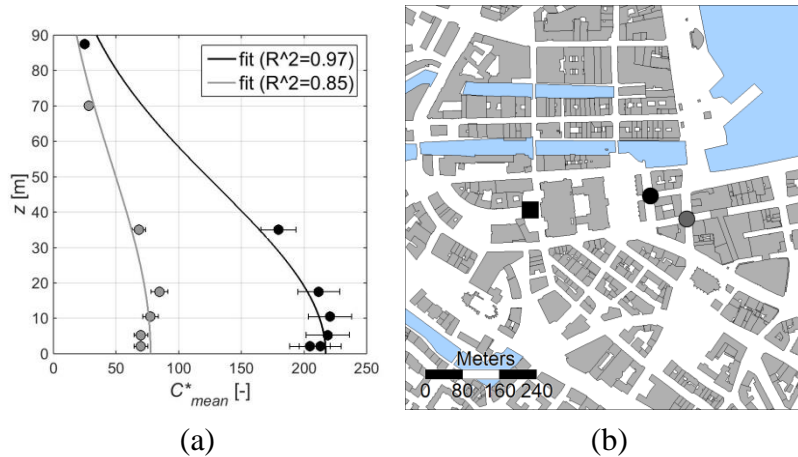


Figure 4.12 Vertical mean concentration profiles measured within the Michelstadt model. The fits of the simplified vertical Gaussian distribution are indicated with lines. The locations of the source (square) and measurements (circles) within the model (b).

It can be concluded that the equations derived from the Gaussian distribution give reasonable fits for the mean concentration profiles in each direction; however, the quality of the fits on the lateral concentration profiles is worse, than in longitudinal and vertical directions. For the lateral profiles an extra degree of freedom was necessary to introduce, because the maximum of the profile is often substantially misaligned with the source location due to the influence of the building geometry.

Although numerous assumptions of the Gaussian plume model do not apply for urban environments, the Gaussian distribution still seems to fit quite well for the measured mean concentration profiles. Nevertheless, the goodness of the fits in Figure 5.2 to Figure 5.12 does not imply that a Gaussian plume model would give such precise predictions. The parameters for Eq. (4.3 to 4.5) were determined based on the best fit on the measurement results. For Gaussian modeling, the parameters must be defined beforehand.

The estimation of the parameters in Eq. (4.1) is more difficult for an urban environment, than for flat-open terrain or above homogeneous roughness. Different methods exist to predict the parameters of the Gaussian plume model for different meteorological and roughness conditions, described for example by Hanna et al. (1982). The evaluation of these methods and suggestions on parameter prediction based on the measurement results could be the next step; however, it is out of the scope of this thesis.

It is also worth noting that the fits in all directions are generally better above the buildings than within the geometry. This is not surprising, since the higher the measurements are, the more homogeneous the turbulence is going to be, and the closer we get to fulfil the basic assumptions of the Gaussian plume model. This is an important message for validation exercises. If a model will be applied to predict the concentration field at pedestrian level, the validation should focus on the predictions at this height, because providing good results well above the buildings does not necessarily imply that the model can predict the concentration within the geometry similarly well.

Gaussian models are often used in emergency situations due to their fast speed and easy applicability. However, nowadays more advanced models are already available with similar benefits. As an example, CT-Analyst is based on a pre-calculated flow field using LES. Only the transport has to be predicted on-site, which can be done by a less complex model, such as Gaussian or Lagrangian. Due to the high precision of the flow field, the effects of the urban geometry on the transport processes are considered in detail, whereas a classical Gaussian model considers the city geometry as a parameter in the equation.

4.1.2 Frequency distribution of concentration

In the previous chapter, the spatial concentration distribution was described using equations derived from the Gaussian plume model. The Gaussian plume model considers only one concentration value for each location. However, due to the transient processes described in Chapter 2.2, the measured concentration signal is quasi-stationary even for constant continuous releases. Therefore, the concentration at a measurement location can be better described by a frequency distribution of the measured values, than with a single value (Chatwin, 1982). Most numerical codes used to model accidental releases predict only the first two moments of the concentration distribution. If a general probability density function (PDF) could be found that describes the concentration distributions at each measurement location, this could help the prediction of the whole distribution based on the first two moments.

Describing the frequency distributions using probability density functions

The idea to describe the frequency distributions of concentration measurements by probability density functions originates from Chatwin (1982). Since then, many attempts were made to find a general PDF, which matches all types of concentration measurements, or to introduce very specific ones for an individual dispersion scenario. Some examples from literature are listed in Table 4.1. Finding the optimal PDF is not straightforward, since the shape of the distribution is affected by different factors, such as the fluctuation intensity or the intermittency (Klein et al., 2010a). Mylne (1992) points out, that some PDFs are too complex and case specific to be generally applicable. The better fit of these complex PDFs compared to classical distribution functions is most likely caused by greater mathematical flexibility, rather than physical appropriateness. As shown in Table 4.1, the most commonly applied PDFs to model the measured distributions are the exponential, lognormal, clipped-normal, gamma and clipped-gamma distribution functions.

Most studies listed in Table 4.1 were carried out in a homogeneous turbulent flow field. As already described in Chapter 2.2.1, the flow field in an urban area is more complex and highly inhomogeneous. This makes the generalization of concentration distributions even harder.

Table 4.1 Literature overview on describing concentration measurements with PDF's.

First author	Year	Method	Fitted PDF	Conclusions
Yee	1990	field (flat terrain)	lognormal, clipped-normal, exponential, g- and h-distributions	g-and h-distributions give the best fits (clipped-normal provides a conservative prediction)
Mylne	1991	field (flat terrains with various turbulence levels)	exponential, clipped normal	clipped normal gives a better result overall, but exponential is better for high intermittency
Mylne	1992	a comment on Yee (1990) and Yee (1991)		compared to other PDFs, the better fits of g- and h-distributions reflect greater mathematical flexibility, not their physical meaning
Yee	1993	water channel (homogeneous roughness)	exponential, lognormal, clipped-normal, gamma, Weibull, conjugate beta, and K-distributions	none was adequate for the whole concentration field, but Weibull was the best fit for the centerline measurements
Schopflocher	1998	WT (model of Thorney Island)	composite of gamma and GEV	gives good result, but they note that other combinations might be useful to explore
Munro	2001	field (flat grassland)	Method 1: GEV with Weibull and beta; Method 2: GPD; Method 3: from mean excess plots	Method 1 is the best, where applicable
Schopflocher	2002	WT (grid turbulence)	4-parameter function using a mixture of beta densities	the high concentration range is well represented
Weil	2002	buoyant plume dispersion in a convection tank	gamma and clipped-normal	gamma was a reasonable and better fit than the clipped-normal in general
Ma	2005	field experiments in coastal regions	gamma, clipped-normal, modified clipped-gamma	modified clipped-gamma performed best, clipped-normal gave the poorest fit, but still reasonable
Xie	2007	WT and LES (rough wall)	GPD	generally good fit
Mole	2008	WT (grid turbulence)	GPD (using a linear fit to define the moments)	"good first guess" for the ratio of maximum and mean concentration
Yee	2008	water channel (five different types of obstacle arrays)	clipped-gamma	both the lower and upper tails in each geometry were well predicted
Klein	2010b	field (Joint Urban 2003)	clipped-gamma (2- and 3-parameter)	3-parametric clipped-gamma has not shown significant improvement in comparison to the 2-parametric model
Yassin	2011	WT (homogeneous urban-like roughness)	normal, lognormal	non-Gaussian behavior, lognormal provides better fit
Nironi	2015	WT (homogeneous roughness)	gamma	good approximation

The quality of the fit of several traditional PDFs was investigated for the concentration measurements of the Michelstadt and Hamburg data sets. In Figure 4.13 the fitted normal, clipped normal, lognormal, exponential and gamma PDFs and cumulative distribution functions (CDFs) are plotted. Depending on the shape of the measured distribution, different PDFs are suitable. In Figure 4.13.a, the measured distribution is highly skewed with a peak at 0. The normal, clipped-normal and lognormal distributions cannot model this behavior and predict a maximum probability above 0. Although the exponential PDF performs well in modeling skewed distributions (e.g. Figure 4.13.a), it has difficulties with moderately skewed distributions such as Figure 4.13.b. The gamma distribution seems to be a good compromise, which can model both cases well. However, there are other examples, such as the bimodal concentration distribution plotted in Figure 4.13.c, where all PDFs fail to follow the measured distribution.

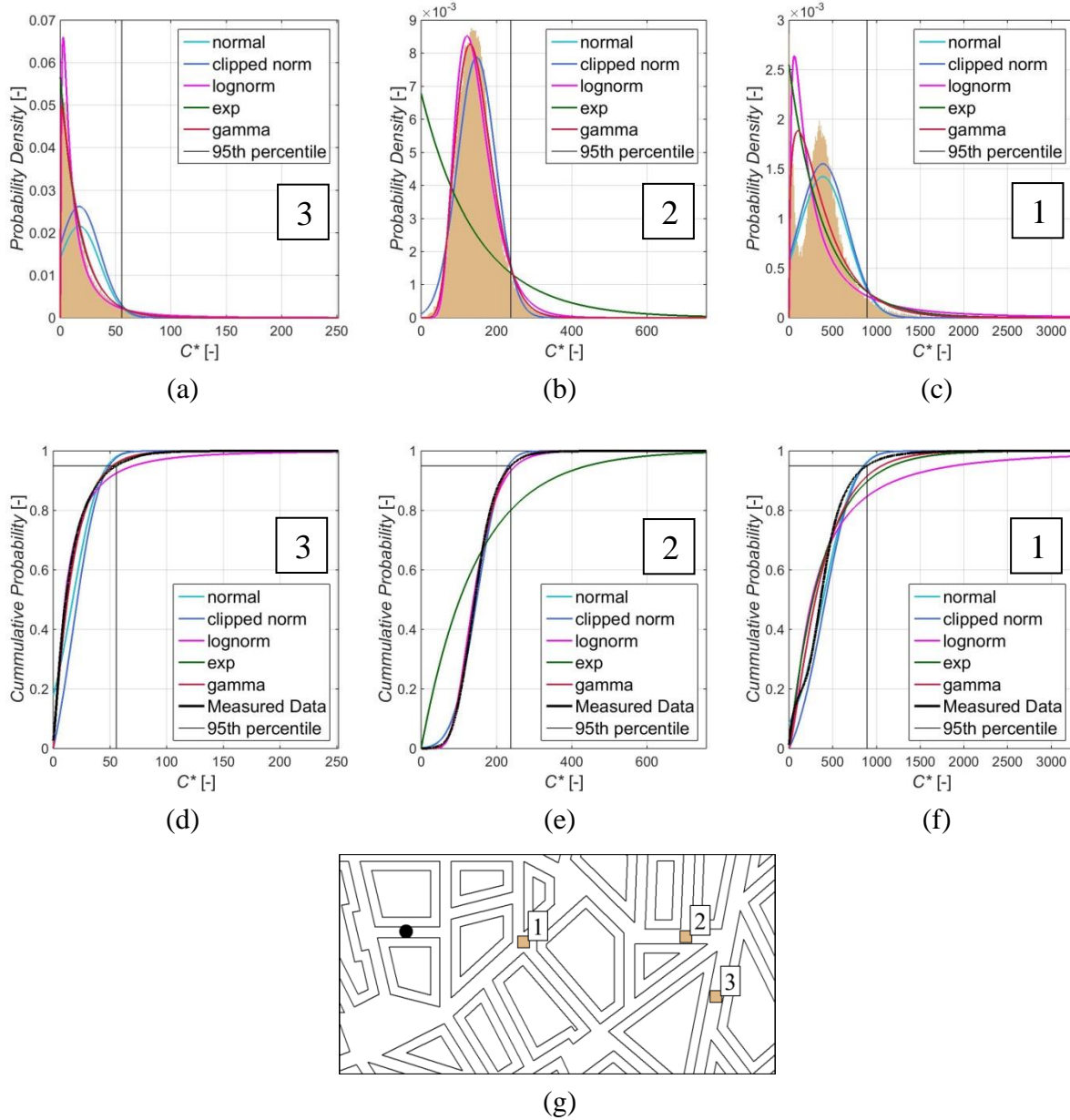


Figure 4.13 Normal, clipped normal, lognormal, exponential and gamma PDFs (a-c) and CDFs (d-f) fitted on measurement data from the Michelstadt campaign. The measured concentration distribution and its 95th percentile are also plotted. The distribution of the measured data for Figures a-c is indicated with brown color. The measurement locations are shown in (g).

Scatter plots help to further investigate and compare the accuracy of the fits of the different PDFs (Figure 4.14). As an example, the observed and predicted 95th percentile of the concentration distribution was selected for comparison. The predictions seem to be worse for small concentrations, especially those derived from the normal PDF. For higher concentrations, especially for the Hamburg campaigns the predictions are much better. According to the scatter plots, the gamma distribution provides the most accurate predictions of the 95th percentiles.

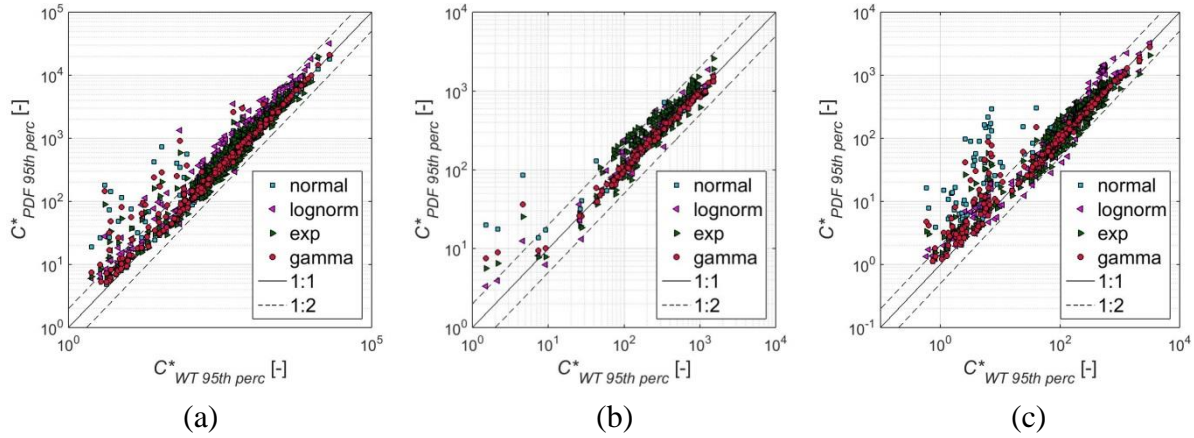


Figure 4.14 Scatterplots of the 95th percentiles of the measured and modeled concentration distributions for the Michelstadt data set (a) and the new (b) and previous (c) campaign of the Hamburg measurements.

Scatterplots are difficult to evaluate quantitatively and even qualitatively if the number of data points is high. Therefore, to further analyze the predictions of the 95th percentiles of the concentration distributions based on different PDFs, statistical metrics are applied. The fractional mean bias (FB):

$$FB = \frac{2\overline{(C_o - C_p)}}{C_o + C_p}, \quad (4.6)$$

the normalized mean-square error (NMSE):

$$NMSE = \frac{\overline{(C_o - C_p)^2}}{C_o C_p} \quad (4.7)$$

and the fraction of predictions within a factor of two of observations (FAC2) were suggested by Hanna and Chang (2012) to evaluate urban dispersion models. These metrics were applied in many studies already, such as COST ES1006 (2015b), Gariazzo et al. (2015), Moonen et al. (2013) and Kochanski et al. (2015). The lower the NMSE and the absolute value of FB and the higher the FAC2 value, the better the prediction. If the FB is negative, it means that the evaluated model (here the PDF) is overpredicting, and if the FB is positive, the model is underpredicting the measured value. The FAC2 value represents the fraction of points in the scatter plots of Figure 4.14 that fall within the 1:2 lines. Since most of the points fall within these lines, the FAC2 value is close to unity, suggesting high-quality predictions.

The acceptance criteria of these metrics according to Hanna and Chang (2012) are $|FB| < 0.67$, $NMSE < 6$, $FAC2 > 0.3$. It should be noted, that these criteria were defined for urban dispersion models, therefore are quite weak for evaluating PDFs. However, it gives a good comparison to see how well the PDFs predict the 95th percentile of the concentration distribution.

The PDFs shown in Figure 4.13 and Figure 4.14 were estimated based on the best fit on the whole measured concentration distributions. However, the PDFs investigated in this thesis can

also be defined based on the first two moments (mean and variance) of the distributions. In Figure 4.15 to Figure 4.17 and Table 4.2 the statistical metrics are plotted and listed for different PDFs fitted on the measured concentration distributions or estimated from the first two moments.

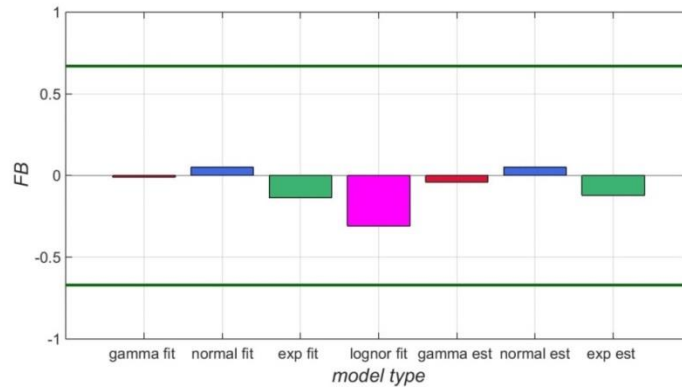


Figure 4.15 Fractional mean bias of the 95th percentile from the fitted on the whole concentration distribution (fit) and estimated from the first two moments (est) PDFs for all measurements. The acceptance zone defined for urban dispersion models is within the green lines.

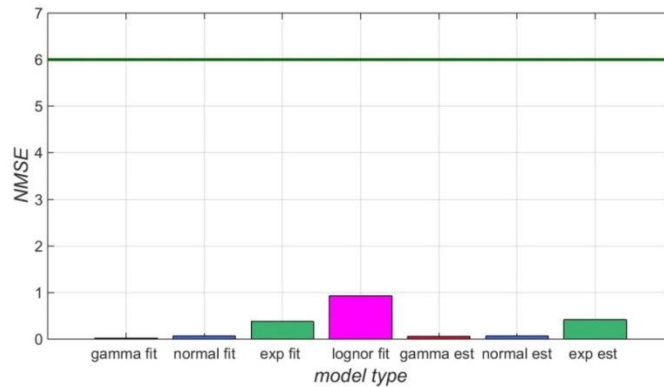


Figure 4.16 Normalized mean-square error of the 95th percentile from the fitted on the whole concentration distribution (fit) and estimated from the first two moments (est) PDFs for all measurements. The acceptance zone defined for urban dispersion models is below the green line.

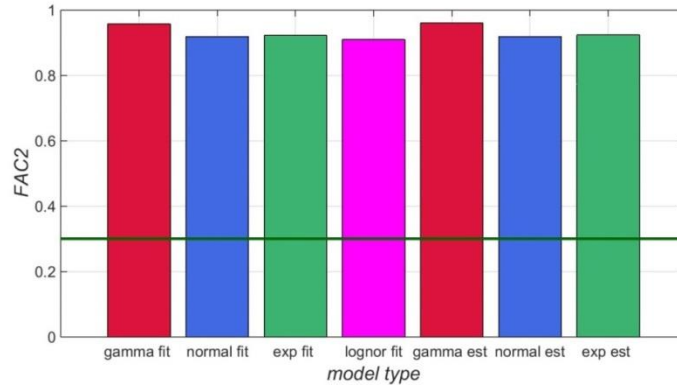


Figure 4.17 Fraction of the 95th percentile from the fitted on the whole concentration distribution (fit) and estimated from the first two moments (est) PDFs for all measurements. The acceptance zone defined for urban dispersion models is above the green line.

According to Figure 4.15 to Figure 4.17 and Table 2.1 all PDFs (both fitted and estimated) provide sufficiently accurate predictions for the 95th percentiles of the concentration distributions. They all satisfy the acceptance criteria defined by Hanna and Chang (2012). The gamma PDF outperforms all the other models with its exceptional results. All three metrics show the superiority of the gamma PDF in comparison to the other models. It is surprising that in most cases the estimated gamma PDF gives an even better prediction of the 95th percentile of the concentration distribution, than the fitted gamma PDF.

Table 4.2 Statistical metrics of the 95th percentile prediction for all measurement campaigns and PDFs.

Metric	Data set	fitted				estimated		
		gamma	normal	exponential	lognormal	gamma	normal	exponential
FB	MS	-0.016	0.055	-0.114	-0.337	-0.048	0.055	-0.096
	HH previous	0.003	0.040	-0.095	-0.307	-0.021	0.040	-0.076
	HH new	0.006	0.044	-0.297	-0.152	-0.031	0.044	-0.295
	All data sets	-0.010	0.051	-0.137	-0.309	-0.041	0.051	-0.121
NMSE	MS	0.014	0.045	0.249	0.619	0.043	0.045	0.277
	HH previous	0.030	0.055	0.282	0.772	0.024	0.055	0.326
	HH new	0.011	0.023	0.259	0.075	0.006	0.023	0.261
	All data sets	0.022	0.067	0.376	0.928	0.060	0.067	0.416
FAC2	MS	0.980	0.966	0.973	0.925	0.993	0.966	0.973
	HH previous	0.930	0.862	0.911	0.875	0.922	0.862	0.914
	HH new	0.983	0.967	0.867	0.961	0.989	0.967	0.867
	All data sets	0.958	0.920	0.923	0.910	0.960	0.920	0.924

It should be noted that it is also possible to evaluate higher moments of the concentration distributions to further specify the PDFs. However, the more complex the definition of the PDFs is, the less generalizable they become and as mentioned before with reference to Mylne (1992), a

better fit does not necessarily mean physical appropriateness. Using only the first two moments to describe a concentration distribution has also the benefit, that these moments are usually predictable by CFD models (e.g. Efthimiou et al., 2015). Therefore, if a CFD model can predict the mean and the variance properly, then the whole concentration PDF can be predicted.

Correlation of the statistical parameters

To further investigate why the estimated gamma PDF gives generally better predictions for the 95th percentile of the concentration distribution than the fitted gamma PDF, the correlations between the mean and the standard deviation (Figure 4.18.a) and the mean and 95th percentile (Figure 4.18.b) were plotted. Both relationships are close to linear, with a power exponent of 0.95 and 0.98. The correlation between mean and the standard deviation of the concentration is not very strong ($R^2=0.81$). However, the relationship between the mean and the 95th percentile of the concentration distribution is much stronger ($R^2=0.93$). It is also interesting that the results of the different data sets fall very close to each other.

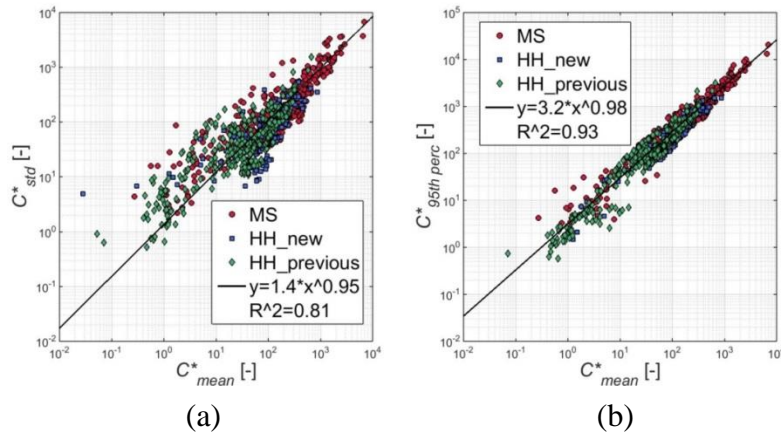


Figure 4.18 The correlation between the mean and the standard deviation (a) and the mean and 95th percentile (b) of the measured concentration distributions. The black lines indicate the best fit on the whole data set.

The results show that if the first two moments of the concentration distributions can be predicted by a numerical model, it is possible to provide a good prediction of the higher concentrations using a general PDF estimated from these moments. The prediction of the percentile ranks using PDFs introduces a low uncertainty based on statistical metrics compared to the usual uncertainty of a dispersion model. If only the first moment is available from a dispersion model (such as the Gaussian plume model described in Chapter 4.1.1), the higher concentrations can still be predicted with relatively low additional uncertainty due to the strong correlation between the mean and the higher percentile ranks of the concentration distributions.

4.1.3 Extreme value analysis of the frequency distribution

During an accidental release in an urban area, the rescue personnel needs information on the possible worst case scenario, including the extreme value of the concentration distribution, i.e. the highest concentration that can occur at a location. Measurements and time-dependent numerical simulations both have limited durations. During the investigated interval, it is likely that the expected extreme concentration will not occur.

As described in Chapter 4.1.2 probability density functions can be used to describe the concentration distribution at a location during a continuous release. However, the PDFs that are commonly applied to describe the concentration distributions have no upper limit (see Table 4.1), therefore the extreme value cannot be derived from them. These PDFs are mainly used to model the bulk of the concentration distribution.

There are two basic theorems to estimate the extreme value of a distribution by approximating the distribution of the high concentrations (Bensalah, 2000). The time series can be separated into blocks and distribution of the block maxima can be modeled by the Generalized Extreme Value Distribution (GEV). The second theorem states that the Generalized Pareto Distribution (GPD) models the upper tail of the whole distribution. Both theorems of the extreme value theory are examined in this Chapter. The two methods are demonstrated on the concentration distribution measured at a selected location (S2P1) from the Michelstadt data set (Figure 4.19).

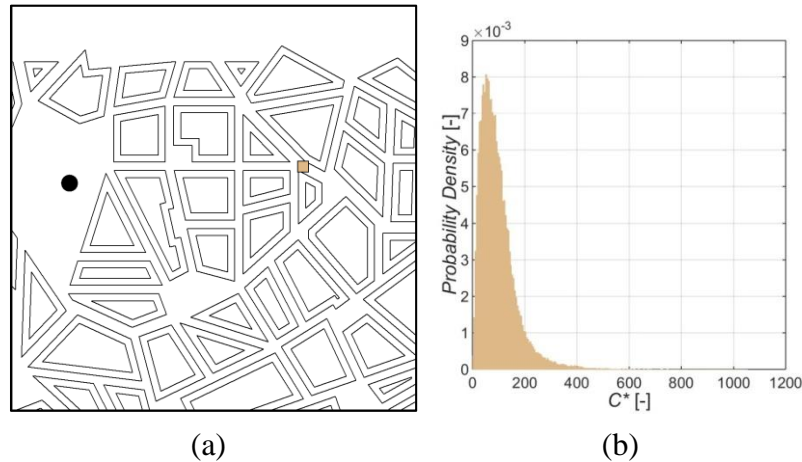


Figure 4.19 The location of the S2 source (black circle) and the measurement point S2P1 (square) in the Michelstadt model (a). The probability distribution of the measured concentration at S2P1 (b).

Generalized Extreme Value Distribution

According to the Fisher-Tippett Theorem (Fischer and Tippett, 1928 and Gnedenko, 1943), the sample block maxima of a sequence of independent and identically distributed random variables converge to the Gumbel (Type I), Fréchet (Type II, also known as the Fréchet-Pareto

case, see e.g. Beirlant et al., 2004) or Weibull (Type III) distributions. These three types of distributions are combined in the GEV distribution (Coles, 2001):

$$G(z) = \begin{cases} \exp \left\{ - \left[1 + \xi \left(\frac{z - \mu}{\sigma} \right) \right]^{-\frac{1}{\xi}} \right\} & \text{if } \xi \neq 0 \\ \exp \left\{ \exp \left[- \left(\frac{z - \mu}{\sigma} \right) \right] \right\} & \text{if } \xi = 0 \end{cases} \quad (4.8)$$

such that $1 + \xi(z - \mu)/\sigma > 0$, where $-\infty < \mu < \infty$ is the location parameter, $\sigma > 0$ is the scale parameter and $-\infty < \xi < \infty$ is the shape parameter of the distribution.

The signum (Eq. 4.9) function of the shape parameter decides to which type of the three distributions the GEV corresponds to. If $sign(\xi)$ is -1, 0 or 1, the GEV will correspond to the Type I, II or III respectively.

$$sign(x) = \begin{cases} -1 & \text{if } x < 0 \\ 0 & \text{if } x = 0 \\ 1 & \text{if } x > 0 \end{cases} \quad (4.9)$$

One of the criteria of the Fisher-Tippett Theorem is the independence of the variables. A measured concentration time series is a stationary, dependent sequence (see later at Figure 4.23.a). However, by selecting a large-enough block size, independence can be assured, and according to Roberts (1979), (in case of air quality data) the criterion of independence for a GEV distribution is not crucial.

Selecting a block size to fit the GEV distribution is an arbitrary choice. The common technique (see e.g. in the paper of Munro et al., 2001) is to test the sensitivity of different parameters or quantiles to the block size. Figure 4.20 shows an example of the sensitivity of the shape and scale parameters depending on the block size with 95% confidence intervals. The confidence intervals were calculated based on the maximum likelihood estimation (MLE) and the profile likelihood estimation. The two estimation methods give very similar results of the confidence intervals.

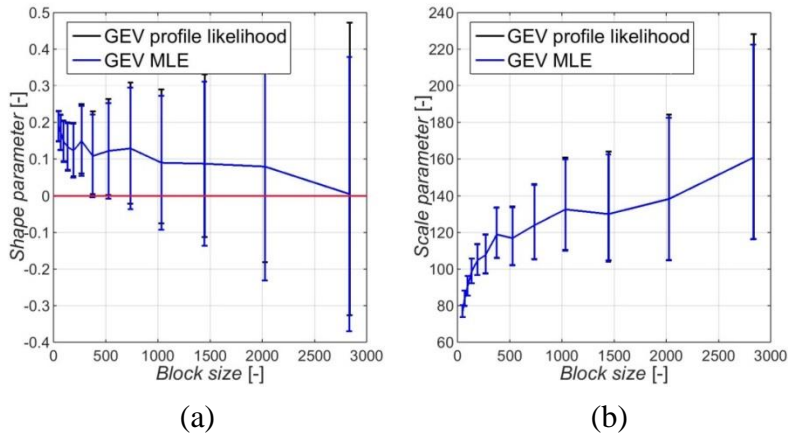


Figure 4.20 The sensitivity of the shape parameter (a) and scale parameter (b) of the GEV distribution, depending on the block size.

According to Figure 4.20, it is safe to say that in case of this particular measurement, above a block size of 400, the variation of the parameters is negligible compared to the confidence interval widths.

Figure 4.21 shows the GEV fitted on the block maxima of the concentration time series measured at the location shown in Figure 4.19.a in case of a block size of 400. Figure 4.22 shows the probability density of the shape parameters of the GEV fits on all of the time series of the Michelstadt data set using a block size of 400, 450 and 500 respectively. The shape parameter distributions with different block sizes look similar to each other. However, it should be noted that the optimal block size should be defined for each measurement separately. Nevertheless, finding the best GEV fit for each measured concentration distribution is not the aim of this work, therefore individual optimization of the block size for each measurement will be spared.

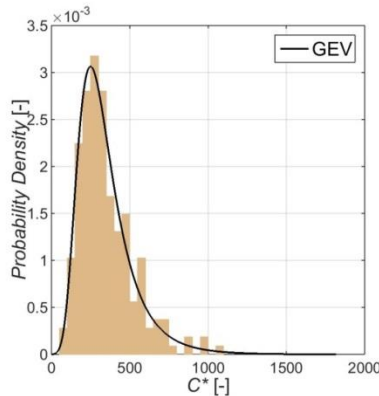


Figure 4.21 GEV distribution fitted on the block maxima of the concentration time series with block size 400 for the S2P1 case.

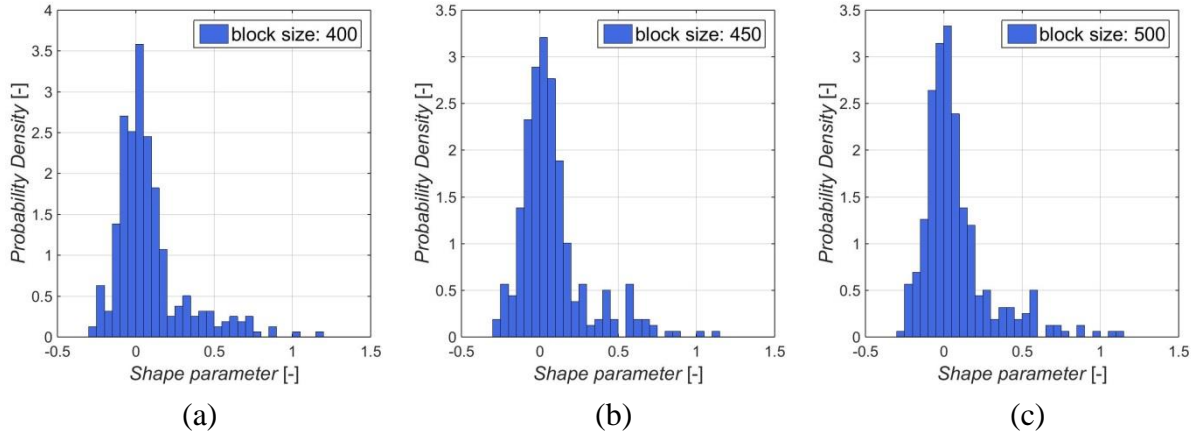


Figure 4.22 Distribution of the shape parameters of the GEV distributions based on all Michelstadt measurements with block size 400 (a), 450 (b) and 500(c).

Generalized Pareto Distribution

According to the Pickands-Balkema-de Haan Theorem (Pickands, 1975; Balkema and de Haan, 1974), with a sufficiently high threshold (u), the part of the distribution of a sequence of independent and identically distributed random variables which is above the threshold, can be approximated by the GPD function:

$$H(y) = 1 - \left(1 + \frac{\xi y}{\sigma_*}\right)^{-\frac{1}{\xi}}, \quad (4.10)$$

where $0 < \mu < \infty$ is the location parameter, $0 < \sigma < \infty$ is the scale parameter and $-\infty < \xi < \infty$ is the shape parameter. σ_* is the modified scale parameter (Coles, 2001):

$$\sigma_* = \sigma + \xi(u - \mu) \quad (4.11)$$

Since the GPD is fitted on the whole right tail of the concentration distribution (not just the block maxima), dependence of the data becomes an issue. Figure 4.23.a shows a part of the time series, which illustrates that high concentrations tend to cluster; therefore, the sequence cannot be treated as independent.

To treat the problem of dependence, declustering was applied. From each consecutive time step, where the concentration stays above the chosen threshold, only the maximum concentration is kept. A disadvantage of declustering is that it significantly decreases the size of the data.

As selecting the block size for the GEV distribution, the selection of the threshold for the GPD is also somewhat arbitrary. The techniques include looking at the quantile-quantile (QQ) plots, the mean excess function (MEF), or similarly to the GEV distribution, examining the sensitivity of different parameters or quantiles to the threshold variation.

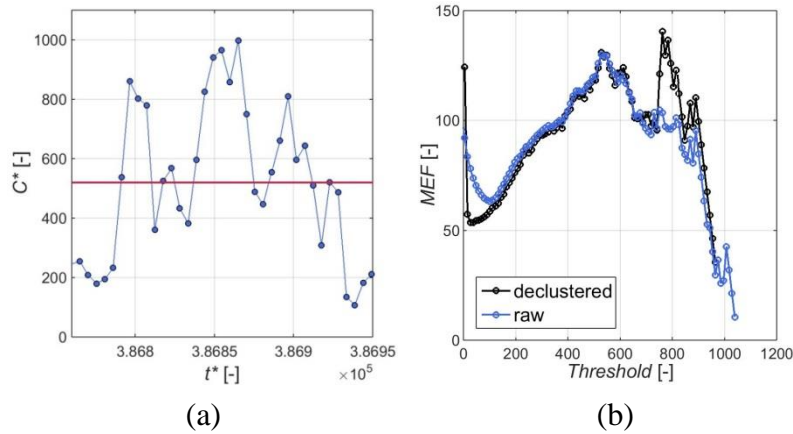


Figure 4.23 A part of the time series measured at S2P1 location (a). The red line is at $C^*=520$. The mean excess function (MEF) plot of the S2P1 measurement (b).

The mean excess function plot shows the average difference between the concentration values and the threshold (overshoot) plotted against the threshold (Munro et al., 2001). In case of an exponential distribution, the MEF plot is a straight line. The MEF of a heavy-tailed distribution will have a positive gradient, whereas a short-tailed distribution has a MEF with negative slope (McNeil, 1997). The MEF plot tends to become very irregular at high threshold values, because the number of exceedances above the threshold will be small (Munro et al., 2001).

The QQ plot of a distribution compared to the exponential distribution is again an indicator of the tail properties. The points on the QQ plot of an independent and identically distributed data following an exponential distribution should be approximately along a straight line. A concave departure indicates a heavier tailed distribution, whereas convexity is an indicator of shorter tails (McNeil, 1997).

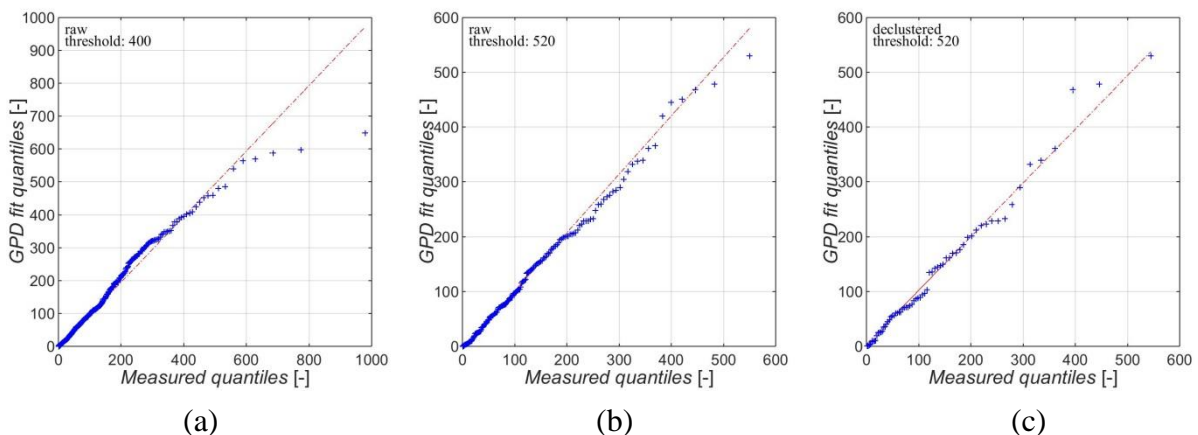


Figure 4.24 The quantile-quantile (QQ) plots of the raw data (a, b) and the declustered data (c) with $u=400$ (a) and $u=520$ (b, c) thresholds.

Figure 4.23 shows the MEF plot, while Figure 4.24 shows the QQ plots of the concentration distribution measured at S2P1 location. The threshold-sensitivity of the shape and scale parameters is plotted in Figure 4.25 in case of the raw (clustered) and declustered data. Judging from these figures, $u=520$ is a possible threshold for a GPD fit for the S2P1 measurement.

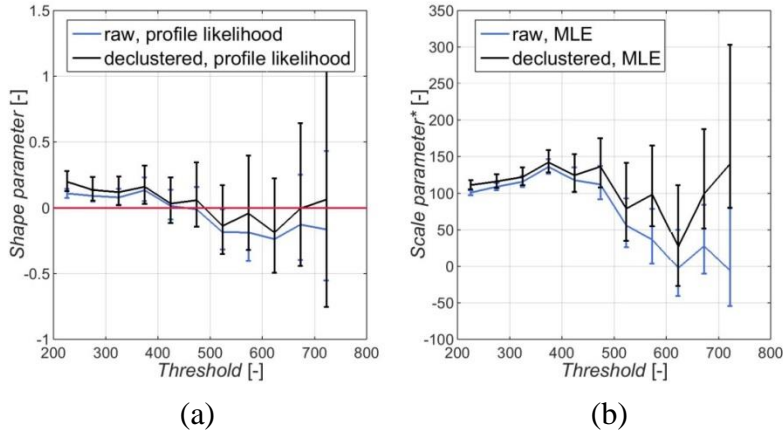


Figure 4.25 The sensitivity of the shape parameter (a) and scale parameter (b) of the GPD for the S2P1 measurement, depending on the threshold.

In Figure 4.26, the GDP is fitted on the raw and declustered data with the chosen threshold of $u=520$. It is clear to see, that declustering (Figure 4.26.b) decreases the number of data points, causing an irregular probability density plot.

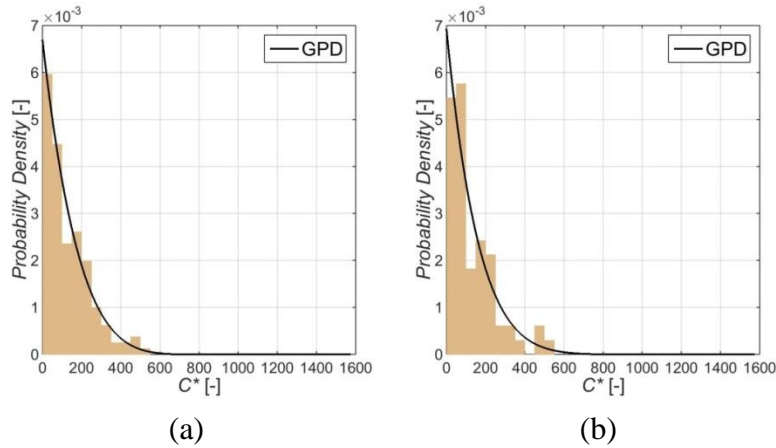


Figure 4.26 GPD fitted on the upper tail of the concentration time series distribution with threshold $u=520$ for the S2P1 measurement without declustering (a) and with declustering (b).

In Figure 4.27, the probability density of the shape parameters of the whole Michelstadt data set is shown with different threshold definitions. Due to the high variability in the spread of the concentration distributions depending on the measurement location, relative thresholds were defined. Similar to the problems of defining a general block size for the GEV distribution (Figure 4.22), to carry out a proper extreme value analysis each measured concentration distribution

should be individually examined as it was done for the S2P1 measurement as an example. Choosing a general characteristic for all the distributions (such as a percentile, as in Figure 4.27) is not the correct method to define the threshold of the GPD. However, it is not the aim of this thesis to find the best fitting GPD for each measurement of the data sets, but to investigate the possibility of predicting finite extrema. Figure 4.22 and Figure 4.27 show that the distributions of the shape parameters do not change significantly, when different block sizes or thresholds are applied. This means, that the shape parameter is not sensitive to the change in block size or threshold within the investigated interval. Therefore, an individual examination of the concentration distributions at each location would not change the shape parameter values significantly. On the other hand, Figure 4.27 shows that declustering generally increases the value of the shape parameter.

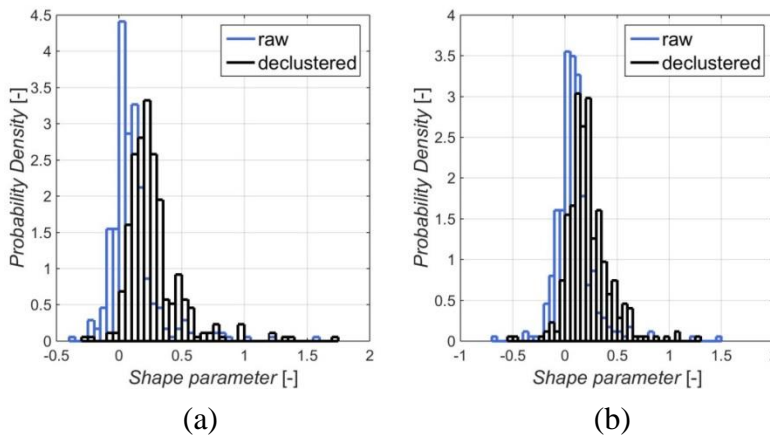


Figure 4.27 Probability density of the shape parameters of the GPD for the whole data set with the 98th percentile (a) and 99th percentile (b) as thresholds.

Finding a finite extremum

The GEV and GPD functions have finite extremes only, if the shape parameter is negative. Even though the finite concentration at the source suggests that the concentration at the measurement locations must have a finite upper limit, the shape parameters fall mostly above zero (see Figure 4.22 and Figure 4.27). Even the absolute values of the negative shape parameters are in most cases smaller than their confidence intervals (see Figure 4.20.a and Figure 4.25.a), making it impossible to reliably predict the finite maximum values based on the fits.

In the example of the measurement carried out at S2P1 location, the fitted GPD has a slightly negative shape parameter ($\xi=-0.11$) at $u=520$. Although this fit has a finite upper limit (1821), which is above the maximum measured concentration (1050), the confidence interval of the shape parameter is between -0.37 and 0.16 according to the profile likelihood estimation. Therefore, even with a slightly negative shape parameter it is very uncertain to provide a maximum concentration based on the measured time series.

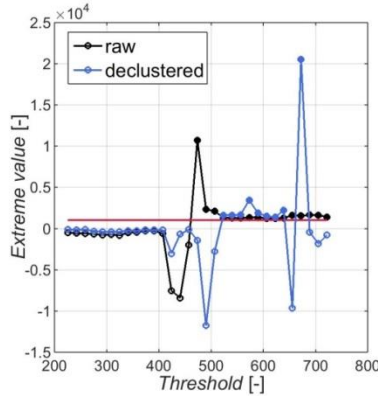


Figure 4.28 Prediction of the extreme value based on GPD fits with different thresholds. Filled symbols show the predictions with finite upper limit that are above the maximum of the measured distributions (indicated with a red line).

Figure 4.28 shows the predicted extreme values for the S2P1 measurement by considering different thresholds for the GPD fit. Figure 4.28 is consistent with the results shown in Figure 4.25. Where the shape parameter falls below 0, there is a finite upper limit with a reasonable extremum prediction. For the raw data (without declustering), the predicted extreme value is relatively constant above a threshold of $u=520$, whereas the predictions based on the declustered data have larger variability due to the smaller data size.

The results show that both the GEV distribution and the GPD can be fitted on the measured concentration distributions. However, in most cases it is not possible to predict the extremum due to the high values of shape parameters.

4.2 Residence time analysis based on short-term releases

Continuous and instantaneous releases are the two theoretical extrema of the release duration. In real life, accidental releases have a finite duration. If the finite duration is significantly shorter or longer than the characteristic times of the transport processes, it can be modeled as an instantaneous or continuous release respectively. If the release duration is finite, the concentration will decrease after the end of the release. The duration after the end of the release until the concentration decreases below a certain threshold is the residence (or retention) time. The evaluation of the residence time of a contaminant in this work is based on short-term release measurements. The method of characterization is presented in this Chapter, followed by a discussion of typical results.

4.2.1 Characterizing concentration decay measurements

The modeling of concentration decay requires the satisfaction of the experimental criteria related to continuous and puff release measurements. The release must be long enough to enable the identification of a quasi-stationary concentration plateau before the decay starts. However, the evaluation of the measurement is time dependent, focusing on the time series after the source is closed. Therefore, a sufficient number of repetitions are necessary to acquire a statistically representative ensemble of data.

The concentration decay measurements had longer release durations (approx. 10 s in model scale), than the puff releases in order to reach the desired quasi-stationary dispersion conditions. However, they were repeated sufficiently often (approx. 90 times), unlike continuous release measurements, where merely the duration of the release determines the statistical representativeness of the results.

Due to the relatively long release durations ($T_{rel} > 5at$), the dimensionless concentration (Eq. 3.13) applied for converting the continuous release measurements was considered while nondimensionalizing the concentration decay time series.

There are several articles addressing the subject of concentration decay with means of wind tunnel and field experiments, as well as with CFD. The methods of evaluation differ just as much as the technique to gather the data (see Table 4.3).

The common practice is to release traceable material from a source, which is then closed instantaneously. The concentration is measured until it falls below a certain threshold. The part of the time series representing the decay of the concentration is then evaluated. There are several techniques to characterize the time series of the concentration decay. Unlike a RANS model, the measurements are affected by the high variability of the flow field. Therefore, recording a ensemble of time series at each measurement location is mandatory to ensure statistical representativeness.

The concentration decrease is expected to follow an exponential decay function. Eq. (4.12) is the exponential function describing the decay of the dimensionless concentration.

$$\frac{dC^*(t^*)}{dt^*} = -\frac{1}{\tau^*} C^*(t^*). \quad (4.12)$$

The most commonly analyzed characteristic of the concentration decay time series is its time constant (τ^*). The time constant is either derived from the solution of the exponential decay function

$$C(t) = C_0 e^{-\frac{t}{\tau}}, \quad (4.13)$$

or from the C_0^* initial concentration:

$$C^*(\tau^*) = \frac{C_0^*}{e}. \quad (4.14)$$

The difference between the two methods is whether the initial concentration is considered to be a reliable constant acquired from the measurements (Eq. 4.14) or should be estimated by fitting Eq. (4.13) on the time series. In Eq. (4.13), C_0^* is considered as an unknown parameter to be estimated from the best fit, whereas in Eq. (4.14) it is defined based on the measurements. The average difference between the two evaluation methods for the first campaign of the Hamburg data set is 23% (Figure 4.30.a). Considering the high variability of the data and the influence of the averaging (Figure 4.30.b), the effect of the various time constant estimations is low. However, Figure 4.30.a shows the trend that the time constant of the fitted equation is in most cases larger than that obtained from Eq. (4.14), causing a systematic difference between the results.

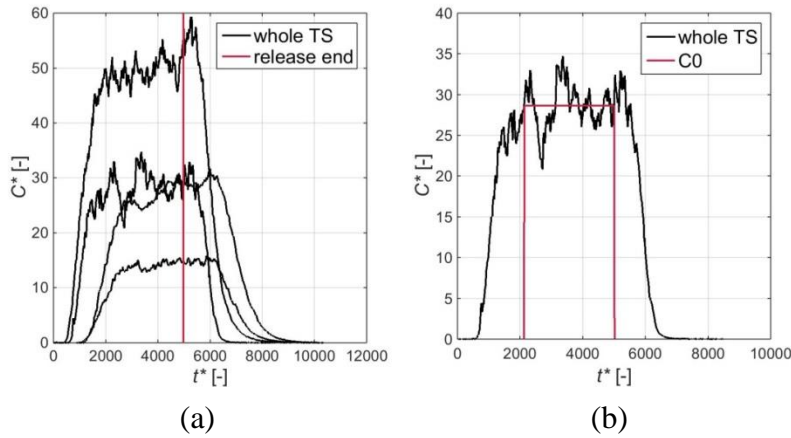


Figure 4.29 Averaged time series measured at different locations with identical release conditions; the end of the release is indicated with a red line (a). C_0 defined as the mean concentration between the time steps, when 20% and 80% of the total dosage has reached the measurement location (b). The period between the 20% and 80% of the total dosage is indicated with red lines.

The three main stages of processing the concentration decay time series are statistical analysis (such as averaging), defining the starting time of the decay (cutting) and evaluating the result (finding the time constant). Based on the criteria and the sequence of the stages of evaluation, the results can differ substantially.

Examples of criteria to define the starting time are the release duration, mean concentration, dosage, peak concentration, percentile, or one of these characteristics multiplied by a constant. A more detailed analysis of the different criteria and their effects on retention time estimates can be found in (Berbekar et al., 2015b).

Table 4.3 Literature overview on concentration decay evaluation techniques.

First author	Year	Method	How to measure/model?	What to average?	Where does the decay start?	What to compare?
Fackrell	1984	WT	point source (release duration not specified)	time constant (100-150/location)	not specified	time constant (Eq. 4.14)
Isaacson	1990	WT	point source (release duration not specified)	the original TS (6/location)	steady-state pre-drop concentration from averaged TS (if not possible, a range is applied)	dimensional and dimensionless time constant (Eq. 4.13)
Higson	1995	field	Dugway (1993): constant point source was shut (conc. decay was not the main purpose)	not specified	not specified	duration, dimensional and dimensionless time constant (Eq. 4.14)
Mavroidis	1999	field	Dugway (1995): 30 s steady state release	lateral spatial averaging, investigate the range of results	source switch-off	dimensional and dimensionless time constant (Eq. 4.14)
Doran	2006	field	JU2003: instantaneous releases	examine each TS separately, investigate the distribution	concentration first exceeds and remains above 50 ppt _v for at least 20 s	duration, time constant (Eq. 4.14), also multiplied by a constant (4.61)
Gomes	2007	WT	line source; release shut off instantaneously after "brief period of time"	the normalized TS (20/location)	decay TS is between 0.2-0.8 of normalized concentration (C ₀)	dimensional and dimensionless time constant (Eq. 4.13)
Yim	2009	CFD	RANS for flow field, URANS for dispersion	only one TS/location	steady-state concentration	time constant (Eq. 4.14)
Richmond-Bryant	2012	field	MID05, JU2003: 30-min releases	only one TS/location	"Time series intervals were designated to coordinate with the release times"	dimensional and dimensionless time constant (Eq. 4.13)
Mavroidis	2012	CFD	RANS (ADREA)	only one TS/location	steady-state concentration	dimensional and dimensionless time constant (Eq. 4.14)
Kipsch	2015	WT	short-term (6-8 s) releases from point sources	the original TS (100-150/location)	decay TS starts at 0.95 of the mean concentration	bandwidth and shape of the time series

The most common criterion to determine the starting time of the decay is the end of the release. However, often there is a time delay between the end of the release and the beginning of detectable concentration decay. Four averaged time series are plotted in Figure 4.29.a measured at different locations with identical mean release conditions. The end of the release is indicated with a red line. The drop of the concentration is delayed compared to the end of the release. Fitting the exponential equation (Eq. 4.13) to such a delayed decay curve will give a poor result. As Figure 4.29.a illustrates, the concentration decrease starts at different time steps after the release for each measurement location. It is therefore impossible to define a criterion, linearly dependent on the release duration to be applicable for each measurement. Nevertheless, to study the residence time of pollutants, the whole subsequent time series after the end of the release should be considered. This problem can be solved by separating the period after the release has

stopped, but the decay has not yet started from the actual concentration decay. During the evaluation of the residence time the whole time series after the end of the release was considered, but the exponential function was only fitted on the part, where the concentration decreases.

To obtain a single result instead of a distribution, a statistical evaluation is required. For this thesis, the concentration decay measurements are averaged, however the other statistical methods presented in Chapter 3.1.4 could also be applied instead. The statistical analysis can be carried out at different stages of the evaluation process. The raw or the normalized time series can be averaged, using the mean concentration trace for further analysis. Another method is to first find the starting time of the decay for each release and average only the parts of the time series following the starting time. Finally, the whole evaluation process can be carried out for each measurement, averaging only the distribution of the final results. A comparison of the evaluated time constants using the same method of evaluation, but averaging at different stages is shown in Figure 4.30.b. Stage 1 refers to averaging the whole raw time series. Stage 2 corresponds to averaging the normalized time series of the concentration decay already cut at the starting time. Stage 3 averages the time constants evaluated from each time series separately. Due to the high variability of time series resulting from relatively short release duration (Harms et al., 2011 and Berbekar et al., 2015a), the exponential function gives a poor fit to several of the single concentration decay time series. Therefore, taking the average of the time series before fitting the exponential function, results in parameters with higher statistical representativeness. Taking this into consideration, the averaging of the time series was the first step of the evaluation process used for this work (stage 1 averaging in Figure 4.30.b).

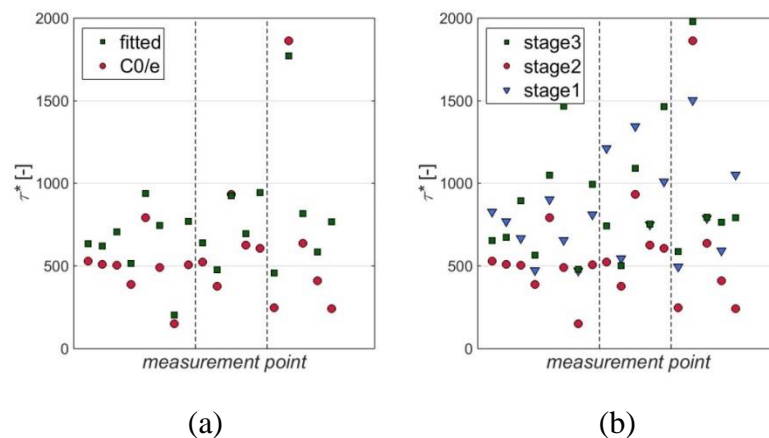


Figure 4.30 Time constants resulting from different methods of evaluation (a). Time constants resulting from the same method of evaluation, but averaging at different stages (b).

Based on the results and the considerations mentioned above, the time constant was defined as the duration between the end of the release and the time when the concentration reaches $1/e$ of the mean concentration of the plateau:

$$\tau^* = t^* \Big|_{C^*(t^*)=\frac{C_0^*}{e}} - t^* \Big|_{Q(t^*)=0}, \quad (4.15)$$

where Q is the flow rate of the release and $t^* \Big|_{Q(t^*)=0}$ refers to the end of the release. Therefore, the period after the release has stopped, but the decay has not yet started and the actual concentration decay are both considered in the time constant. However, the exponential function is fitted only on the time series after the concentration stays below the mean of the plateau. The mean of the plateau is defined as the mean concentration between the arrival time and the leaving time, taking 20% of the dosage as the relative threshold:

$$C_0^* = \frac{1}{\Delta t^*} \int_{t_{d20}^*}^{t_{d80}^*} C^*(t^*) dt^*, \quad (4.16)$$

where $\Delta t^* = t_{d80}^* - t_{d20}^*$ and t_{di}^* represents the time between the beginning of the release and when $i\%$ of the total dosage has reached the measurement location (Figure 4.29).

The resulting time series were normalized. The concentration of the i th time step from the mean of n independent concentration time series is defined as

$$C^*(t_i^*) = \frac{\frac{1}{n} \sum_{j=1}^n C_j^*(t_i^* + t^* \Big|_{Q(t^*)=0})}{C_0^*}. \quad (4.17)$$

4.2.2 Exemplary results of the concentration decay measurements

To illustrate that the concentration decay follows an exponential function, both Eq. (4.13) and Eq. (4.14) were fitted on the measured normalized mean concentration time series for a selected source location within the Hamburg model (Figure 4.31). The equations were fitted on the part of the measurement time series, where the concentration decreases. The equation $C_0^* \exp(-x/b)$ in (Figure 4.31) corresponds to Eq. (4.14) with one fitted parameter (b), whereas the equation $a^* \exp(-x/b)$ corresponds to Eq. (4.13) with fitted parameters a and b . As expected, Eq. (4.13) gives a better fit on the measurements, since it has two degrees of freedom, whereas Eq. (4.14) has only one parameter to be estimated. Still, both equations provide a good fit on the measurement results.

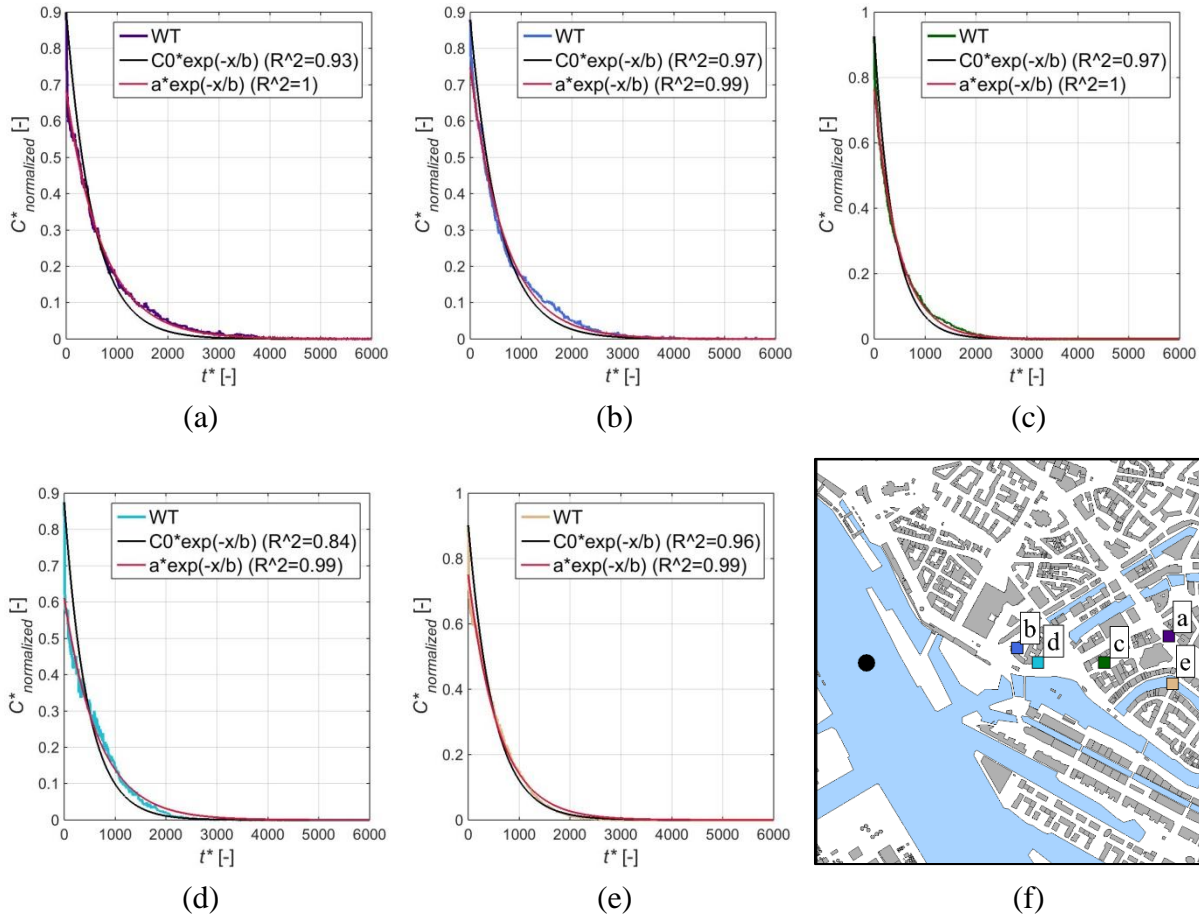


Figure 4.31 Eq. (4.13) and Eq. (4.14) fitted on exemplary measurement results of source S4 of the Hamburg data set (a-e). The source location is indicated with a black circle, the measurement points are marked with squares (f).

In Figure 4.32.a, the time constants are plotted against the distance from the source for multiple source locations. The time of the concentration decay generally increases with increasing distance from the source, similar to the retention times above flat-open terrain or homogeneous roughness. However, there are some deviations from this behavior (see Figure 4.34 for a more detailed analysis). It is also clear from Figure 4.32.a, that the time constants for the source located on the water surface (S4), surrounded by an open area are significantly shorter, than for the other sources located within the urban geometry. As expected, the measurement gas released from the source located on the river is washed out much faster compared to the other sources. When comparing the results of all source locations it is found, that the higher the building density and the height of the structures surrounding a source, the longer the retention times are.

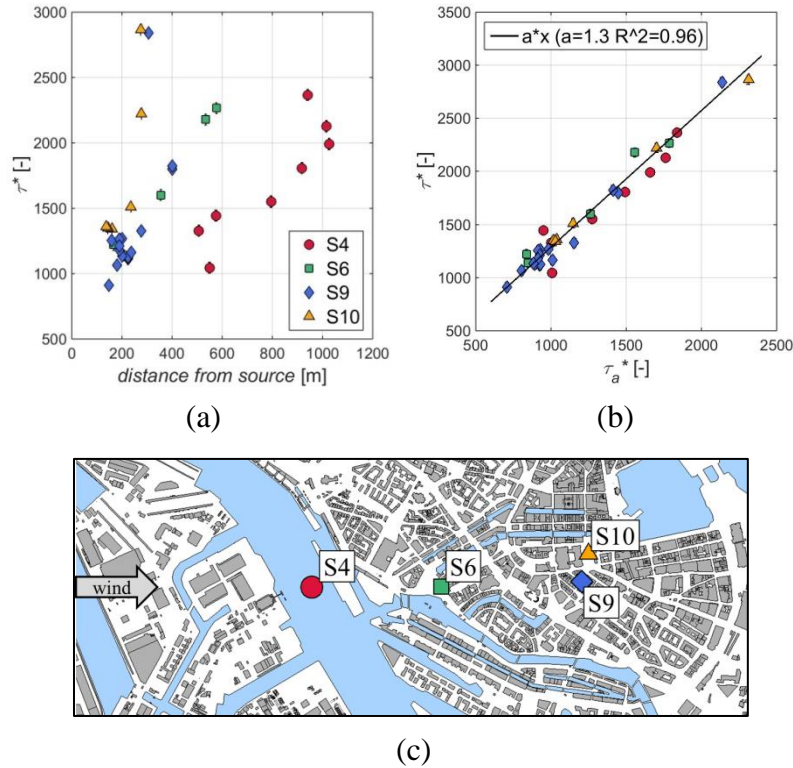


Figure 4.32 The relationship between the time constants (τ^* [-]) and the distance from the source (a) and the arrival time for short-term releases (b) measured for different source locations within the Hamburg model at pedestrian level. The locations of the sources within the Hamburg model (c).

Not only the residence time, also the transit time (or arrival time) is longer in a densely build area. Figure 4.32.b shows the relationship between the arrival time and the retention time for source locations within differently built areas. There is a strong correlation between the arrival time and the retention time. The arrival time for the short-term releases (unlike for puffs) was defined as the period after the start of the release until the concentration has reached C_0^*/e :

$$\tau_a^* = t^* \Big|_{C^*(t^*) = \frac{C_0^*}{e}} \quad (4.18)$$

Figure 4.33 shows a similar relationship for puff releases, as Figure 4.32.b for short-term releases. In Figure 4.33 the correlation between the leaving time and the arrival time of puff releases is investigated for one of the source locations. (For the definition of arrival time and leaving time for puff releases see Chapter 3.1.3.) Although the correlation between arrival time and leaving time for puff releases is not as strong as for short-term releases, it is still evident, that with increasing arrival time the leaving time increases. The strong correlation enables the prediction of the residence time from the arrival time of hazmat dispersion, which can be useful in emergency situations.

It is also interesting to see in Figure 4.32.b and Figure 4.33 that the relationship between arrival time and residence or leaving time is greater than one. The asymmetry of the arrival and

leaving times is a known phenomenon, discussed for example by Doran et al. (2007). They investigated puff measurements and found the ratio to be 3.1 for measurements in Oklahoma City. Two reasons are listed in this reference as possible reasons of the asymmetry: the along-wind dispersion coefficient (σ_x) increases, while the puff travels over the measurement location and the buildings retain the measurement gas, elongating the puff. In the Hamburg model, the buildings are lower and the city is less structured than in the case of Doran et al. (2007), which could explain, why the time ratio is smaller in Hamburg than in Oklahoma City. In the Hamburg test case, the ratio is higher for puff releases, than for short-term releases. However, this might be due to the different definitions of the characteristics and does not necessarily have a physical reason.

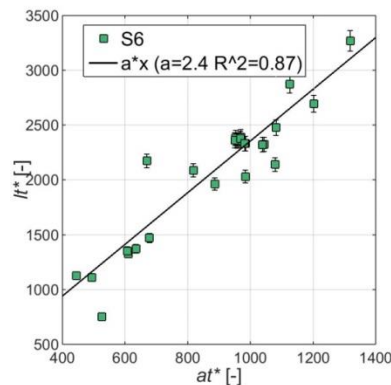


Figure 4.33 The relationship between the leaving time and the arrival time for puff releases measured at S6 source location within the Hamburg model at pedestrian level.

The uncertainty of the time constant values in Figure 4.32 was estimated based on repetitive measurements. The deviation of the results between different evaluation methods was not considered while defining the uncertainty of the time constants, since the evaluation process was carried out with the same technique for all measurements. When repetitive measurements were carried out, both results are shown in Figure 4.32. The overlap of results from the repeated measurements and the size of the scatter bars indicate that the uncertainty of measurement results was low ($\delta\tau^*=85$).

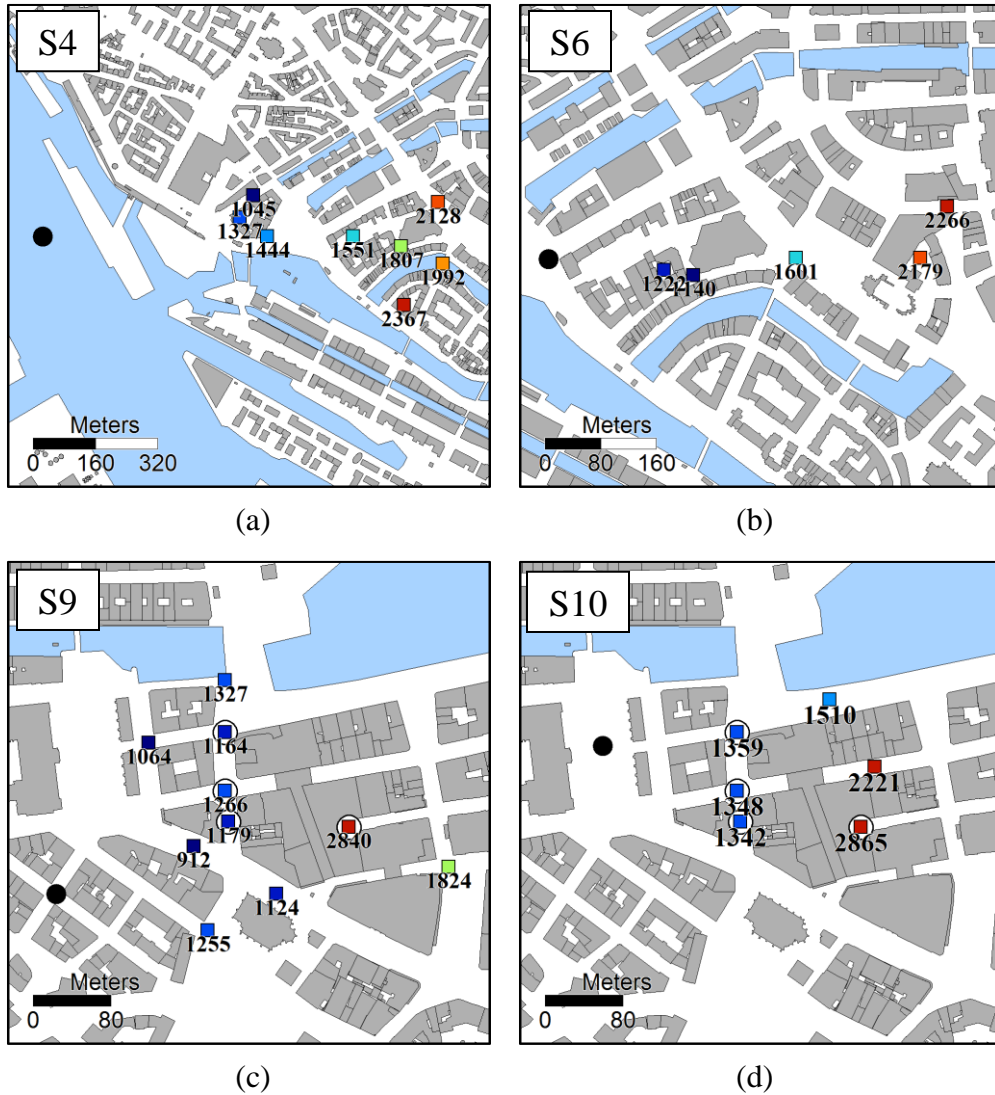


Figure 4.34 Time constants (τ^* [-]) measured for different source locations within the Hamburg model at pedestrian level. The source location is indicated with a black circle. The labels show the actual values of the time constant at each measurement location. The overlapping measurement locations are circled. The uncertainty of the time constants is $\delta\tau^*=85$.

Figure 4.34 demonstrates again that the farther away a measurement location is from the source, the longer the residence time will be. There are four locations that were measured for both S9 (Figure 4.34.c) and S10 (Figure 4.34.d) sources, marked with circles. At three of these measurement points the difference between the results of the two source locations are significantly above the repeatability. In all cases, the residence time is longer in case of S10 (Figure 4.34.d). This is somewhat surprising, considering that S10 is closer to these measurement locations, than S9. The reason for the longer residence times is possibly the effect of the city hall located upwind from S10. The city hall is the tallest building in this area and its horizontal dimensions are also substantially bigger in comparison to the other structures in the

neighborhood. It is safe to assume that S10 is in the separation bubble behind the city hall, causing the measurement gas to stay longer than the release from S9.

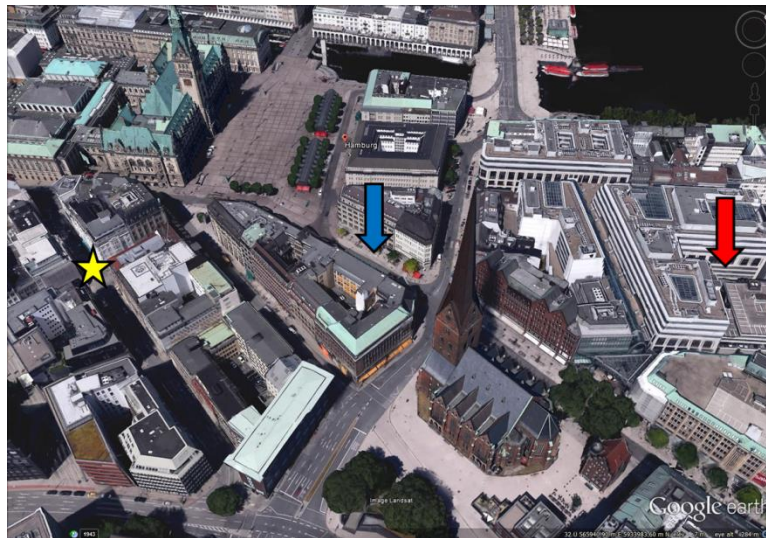


Figure 4.35 3D model of a part of Hamburg (source: Google Earth). The location of the S9 source (star) and the locations of the shortest (blue arrow) and longest (red arrow) measured residence times are indicated. The direction of the mean approach flow is from left to right.

Figure 4.35 is again a demonstration of the effect the city geometry has on the dispersion. It shows a 3D view of the buildings around source S9 where the locations of the shortest and longest residence times are indicated for this source. The shortest residence time occurs at a well-ventilated, wide street canyon, and the longest residence time was measured within a court-yard, which is surrounded in three directions by high buildings, causing low-wind conditions at the measurement location.

4.3 The effect of geometry modification on the dispersion

The structure of a city is never static; it changes constantly due to construction works. Buildings are torn down or modified and new ones are erected. The applicability of the results of urban dispersion studies carried out prior to a construction resulting in geometrical modifications is therefore questionable and worth investigating.

As examples of urban transformation, few areas of the inner part of Hamburg that changed between 2008 and 2015 are plotted in Figure 4.36. At most locations, only a single building was modified. The HafenCity (a part of it is plotted on the last maps of Figure 4.36), is a 2.4 km² area in Hamburg that is currently one of the largest urban development and reconstruction projects in Europe with a massive modification in the urban structure (Wikipedia, 2016b).



Figure 4.36 Modified building structures within the center of Hamburg between 2008 and 2015 (source: Google Earth). The maps on the left side are from 2008 and the maps on the right were recorded in 2015.

There are numerous studies dealing with the effects of geometry modifications. Leitl et al. (2001) measured the flow and concentration field in various high-resolution and simplified geometries in the wind tunnel and concluded that geometrical simplification can have a significant effect on the results of local scale dispersion modelling. Heist et al. (2009) and Brixey et al. (2009) investigated the flow and dispersion within an idealized geometry with and without a tall tower, finding that the tall building enhanced the ventilation of the street canyons. Janssen (2013) investigated the changes in pedestrian wind comfort due to building reconstructions in an

area of Hamburg and concluded that the reconstruction had measurable effect in the vicinity of the building. Kipsch (2014) found that rebuilding a city quarter has a significant effect on city ventilation even in the far field (in the order of a km). Balczó and Tomor (2016) investigated the wind comfort and dispersion characteristics of an urban square with and without vegetation and found that trees cause a decrease in wind velocity and turbulence.

There are also numerous studies on the effects of geometry simplifications in the literature. Many CFD studies, where the mesh-independence is tested, study the effects of geometrical simplifications as well. For example, Rakai et al., (2013) tested the effects of different grid resolutions and grid types on the flow and dispersion statistics within the Michelstadt geometry.

Most studies examining the effects of geometrical modifications or simplifications concentrate on the flow field (investigating wind comfort and city ventilation) or urban air quality. The focus of the measurements presented in this thesis was to evaluate the differences between the concentration fields and dispersion behavior of various urban geometries, including temporal transport characteristics. As described in Chapter 3.2.5, the concentration fields of five different model configurations within the Hamburg test case were measured. Figure 3.20 to Figure 3.24 show the various geometries. As a reminder, Table 4.2 lists the test cases including the number of modified buildings. Based on the data set, not only the effect of the geometrical change, but the effect of simplifications applied on the geometry for numerical modeling is studied.

Table 4.4 List of the measured test cases and the number of modified buildings.

Test case	Modified buildings
High resolution	reference model
Phase 1	1 LoD1 building
Phase 2	3 LoD1 buildings
Phase 3	12 LoD1 buildings
Phase 0	1 building removed

To compare the results of the different test cases, three types of comparison plots will be used, applicable for all characteristics presented in Chapter 3.1.3. The reference values are the measurement results of the high-resolution geometry. The test cases of the simplified and modified geometries are compared to the reference values. The comparison plots are illustrated on the peak concentration results of puff releases from source S11 within the phase 1 geometry (Figure 4.37). The first method is to plot the measured mean peak concentration of the phase 1 case together with the measured mean peak concentration of the high-resolution case (Figure 4.38.a). Figure 4.38.b shows the absolute difference between the mean peak concentration of the high-resolution case and the phase 1 case:

$$\Delta(\chi_{Ph})_i = \chi_{HR} - (\chi_{Ph})_i, \quad (4.19)$$

where $(\chi_{Ph})_i$ is the characteristic of interest (in our example the mean peak concentration) measured during the i th phase. X_{HR} is the characteristic of interest measured in the high-resolution model.

The third plot (Figure 4.38.c) shows the results of the relative differences:

$$\Delta_r(\chi_{Ph})_i = \frac{2\Delta(\chi_{Ph})_i}{\chi_{HR} + (\chi_{Ph})_i}. \quad (4.20)$$

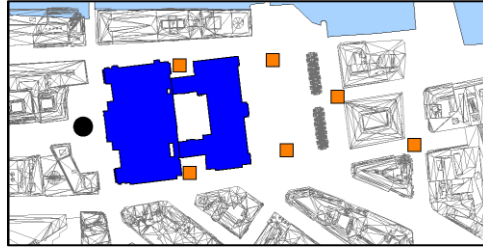


Figure 4.37 The locations of the puff measurements of source S11 for the high resolution and phase 1 (Ph1) model geometries. The source is indicated with a black circle and the squares mark the measurement locations. The Ph1 geometry corresponds to the test case, where only the city hall is simplified.

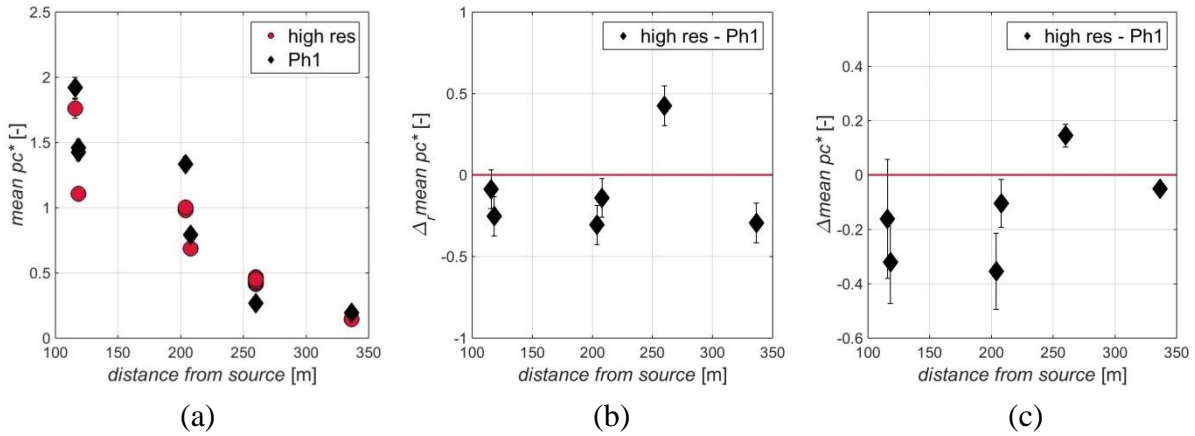


Figure 4.38 The measured mean peak concentrations (a); absolute (b) and relative (c) differences of the measured mean peak concentration results of the puff measurements of source S11 for phase 1.

Based on the plots of $\Delta(\chi_{Ph})_i$ and $\Delta_r(\chi_{Ph})_i$ a possible under- or overestimation of the results compared to the high-resolution test case can also be evaluated. If the points are above the red lines in Figure 4.38.b and c, the measurements carried out in the simplified model (phase 1) would underestimate the results of the high-resolution experiments.

4.3.1 Results of continuous release measurements

Due to the large amount of test cases collected, only exemplary results of the mean concentration for S9 and S11 will be presented to evaluate continuous release measurements. The

95th percentiles of the concentration distributions for S9 and S11, and all the results of the S6 and S10 measurements can be found in Appendix B.

Figure 4.39 shows the measurement locations for the sources of S9 and S11. In Figure 4.40 and Figure 4.41 the measured mean concentration and the absolute and relative differences are plotted for all phases.

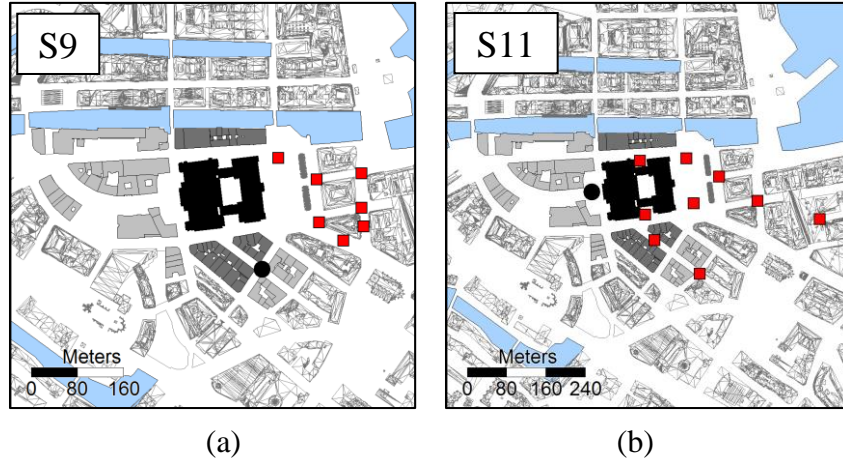


Figure 4.39 The measurement point locations for S9 (a) and S11 (b). The sources are marked with a back circle and the squares indicate the measurement locations. The phases of geometrical simplifications are indicated with different shades of grey.

As concluded in Chapter 4.1.1, the measured mean concentration and 95th percentile decreases with increasing distance, following approximately the power function (Eq. 4.3). For those sources, where the relationship between increasing distance and decreasing concentration is strong (e.g. S11), the absolute value of $\Delta(\chi_{Ph})_i$ also decreases with increasing distance in a similar manner (see Figure 4.41.a and b). However, the relative difference, $\Delta_r(\chi_{Ph})_i$, deviates from this behavior. For most cases, there is a weaker to no clear relationship between the distance from the source and the value of $\Delta_r(\chi_{Ph})_i$. The decreasing absolute differences of the measured concentrations suggest that the effect of geometry simplification on the prediction of the affected area is negligible.

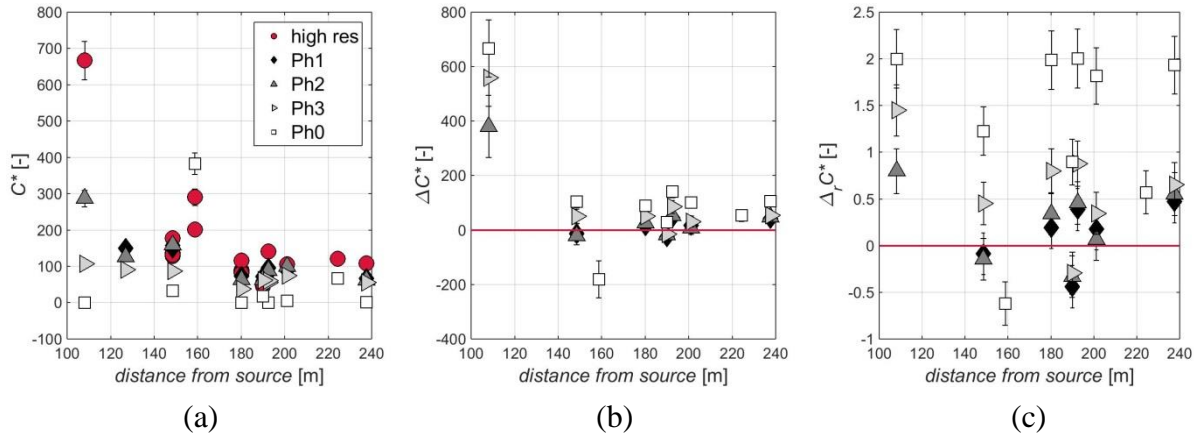


Figure 4.40 The measured mean concentrations (a) and the absolute (b) and relative (c) differences of continuous release measurement results for source S9 with different phases of geometrical simplifications.

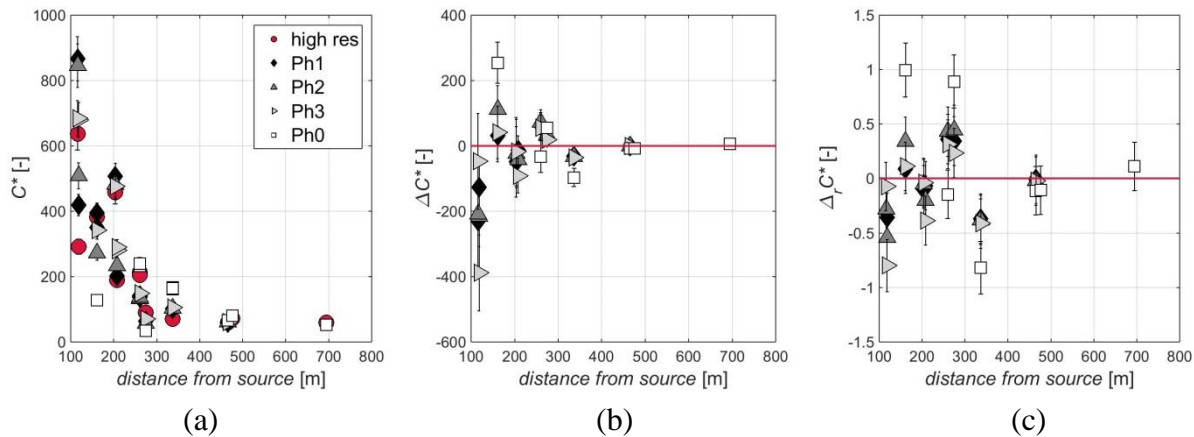


Figure 4.41 The measured mean concentrations (a); absolute (b) and relative (c) differences of continuous release measurement results for source S11 with different phases of geometrical simplifications.

As expected, the largest difference from every other test case is observed in phase 0. Phase 0 is the test case, when the city hall of Hamburg is removed entirely from the model geometry. The 112-m-high and 111-m-wide building covering a 7840 m² surface area (Wikipedia, 2016a) presents a significant influence on the flow and dispersion field. It is not surprising that removing such a prominent building would cause large differences. Changing the model of the city hall from high resolution to LoD1 geometry also causes a difference, which is in most cases significantly larger than the uncertainty of the results. The simplification of smaller buildings similar to their surroundings (phases 2 and 3) has only a small impact on the dispersion characteristics and the differences are mostly within the uncertainty intervals.

In cases of sources S9, S10 and S11 the source is located within the modified geometry itself. Source S6 is 680 m upwind from the city hall of Hamburg and 430 m upwind from the closest simplified building model in full scale. Figure 6.15 and Figure 6.16 in Appendix B show

that in case of source S6 the difference between the results of the various test cases is small, far less than the uncertainty of the measurements.

Based on the $\Delta(\chi_{Ph})_i$ and $\Delta_r(\chi_{Ph})_i$ plots the results of source S9 within the high-resolution model are underestimated by most of the measurements in the simplified models. The S10 measurements are on the other hand overestimated. The results measured for source S6 also show a slight overestimation, nevertheless the differences are below the uncertainty. The differences for source S11 are mainly within the uncertainty as well, and the results show no clear over- or underestimation.

Compared to the other source locations investigated, the results measured within the phase 0 geometry (without the city hall) during the release from source S9 show the largest deviation from the results captured in the high-resolution model geometry. This is surprising, since source S9 is not located in the direct vicinity of the city hall, unlike S10 and S11. Still, the geometry modification has a significant impact on the results.

Vertical concentration profiles

Two vertical profiles were measured for the source location S11 to investigate the effects of geometry modifications in dispersion behavior at different heights above ground (Figure 4.42). Source S11 is located upwind of the city hall of Hamburg. Both profiles show that if the city hall is removed entirely (phase 0 geometry), the measured concentration below average building height (around 34 m according to Hertwig, 2013) significantly increases. At higher elevations (especially for the results measured at the location of Figure 4.42.a) the concentration increases, if the city hall is present in the model. This is most likely due to the retention of tracer gas caused by the separation bubble behind the city hall.

It is surprising that the underestimation present in Figure 4.42.a is not consistent with the results of Figure 4.42.b. Lower concentration was measured within the simplified geometry, than in the high resolution test case at the location corresponding to Figure 4.42.a. Figure 4.42.b on the other hand shows an overestimation of the concentration measured within the high resolution by the simplified geometry below the average building height. Similar to the pedestrian-level measurements, the difference between phases 1, 2 and 3 are below the uncertainty intervals for the vertical profiles as well. This suggests that the modification or simplification of buildings similar to their surroundings does not affect the dispersion field significantly, even at locations close to the source as in the examples shown in Figure 4.42.

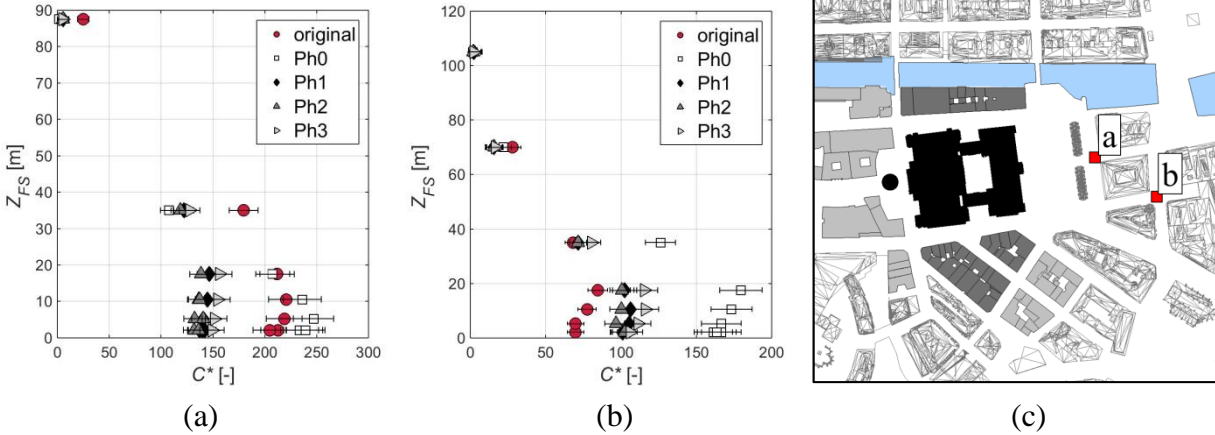


Figure 4.42 The measured mean concentrations (a and b) and the measurement locations (c) of the vertical profiles. The source is indicated by a black circle.

4.3.2 Results of puff release measurements

Geometry modifications and simplifications also influence the transient dispersion characteristics of the puff release measurements. To demonstrate these effects, exemplary results of the puff release measurements from source S11 in the Hamburg model are presented in this thesis. Further characteristics of the measurements corresponding to sources S11 and S10 can be found in Appendix C.

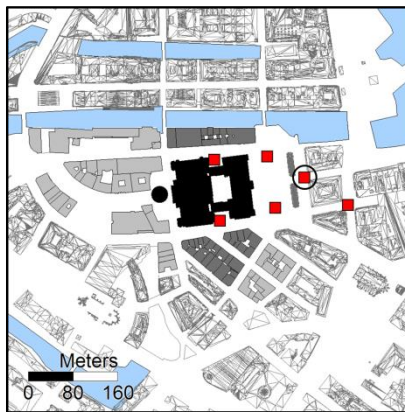


Figure 4.43 The puff measurement locations for source S11. The black circle indicates the source locations and the measurement points are marked with squares. The phases of geometrical simplifications are indicated with different shades of grey.

Figure 4.43 shows the measurement locations of puffs released corresponding to source S11. Due to the short distance between the measurement points and the source, it is expected to see significant differences in the results of the various geometries. Figure 4.44 and Figure 4.45 show the characteristics of the measured mean peak concentrations and the mean dosages respectively.

The effects on the characteristic times of the puff measurements are demonstrated by Figure 4.46 and Figure 4.47.

Similar to the results of the mean concentration measurements for continuous releases, the mean peak concentration and the mean dosage of the puffs decrease with increasing distance from the release location for each test case. The absolute values of the differences between the measured mean peak concentrations and dosages of the various phases show also a decreasing tendency with increasing distance. However, this tendency is not as pronounced as in case of continuous releases. This might be due to the small number of measurement locations for the puff releases.

At most locations, the measurements within the simplified geometries overestimate the mean peak concentration and dosage with respect to the results of the high-resolution model for both source locations. There is one measurement location (marked with a circle in Figure 4.43), where the measurements of phases 1 to 3 underestimate the results of the high-resolution model.

The tendencies of the peak concentration results of source S11 show similarity to the mean concentration of continuous releases. The values of both characteristics decrease with increasing distance. Also, changing the high-resolution model of the city hall to simplified geometry has a greater effect on the measurements, than changing multiple buildings less significant in size. However, when comparing Figure 6.12 in Appendix B and Figure 6.19 in Appendix C, the mean peak concentration measurements within the phase 0 geometry for source S10 show a significantly larger deviation from the high-resolution results, than the mean concentration of continuous releases.

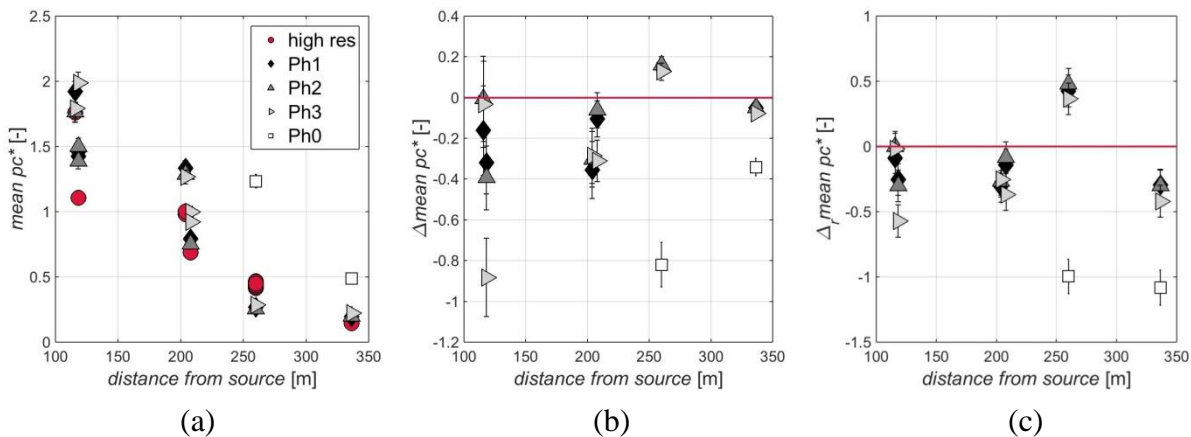


Figure 4.44 The measured mean peak concentrations (a) and the absolute (b) and relative (c) differences of puff release measurement results for source S11 with different phases of geometrical simplifications.

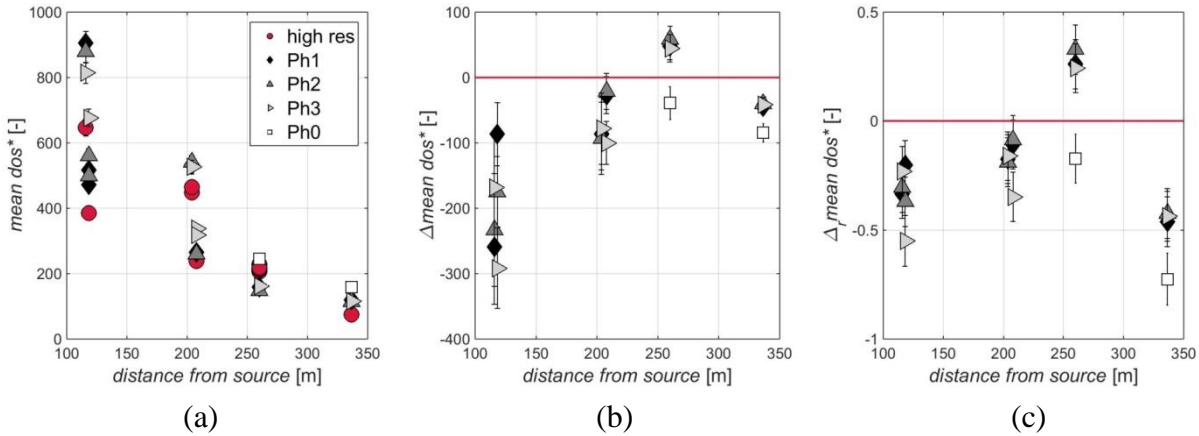


Figure 4.45 The measured mean dosages (a) and the absolute (b) and relative (c) differences of puff release measurement results for source S11 with different phases of geometrical simplifications.

According to the Gaussian puff model (see e.g. Stockie, 2011), the arrival time of a puff increases with increasing distance from the source. This can be observed on the characteristic times of puff releases within the Hamburg measurements (see e.g. Figure 4.46.a and the Figures in Appendix C). For each phase, the measured mean characteristic times increase with increasing distance from the source. On the other hand, the absolute and relative differences between the characteristic times of the simplified and high-resolution geometries show no clear relationship with the distance (Figure 4.46.b and c and Figure 4.47).

The mean peak time (the interval between the start of the release and the highest measured concentration) measured within the high-resolution geometry is underestimated by the measurements carried out within the simplified geometries. However, this behavior cannot be generalized for all characteristic times (see Figure 4.47). The arrival times are also underestimated in most cases within the simplified geometry. The leaving time of the puff measurements carried out within the high-resolution model are at some measurement points and phases underestimated, and overestimated at others. This also results in a mixture of under- and overestimation of the duration of the puffs, which is the difference of the leaving and arrival times.

In case of source S10, both the arrival times and leaving times are mostly underestimated (see Figure 6.22 and Figure 6.23 in Appendix C). The duration is on the other hand in all cases overestimated. The reason behind this is that the difference between the arrival times is larger than the difference between the leaving times, resulting in an overestimation of the durations.

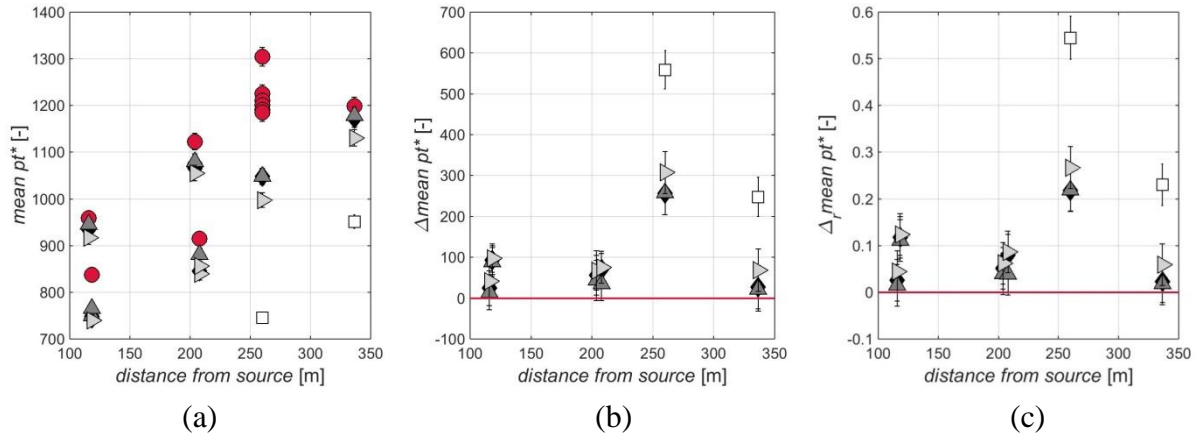


Figure 4.46 The measured mean peak time (a), its absolute (b) and relative (c) differences of puff release measurements for source S11 with different phases of geometrical simplifications.

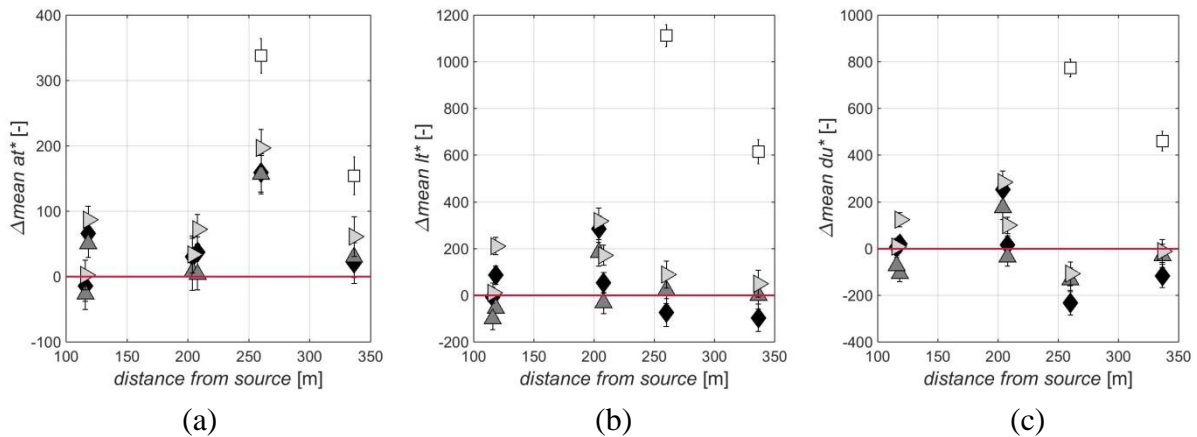


Figure 4.47 The absolute differences of measured mean arrival time (a), leaving time (b) and duration (c) of puff releases for source S11 with different phases of geometrical simplifications.

4.3.3 Impact of geometrical modification on the residence time

To evaluate the effect of geometrical simplification on the concentration decay, the time constants are plotted in Figure 4.48. Results are compared for the high-resolution model and the phase 3 geometry. Similar to the time characteristics of the puff release measurements, the time constant increases with increasing distance from the source in both model geometries.

Due to the limited number of measurements it is difficult to derive general conclusions from Figure 4.48. At half of the measurement locations the measured time constants of the different geometries are within the uncertainty intervals, hence not indicating a substantial impact of building geometry on retention time of pollutants. The time constants measured within the high-resolution geometry close to the source location are somewhat overestimated by the measurements within the simplified model. However, at the measurement locations farther from

the source this tendency seems to change and the phase 3 measurements rather underestimate the results of the high-resolution geometry.

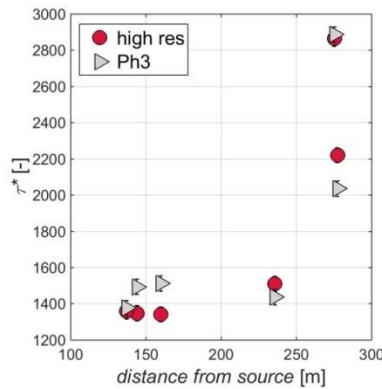


Figure 4.48 The measured time constants for the two test cases as function of the distance from the source.

It is interesting to compare the time constants of the concentration decay tests (Figure 4.49) with the leaving time measured for puff releases (Figure 4.50). Although the actual values are not directly comparable due to the different measurement and evaluation methods, the tendency of the change with geometrical simplification can be analyzed. Both the time constants and the leaving are greater in the simplified geometry. There is only one exception, the uppermost measurement location in Figure 4.49. The underestimation of time constants farther away from the source seen in Figure 4.48 is also visible from the leaving times of the puffs (Figure 4.50).

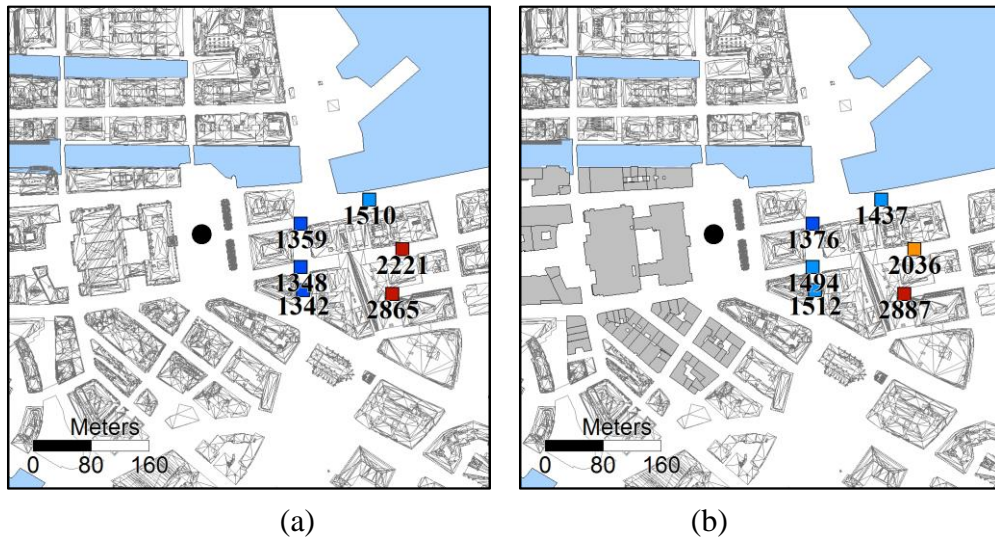


Figure 4.49 Time constants (τ^* [-]) measured for source S10 at pedestrian level within the high resolution (a) and the phase 3 geometries (b). The source is marked with a black circle and the squares correspond to the measurement locations. The labels show the actual values of the time constant at each measurement location. The uncertainty of the time constants is $\delta\tau^*=85$.

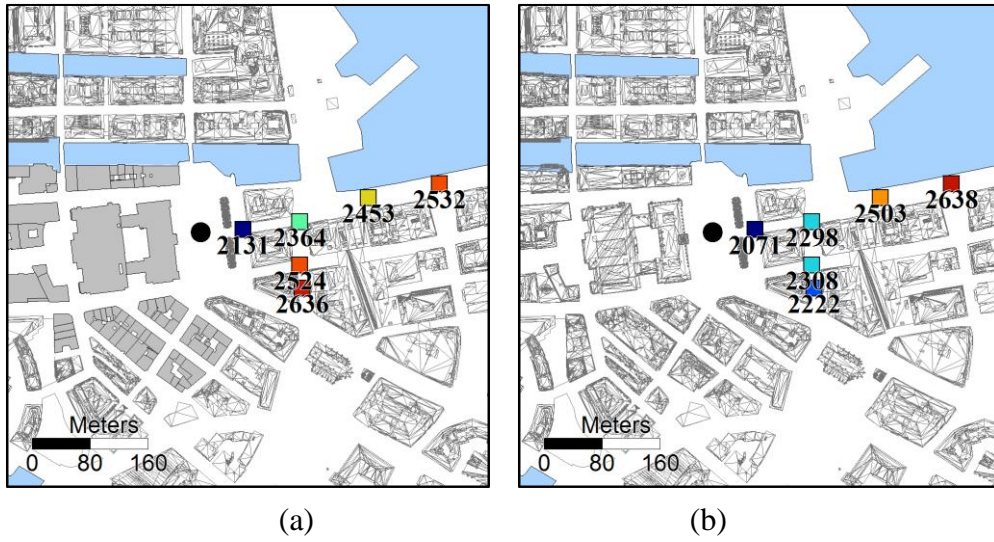


Figure 4.50 Leaving times of puffs measured for source S10 at pedestrian level within the high resolution (a) and the phase 3 geometries (b). The source is marked with a black circle and the squares correspond to the measurement locations. The labels show the actual values of the time constant at each measurement location. The uncertainty of the time constants is $\delta\tau^*=85$.

5 Conclusions

The aim of this thesis is to support the understanding and modeling of accidental and deliberate release transport in urban environments. Wind tunnel measurements of various models and scenarios were carried out and the measured data was statistically analyzed to investigate urban dispersion from point-source releases.

The measurement results presented in this thesis form some of the first, case specific high-quality data sets qualified for model validation purposes. The uniqueness of the data sets is that the measurements were specifically designed to focus on the needs of emergency response tools modeling airborne releases in urban environments. The feedback of model users and developers was incorporated during the process of the measurement planning, implementation and evaluation. The data sets were used in the frame of various projects to validate multiple numerical models already. Due to the high statistical representativeness of the measurements, the data is also suitable for analyzing the entire concentration distributions including higher statistics and extreme value predictions.

5.1 Summary of the results

Covering every aspect of accidental releases in urban environments is impossible in the frame of a PhD thesis. Therefore, five major research questions were proposed in the Introduction (Chapter 1.2) incorporating the focus of this thesis:

- How does the release duration affect transient dispersion behavior?
- How appropriate is it to model the spatial distribution of the mean concentration with the Gaussian distribution function?
- How to predict high concentrations?
- What is the effect of geometrical modification on the dispersion?
- How representative are the predictions based on a simplified geometry?

In the following chapter, I will summarize the results focusing on these five questions.

5.1.1 Characterizing the dispersion results of various release scenarios

A comprehensive set of evaluation methods was presented to describe concentration data. Characteristics applicable for continuous, short-term and puff releases are presented and their dimensional forms are derived. This summary can be helpful in the future to evaluate concentration results from measurements or simulations.

A consistent set of puff parameters based on the dosage was applied to evaluate the puff measurements. Dimensional analysis of the parameters was carried out in this thesis to derive the puff parameters from the fundamental physical dimensions. The dimensionless numbers were verified based on existing and new data sets including various systematic investigations. The results are particularly important for the evaluation of future systematic puff measurements and simulations, because the consistent set of parameters with verified nondimensional formulae provide a thorough characterization of transient puff signals.

Based on the results of the measurements with various release durations, it was shown that the nondimensionalization of short-term releases depends on the ratio of the release duration and the arrival time. According to the results presented in this thesis, the exponential decay function fits well on the measured time series of the decreasing concentration. It was presented, that the time constant of the exponential decay function can be applied to characterize the residence time. Various methods were tested to evaluate the results of short-term release measurements to optimize the process. The final method is capable to evaluate the residence time based on an ensemble of measured time series.

The results show that with increasing distance from the source and increasing building density around the source, the residence time of pollutants increases. The results are consistent with previous findings from the literature, that with increasing building density around the source, the arrival (or transport) time and residence time of pollutants increase. Strong relationships were documented between the travel times and the residence times of short-term releases and between the arrival time and leaving time of puff releases. This suggests, that in emergency situations, if information about the travel time is available, it can be used to predict the time after the end of the release, when the concentration decreases below the threshold value.

5.1.2 The (in)appropriateness of the Gaussian distribution to model the concentration field in urban areas

It was shown in this thesis, that even though some of its assumptions do not hold in urban environments, simplified equations derived from the Gaussian plume model provided reasonable fits on the investigated data sets. One major characteristic that the Gaussian model was not able to capture is the misalignment of the source location and the maximum of the lateral concentration profiles.

The results demonstrate that although the concentration profiles can be modeled with Gaussian distributions, the Gaussian plume model is not capable to capture the complexity of the dispersion field within an urban environment. The fact that the Gaussian distribution provided a reasonable fit for the measured profiles suggest that if the flow field is predicted properly, hybrid models should provide good estimations of the concentration field within city geometries. Here, hybrid model refers to the technique, where the flow field is simulated by a complex model, and a simpler method, such as the Gaussian plume model or Lagrangian model is used to predict the concentration field. This technique also has the benefit regarding emergency situations, that the flow field can be generated beforehand, applying only a simpler and faster dispersion model on site.

Another aspect of the results is that the fits in all directions are generally better above the buildings, than within the geometry. It is not surprising, since the higher above the buildings the measurements are, the more homogeneous the turbulence is going to be, and the closer we get to fulfil the assumptions of the Gaussian plume model. This is an important message for validation exercises. If a model will be applied to predict the concentration field at pedestrian level, the validation should focus on the predictions at this height, because providing good results well above the buildings does not necessarily imply that the model can predict the concentration field within the geometry.

5.1.3 Predicting high concentrations using probability density functions

General probability density functions were fitted on the measured concentration distributions using two techniques. The PDFs were fitted on the whole measured concentration distributions and on the first two moments of the distributions. To evaluate the appropriateness of the PDFs, the predictions of the 95th percentiles of the concentration distributions were assessed using validation metrics. The results showed, that the gamma distribution provided the most accurate predictions of the higher order statistics. Nonetheless, the other tested PDFs (normal, clipped normal, lognormal and exponential) gave reasonable predictions as well. This can be explained by the strong relationship found between the mean and the 95th percentile values of the concentration distributions.

Most numerical models, such as the Gaussian plume or the RANS model provide the mean concentration field only. Even models with higher complexity, such as LES, a statistically representative concentration distribution at a single location can only be obtained after significant, often not affordable, simulation time. The results of this thesis show, that if the mean value can be predicted by a numerical model, it is possible to estimate the higher order statistics with negligible additional uncertainty compared to the usual uncertainty of numerical models.

In emergency situations, information about the highest concentration that potentially can occur at a location is important. However, the highest possible concentration is most likely not

captured during a finite measurement or numerical modeling. Nonetheless, the finite source concentration suggests that the concentration distribution should have a finite upper limit as well.

Through extreme value analysis of the results it was demonstrated that neither the generalized extreme value distribution, nor the generalized Pareto distribution provides a sufficient method to predict the theoretical extrema of the measured concentration distributions. The GEV and GPD functions have finite extremums only, if their shape parameters are negative. However, most shape parameters of the fitted distributions on the measured concentration data fall above zero. Those that are negative are still so close to zero, that their 95% confidence intervals extend into the positive domain. This result shows that based on the statistically representative distributions of the data sets, predicting a finite extremum is not possible with sufficient confidence.

5.1.4 The impact of geometry modifications and simplifications on the dispersion in urban environments

Systematic measurements enabled the investigation of the effects of geometry modifications and simplifications on the concentration field in urban environments. Continuous, short-term and puff releases were measured for four different source locations and five different phases of geometry modifications. The high-resolution case was measured within the original model and was considered as the reference for the other test cases. In the simplified models, the number of the modified buildings was systematically increased. In one extreme case, a significant building was completely removed from the high-resolution geometry.

The results show that the absolute differences between the concentrations measured within the high-resolution geometry and simplified models decrease with increasing distance from the source. This suggests that the prediction of the area affected by the released material based on the results obtained from a simplified geometry is reliable. On the other hand, the relative differences of the concentration results show no significant dependence on the distance.

Generally, the characteristics describing the concentration are overestimated in the simplified geometries, while the characteristic times are overestimated. This tendency however is not true for all source locations or characteristics. Still, in most cases due to flat roofs of the simplified geometries resulting in lower heights, the gas is transported faster and with less mixing. This results in lower characteristic times and higher concentration levels at most measurement locations. The under- and overestimations do not show a linear tendency, therefore it is not possible to define a universal scaling factor to compensate for this effect. Also, unlike the concentration results, the relative and absolute differences of the characteristic times show no correlation with the distance. This suggests that the underestimation of the characteristic times in simplified geometries does not decrease significantly with the distance.

Although the differences between the high-resolution and simplified geometries are detectable, it was shown that they are still quite low compared to the total uncertainty of most numerical models. As expected, the largest differences occurred at an extreme case, where the city hall of Hamburg, a significant building compared to its surroundings was removed from the model completely. The deviation between the high-resolution and the simplified models were also often larger than the measurement uncertainty. However, looking only at the differences between the simplified building geometry cases, these fall below the measurement uncertainty at most locations. It is therefore safe to conclude that if a building significantly different in size from its surroundings is changed, the effect on the model results should be investigated. However, if a building is rebuilt without significant geometrical changes or it is similar in size to its surroundings, the effects will most likely be within the uncertainty of the predictions. The results also showed, that if a source is in the direct vicinity of a geometrical change not yet included in the model, results should be handled with extra caution.

5.2 Outlook

Several aspects of accidental releases in urban environments were not discussed in details within this thesis. The effects of gas properties (such as the density, temperature or chemical reactivity), source dimensions, thermal processes, traffic-induced turbulence and vegetation are just some examples of topics relevant for urban dispersion that are not possible to investigate based on the Michelstadt and Hamburg data sets. Still, the measurement results provide much potential to examine urban dispersion beyond the focus of this thesis. As an example, the systematic evaluation of the distance-dependency and correlations between puff parameters can be investigated (similar to the correlation between the arrival and leaving times discussed in Chapter 4.2.2). In this regard, Lübcke (2014) studied the puff parameters measured within the Michelstadt geometry, whereas Hellweg (2015) investigated the puff measurements of the Hamburg data set. Velocity measurements were carried out for both test cases in previous campaigns, which were not particularly evaluated in this thesis. This opens a series of possibilities to investigate not only the flow field, but its correlation with the concentration field as well. Another example of the application of the results is to validate emergency response tools, which was presented in Chapter 3.2.6.

Even topics discussed in this thesis could be further investigated based on the comprehensive data sets now available. Various methods exist to estimate the parameters of the Gaussian plume model (see e.g. Hanna et al., 1982, for further details). These methods could be evaluated and further developed based on the measurement results to provide suggestions on the parameter prediction for the Gaussian plume model. The block size for the generalized extreme value distribution and the threshold for the generalized Pareto distribution should be analyzed and optimized for each measurement individually. The distribution functions could also be applied to

investigate the predictability of the distributions and extrema of puff parameters. Further aspects of the effects of geometry simplification could also be evaluated and quantified based on the measurement results.

As the examples above show, there is a lot of potential to extend the research of accidental releases in urban environments based on the Michelstadt and Hamburg data sets, or carry out new measurements. However, the results in this thesis showed that numerical and physical modeling are based on simplifications and assumptions, therefore the results should not be taken as real values and can only be interpreted considering the uncertainty inherently present in any model result. Still, numerical modeling is the most effective way to provide quick and reliable predictions during an accidental release, and the quality of the results keep improving due to the fast development of research and technology. Although most numerical models currently used in emergency situations are based on a simplified geometry, only predict a single value (or the first two moments of the concentration distribution) and use assumptions that do not necessarily hold in urban environments, with careful adjustments and considerations based on the results of this thesis, the predictions can be improved.

6 Appendix

6.1 Appendix A: Longitudinal, lateral and vertical concentration profiles

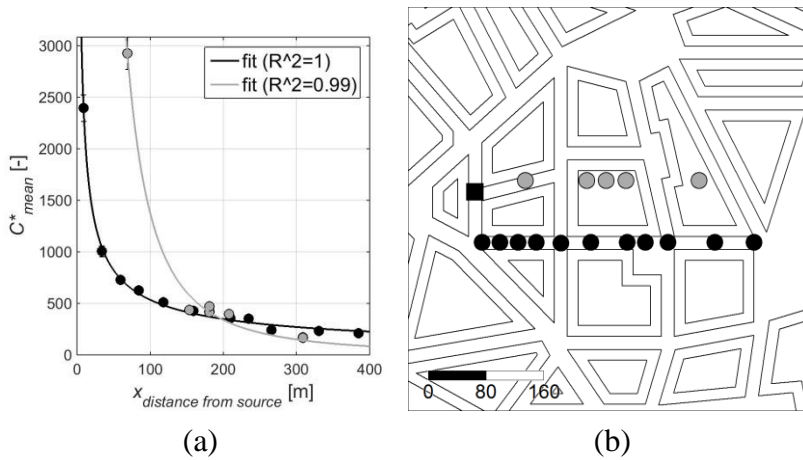


Figure 6.1 Longitudinal mean concentration profiles measured at half-building height in the Michelstadt model. The fits of the simplified Gaussian distribution in x direction are indicated with lines. The locations of the source (square) and measurements (circles) within the model (b).

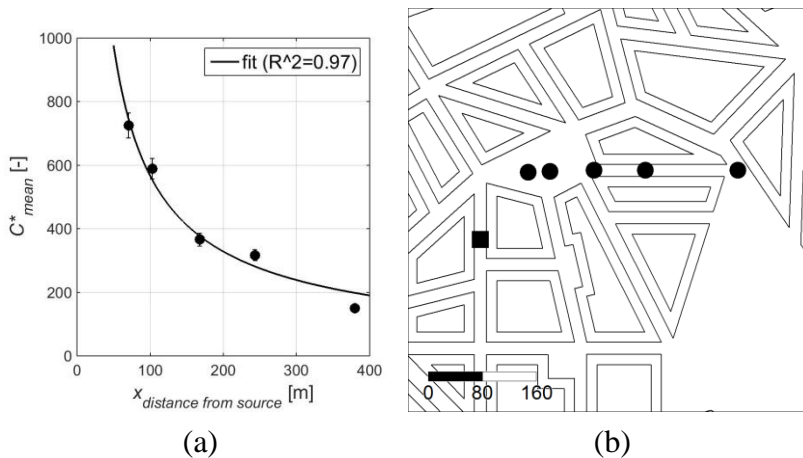


Figure 6.2 Longitudinal mean concentration profile measured at half-building height in the Michelstadt model. The fit of the simplified Gaussian distribution in x direction is indicated with a black line. The locations of the source (square) and measurements (circles) within the model (b).

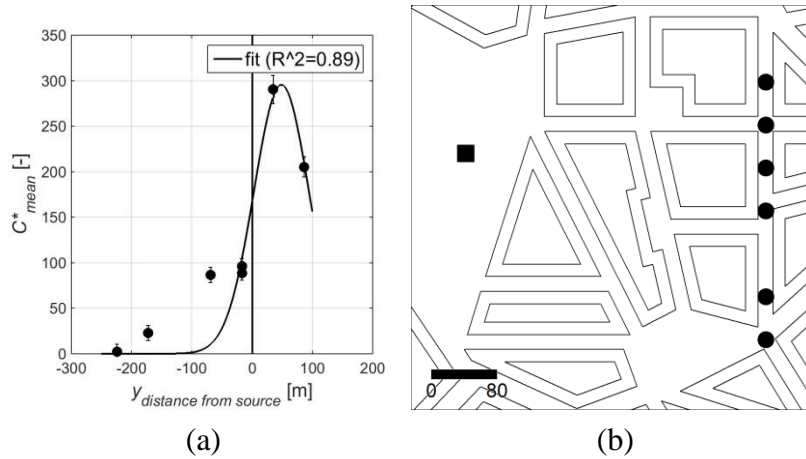


Figure 6.3 Lateral mean concentration profiles measured at half-building height in the Michelstadt model. The fit of the simplified Gaussian distribution in y direction is indicated with a black line. The locations of the source (square) and measurements (circles) within the model (b).

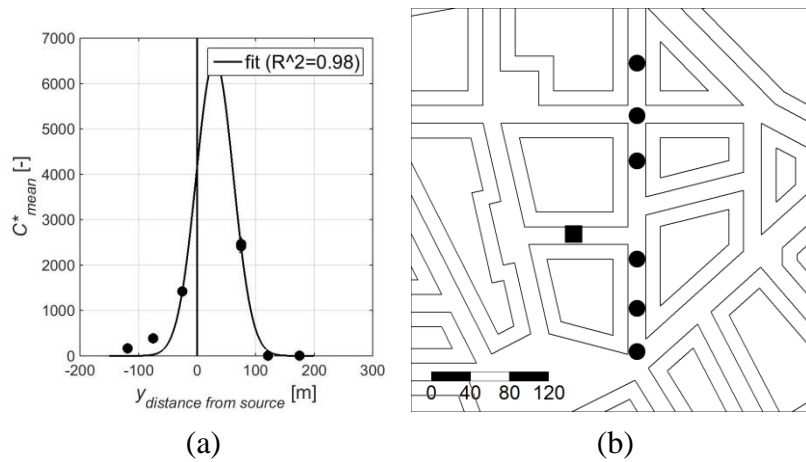


Figure 6.4 Lateral mean concentration profiles measured at half-building height in the Michelstadt model. The fit of the simplified Gaussian distribution in y direction is indicated with a black line. The locations of the source (square) and measurements (circles) within the model (b).

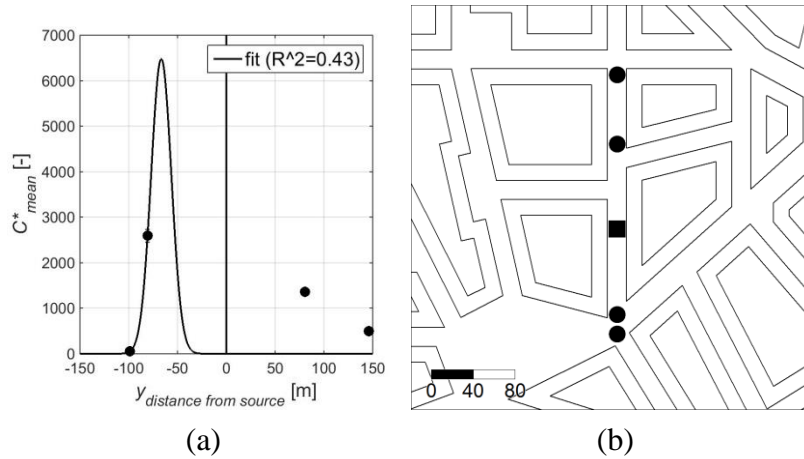


Figure 6.5 Lateral mean concentration profiles measured at half-building height in the Michelstadt model. The fit of the simplified Gaussian distribution in y direction is indicated with a black line. The locations of the source (square) and measurements (circles) within the model (b).

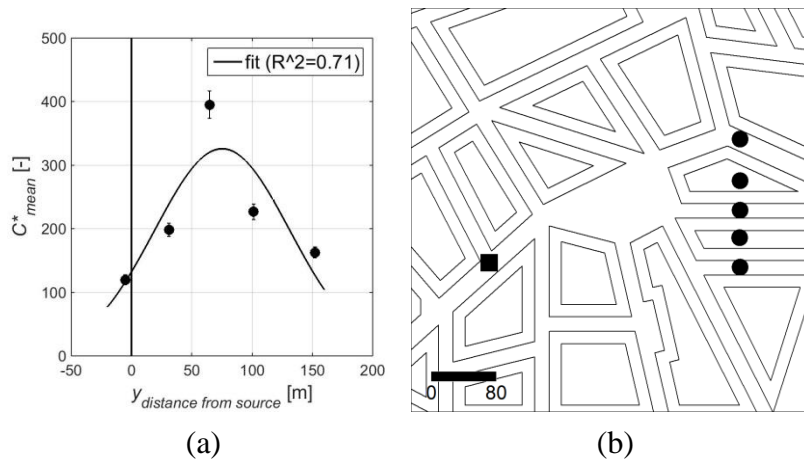
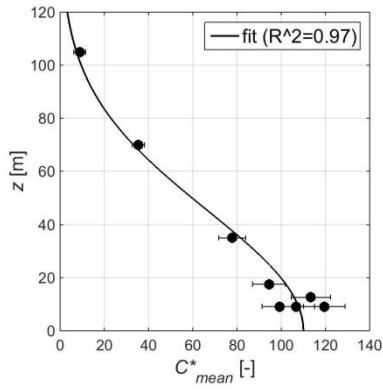
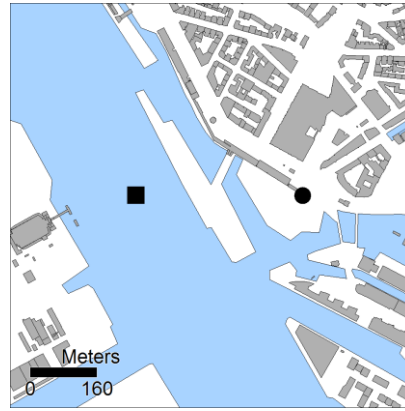


Figure 6.6 Lateral mean concentration profiles measured at half-building height in the Michelstadt model. The fit of the simplified Gaussian distribution in y direction is indicated with a black line. The locations of the source (square) and measurements (circles) within the model (b).

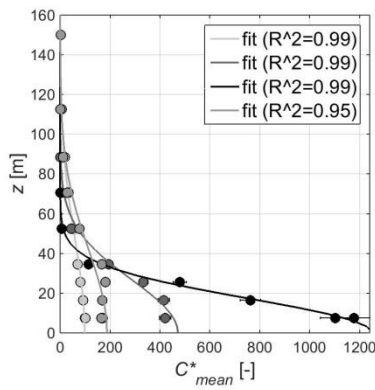


(a)

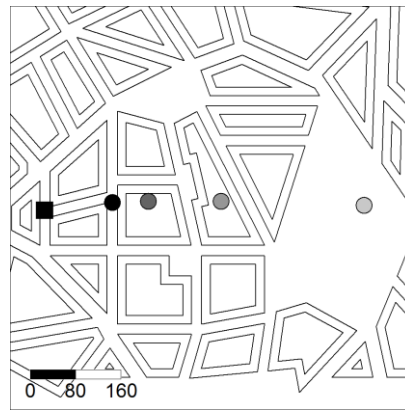


(b)

Figure 6.7 Vertical mean concentration profile measured within the Hamburg model. The fit of the simplified Gaussian distribution in y direction is indicated with a black line. The locations of the source (square) and measurements (circles) within the model (b).



(a)



(b)

Figure 6.8 Vertical mean concentration profiles measured within the Michelstadt model. The fits of the simplified Gaussian distribution in z direction are indicated with lines. The locations of the source (square) and measurements (circles) within the model (b).

6.2 Appendix B: Effects of geometry modifications on continuous release measurement results

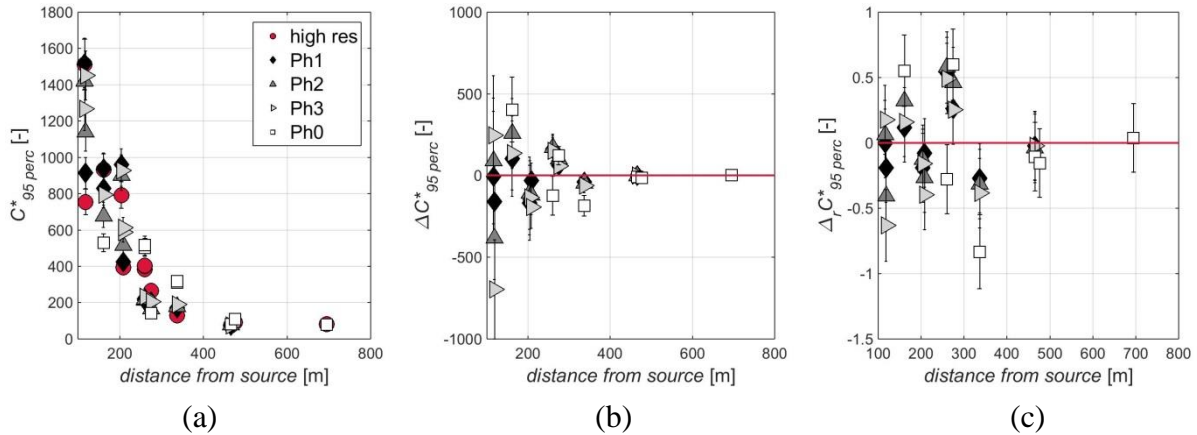


Figure 6.9 The measured 95th percentile of the concentration distributions (a) and their absolute (b) and relative (c) differences of continuous release measurement results for source S11 with different phases of geometrical simplifications.

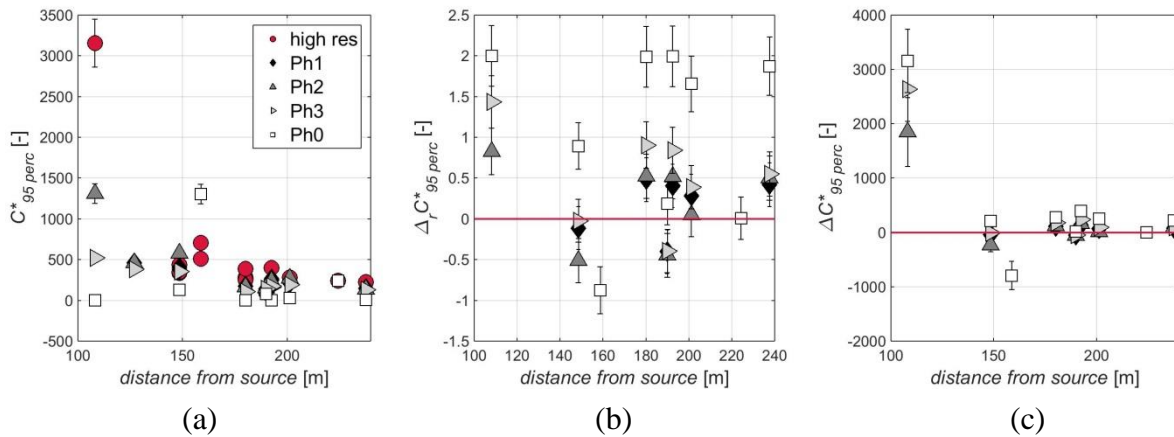


Figure 6.10 The measured 95th percentile of the concentration distributions (a) and their absolute (b) and relative (c) differences of continuous release measurement results for source S9 with different phases of geometrical simplifications.

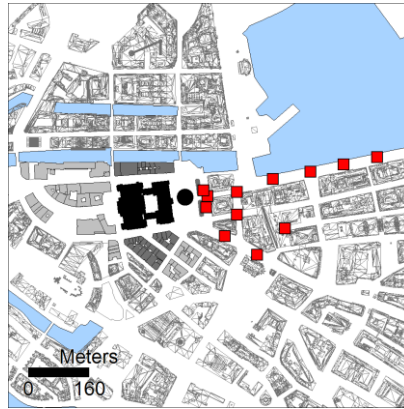


Figure 6.11 The measurement locations (squares) for source S10 (circle). The phases of geometrical simplifications are indicated with different shades of grey.

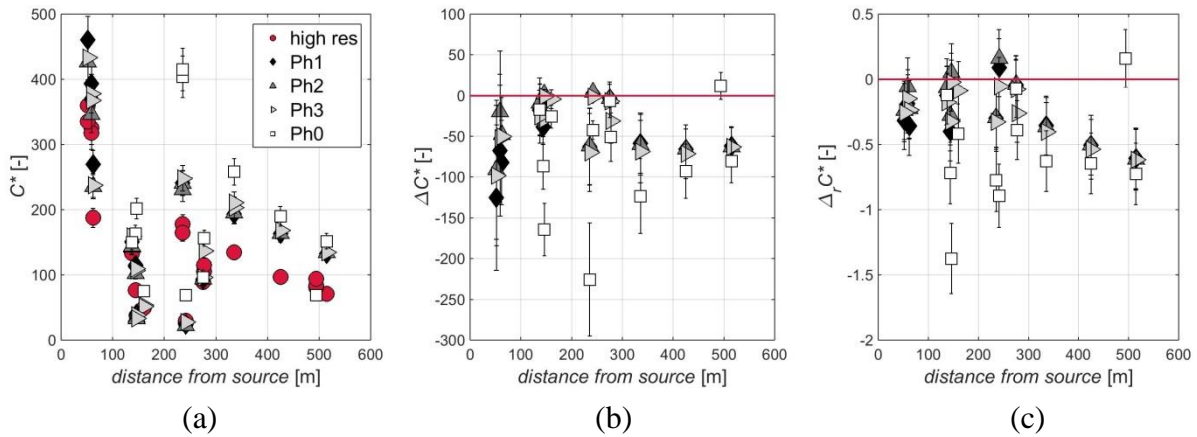


Figure 6.12 The measured mean concentrations (a) and their absolute (b) and relative (c) differences of continuous release measurement results for source S10 with different phases of geometrical simplifications.

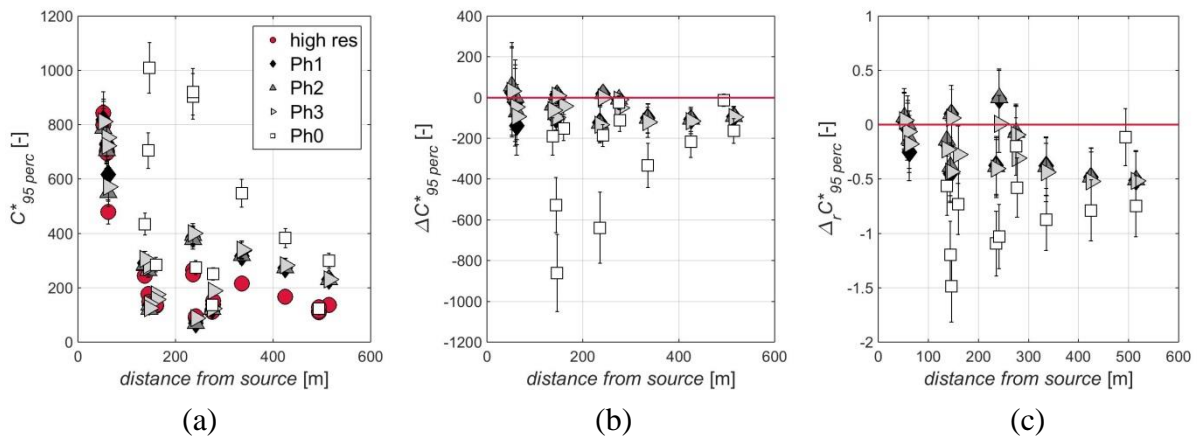


Figure 6.13 The measured 95th percentile of the concentration distributions (a) and their absolute (b) and relative (c) differences of continuous release measurement results for source S10 with different phases of geometrical simplifications.

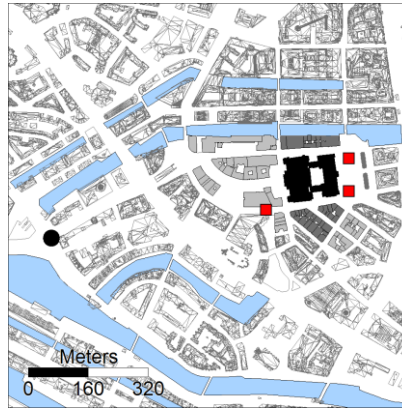


Figure 6.14 The measurement locations (squares) for source S6 (circle). The phases of geometrical simplifications are indicated with different shades of grey.

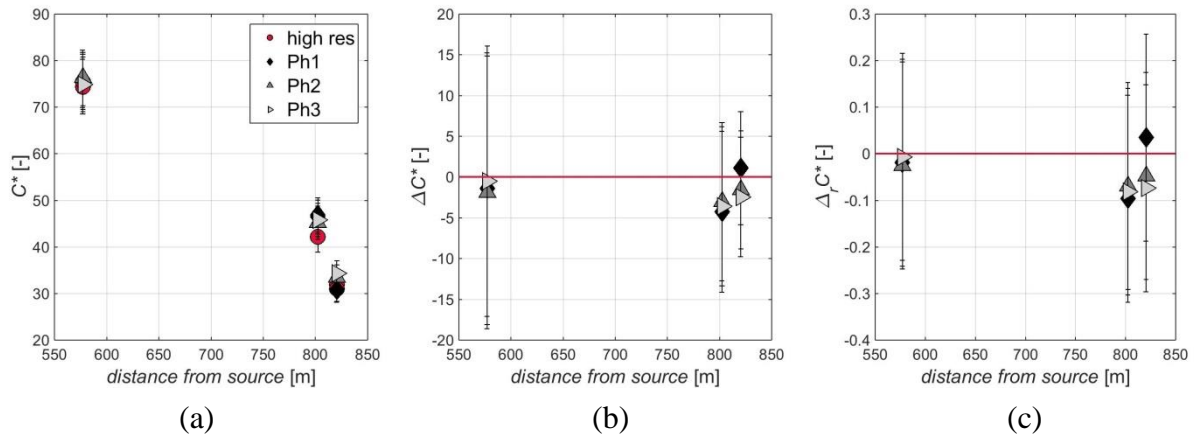


Figure 6.15 The measured mean concentrations (a) and their absolute (b) and relative (c) differences of continuous release measurement results for source S6 with different phases of geometrical simplifications.

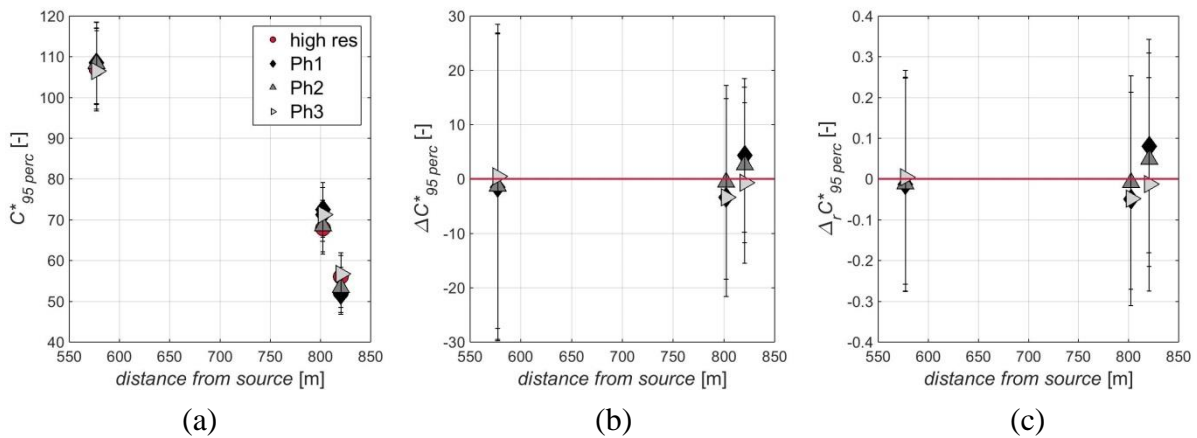


Figure 6.16 The measured 95th percentile of the concentration distributions (a) and their absolute (b) and relative (c) differences of continuous release measurement results for source S6 with different phases of geometrical simplifications.

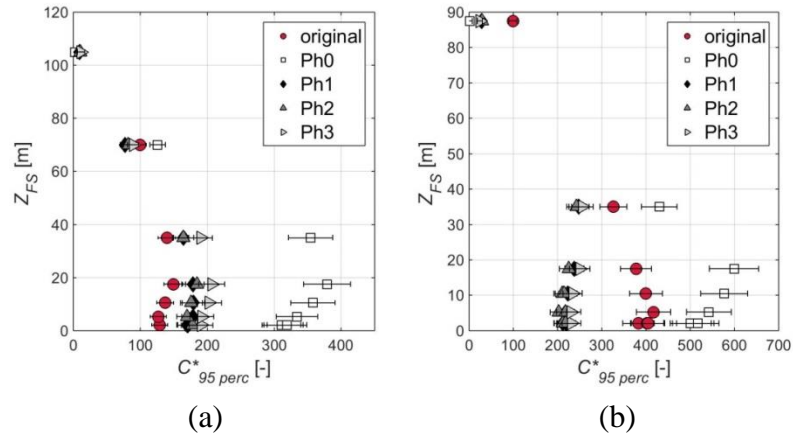


Figure 6.17 The measured vertical profiles of the 95th percentile of the concentration distributions (a) and their absolute (b) and relative (c) differences of continuous release measurement results with different phases of geometrical simplifications.

6.3 Appendix C: Effects of geometry modifications on puff release measurement results

Legends are not plotted on the subsequent figures to enable better representation. The legends presented in the figures of Appendix B are applicable to the figures in this appendix.

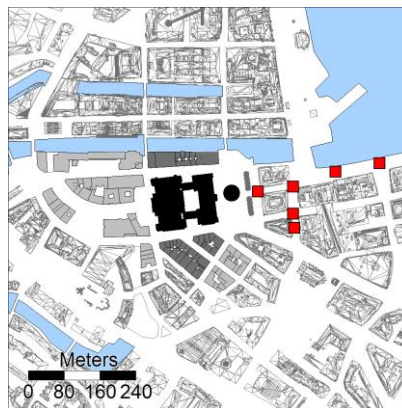


Figure 6.18 The puff measurement locations (squares) for source S10 (circle). The phases of geometrical simplifications are indicated with different shades of grey.

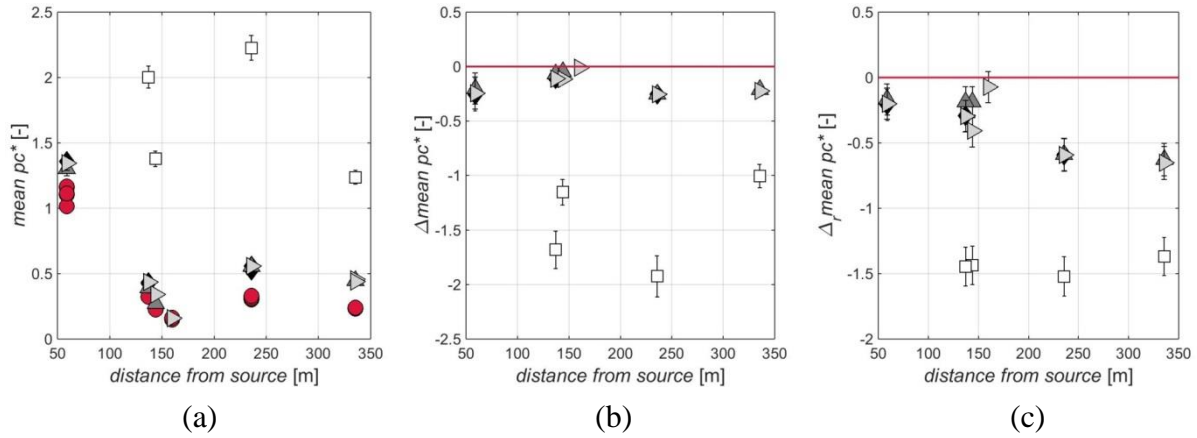


Figure 6.19 The measured mean peak concentrations (a) and the absolute (b) and relative (c) differences of puff release measurement results for source S10 with different phases of geometrical simplifications.

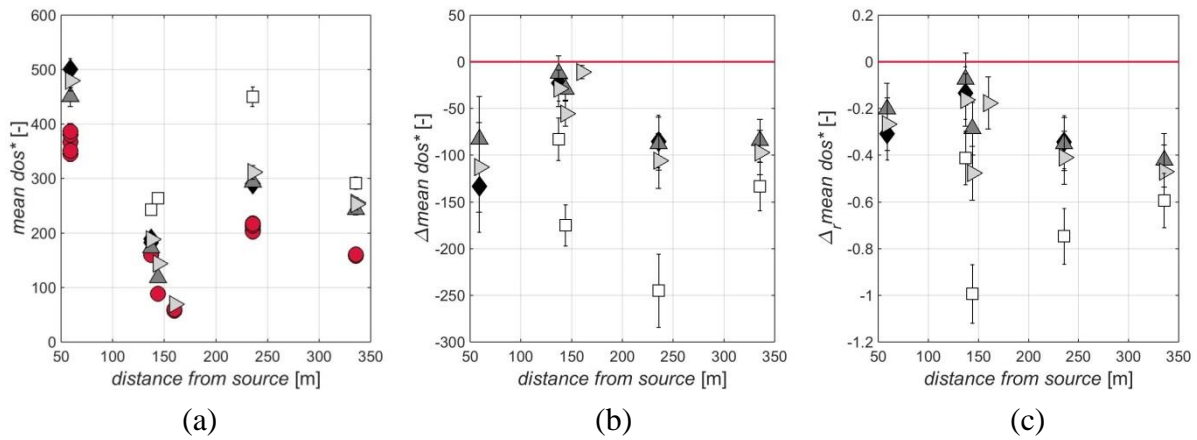


Figure 6.20 The measured mean dosages (a) and the absolute (b) and relative (c) differences of puff release measurement results for source S10 with different phases of geometrical simplifications.

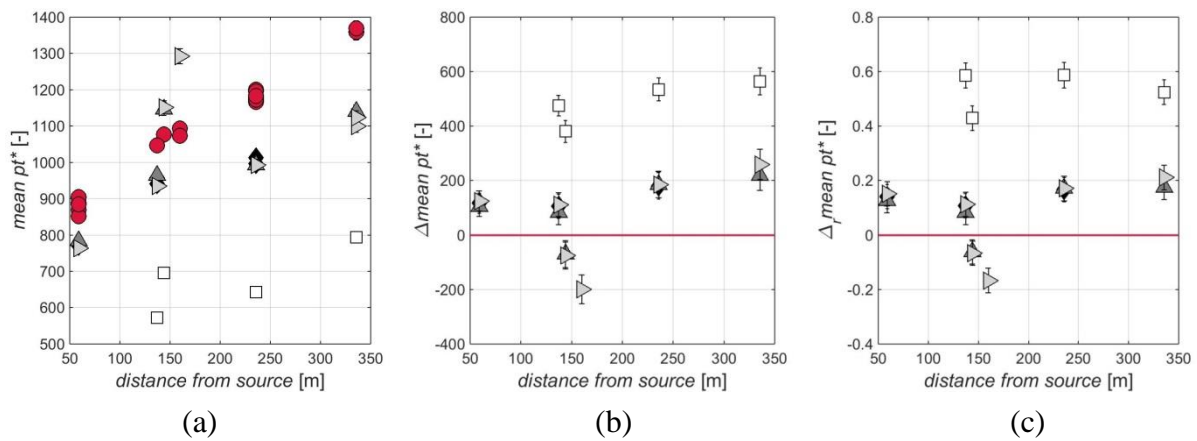


Figure 6.21 The measured mean peak times (a) and the absolute (b) and relative (c) differences of puff release measurement results for source S10 with different phases of geometrical simplifications.

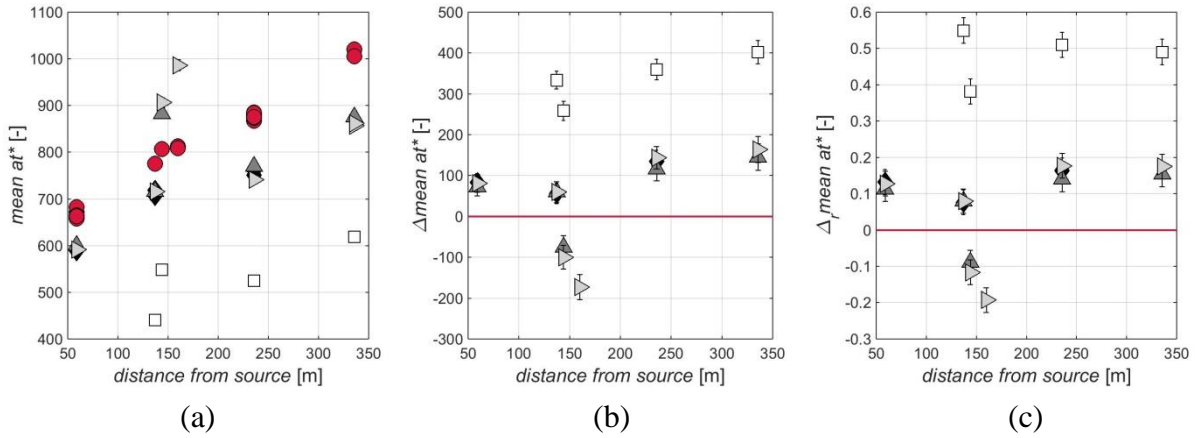


Figure 6.22 The measured mean arrival times (a) and the absolute (b) and relative (c) differences of puff release measurement results for source S10 with different phases of geometrical simplifications.

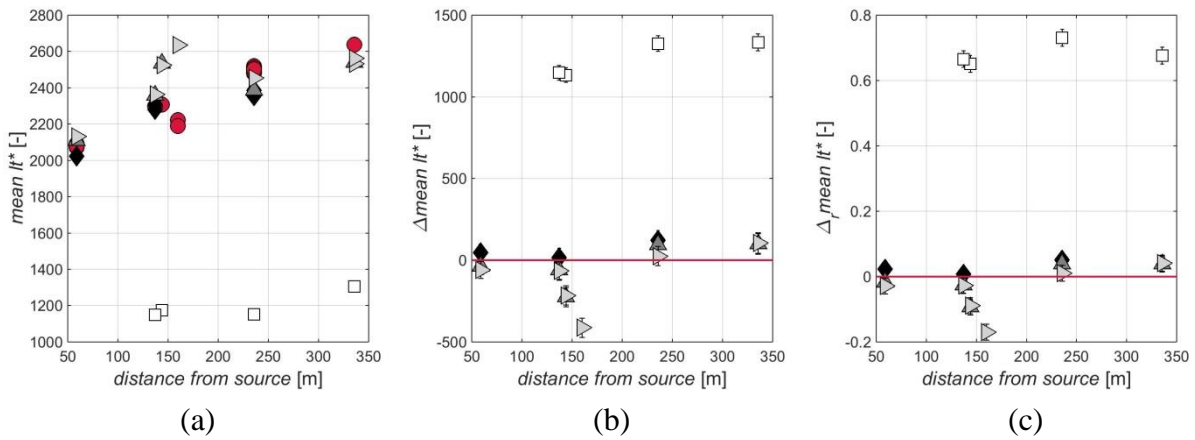


Figure 6.23 The measured mean leaving times (a) and the absolute (b) and relative (c) differences of puff release measurement results for source S10 with different phases of geometrical simplifications.

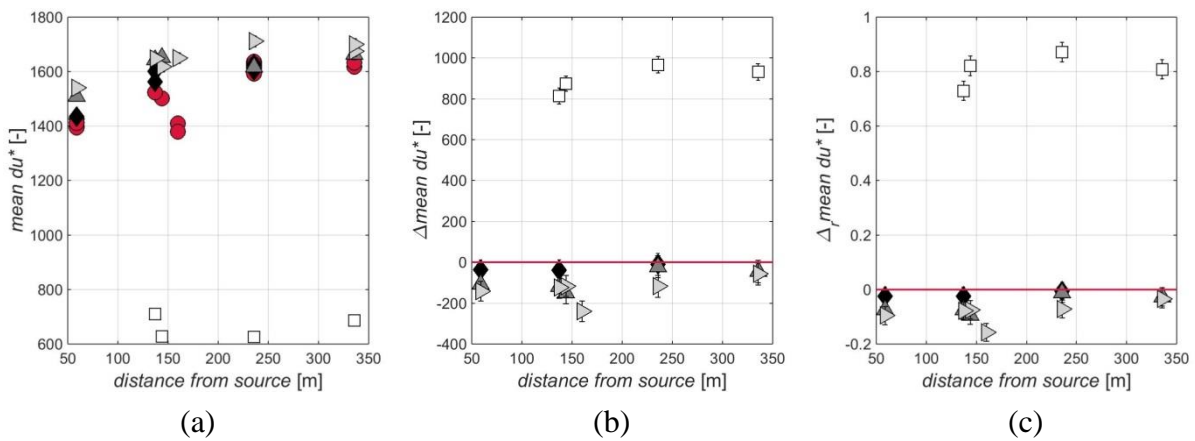


Figure 6.24 The measured mean durations (a) and the absolute (b) and relative (c) differences of puff release measurement results for source S10 with different phases of geometrical simplifications.

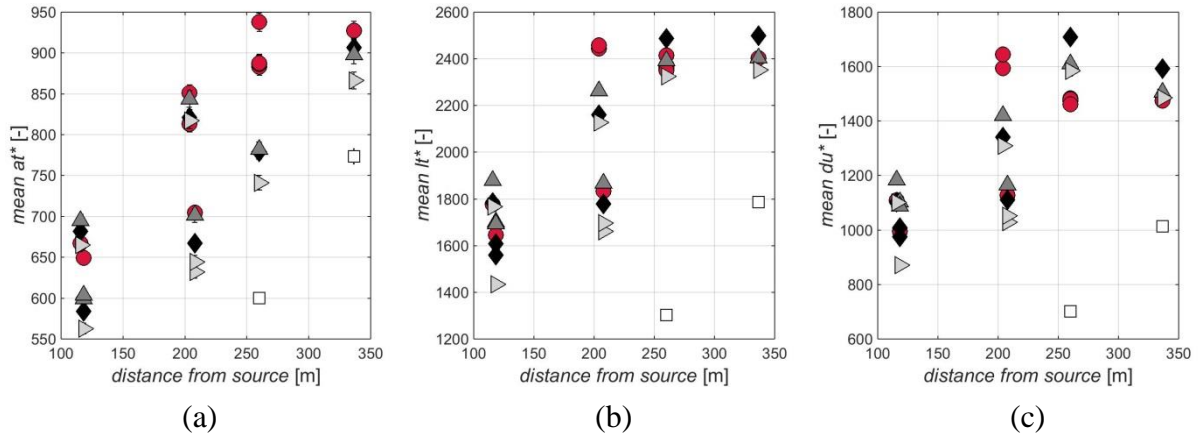


Figure 6.25 measured mean arrival time (a), leaving time (b) and duration (c) of puff releases for source S11 with different phases of geometrical simplifications.

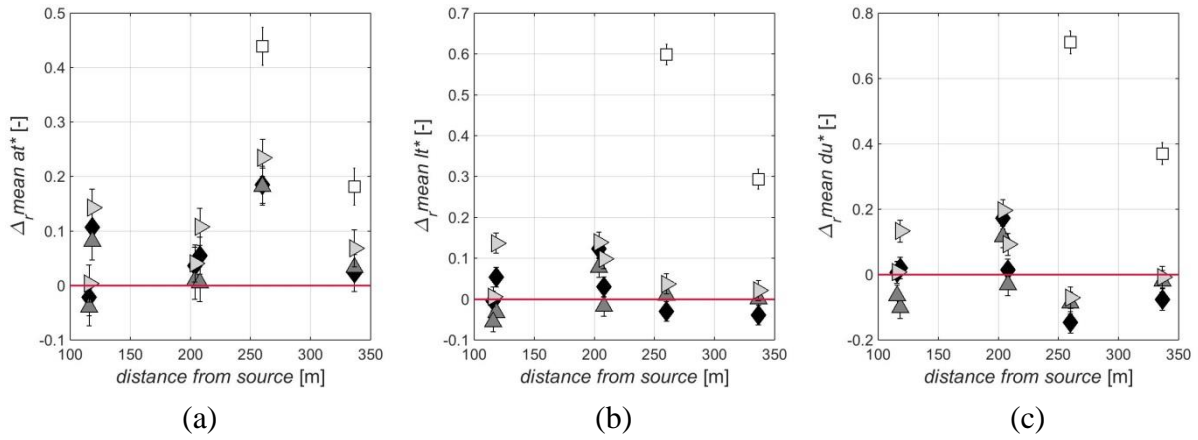


Figure 6.26 The relative differences of measured mean arrival time (a), leaving time (b) and duration (c) of puff releases for source S11 with different phases of geometrical simplifications.

Bibliography

- Allwine, K. J., Leach, M. J., Stockham, L. W., Shinn, J. S., Hosker, R. P., Bowers, J. F. and Pace, C. J. (2004): Overview of Joint Urban – An atmospheric dispersion study in Oklahoma City. *AMS symposium on planning, nowcasting, and forecasting in the urban zone*, Paper J7.1., Seattle.
- Arya, S. P. (2001): Introduction to Micrometeorology. *International Geophysics Series*, No. 42, 2nd edn, Academic Press, San Diego.
- Balczó, M. (2015): *A légszennyező anyagok terjedése és átszellőzés zárt városi tereken*. PhD thesis, Budapest University of Technology and Economics, Hungary. In Hungarian.
- Balczó, M. and Lajos, T. (2015): Flow and dispersion phenomena in a simplified urban square. *Periodica Polytechnica: Civil Engineering*, 59, 347–360.
- Balczó, M. and Tomor, A. (2016): Wind tunnel and computational fluid dynamics study of wind conditions in an urban square. *Időjárás*, 120(2), 199–229.
- Balkema, A. A. and de Haan, L. (1974): Residual Life Time at Great Age. *The Annals of Probability*, 2(5), 792–804.
- Bastigkeit, I. (2011): *Erzeugung von Validierungsdaten für wirbelauflösende mikroskalige Strömungs- und Ausbreitungsmodelle*. PhD thesis, University of Hamburg, Germany. In German.
- Batchelor, G. K. (1967): *An Introduction to Fluid Dynamics*. Cambridge University Press. England.
- Beirlant, J., Goegebeur, Y., Segers, J., Teugels, J., De Waal, D. and Ferro, C. (2004): *Statistics of Extremes*. John Wiley & Sons Ltd. England.
- Bensalah, Y. (2000): *Steps in Applying Extreme Value Theory to Finance: A Review*. Bank of Canada, Ottawa.
- Berbekar, E., Harms, F. and Leitl, B. (2015a): Dosage-based parameters for characterization of puff dispersion results. *Journal of Hazardous Materials*, 283, 178–185.
- Berbekar, E., Harms, F. and Leitl, B. (2015b): Concentration decay from point-source releases in an urban environment. *PHYSMOD 2015 – International Workshop on Physical Modeling of Flow and Dispersion Phenomena*. Zürich, Switzerland.

-
- Berbekar, E., Harms, F., Lübcke, M. and Leitl, B. (2013): Validation data set for local-scale emergency response models. *PHYSMOD 2013 – International Workshop on Physical Modeling of Flow and Dispersion Phenomena*. Guildford, England.
- Beychok, M. R. (1944): *Fundamentals Of Stack Gas Dispersion*. 3rd edn, author-published, USA.
- Boris, J. (2002): The threat of chemical and biological terrorism: Preparing a response. *Computing in Science and Engineering*, 4(2), 22–32.
- Boris, J., Fulton, J. and Obenschain, K., Patnaik, G., Young, T. (2004): CT-analyst: Fast and accurate CBR emergency assessment. *Conference on Chemical and Biological Sensing V*. Orlando, USA.
- Boris, J. P., Landsberg, A. M., Oran, E. S. and Gardner, J. H. (1993): *LCPFCT – a flux-corrected transport algorithm for solving generalized continuity equations*. U.S. Naval Research Laboratory Memorandum Report NRL/MR/6410-93-7192.
- Branford, S., Coceal, O., Thomas, T. G. and Belcher, S. E. (2011): Dispersion of a Point-Source Release of a Passive Scalar Through an Urban-Like Array for Different Wind Directions. *Boundary-Layer Meteorology*, 139(3), 367–394.
- Britter, R. E. and Hanna, S. R. (2003): Flow and Dispersion in Urban Areas. *Annual Review of Fluid Mechanics*, 35(1), 469–496.
- Britter, R. and Schatzmann, M. (2007): *Model evaluation guidance and protocol document*. COST Action 732, University of Hamburg, Germany.
- Brixey, L. A., Richmond-Bryant, J., Heist, D. K., Bowker, G. E., Perry, S. G. and Wiener, R. W. (2009): The effect of a tall tower on flow and dispersion through a model urban neighborhood. *Journal of Environmental Monitoring : JEM*, 11(12), 1–25.
- Buckingham, E. (1914): On physically similar systems; illustrations of the use of dimensional equations. *Physical Review*, 4(4), 345-376.
- Chatwin, P. C. (1982): The use of statistics in describing and predicting the effects of dispersing gas clouds. *Journal of Hazardous Materials*, 6, 213–230.
- Chavez, M., Hajra, B., Stathopoulos, T. and Bahloul, A. (2011): Near-field pollutant dispersion in the built environment by CFD and wind tunnel simulations. *Journal of Wind Engineering and Industrial Aerodynamics*, 1–10.
- Cheng, W. K., Summers, T. and Collings, N. (1998): The fast-response flame ionization detector. *Prog. Energy Combust. Sci.*, 24, 89–124.
- Coceal, O., Goulart, E. V., Branford, S., Glyn Thomas, T. and Belcher, S. E. (2014): Flow structure and near-field dispersion in arrays of building-like obstacles. *Journal of Wind Engineering and Industrial Aerodynamics*, 125, 52–68.
-

-
- Coles, S. (2001): *An Introduction to Statistical Modeling of Extreme Values*. Springer London, England.
- Conrad, O., Bechtel, B., Bock, M., Dietrich, H., Fischer, E., Gerlitz, L., Wehberg, J., Wichmann, V. and Boehner, J. (2015): System for Automated Geoscientific Analyses (SAGA) v. 2.1.4. *Geosci. Model Dev.*, 8, 1991-2007
- COST ES1006 (2012): *Background and Justification Document*, COST Action ES1006, May 2012.
- COST ES1006 (2015a): *Best Practice Guidelines*, COST Action ES1006, April 2015.
- COST ES1006 (2015b): *Model Evaluation Case Studies*, COST Action ES1006, April 2015.
- COST ES1006 (2015c): *Model evaluation protocol*, COST Action ES1006, April 2015.
- Cybyk, B. Z., Boris, J. P., Young, T. R., Emery, M. H. and Cheatham, S. A. (2001): Simulation of fluid dynamics around complex urban geometries. *AIAA*, Paper 2001-0803. Washington DC, USA.
- Cybyk, B. Z., Boris, J. P., Young, T. R., Lind, C. A. and Landsberg, A. M. (1999): A detailed contaminant transport model for facility hazard assessment in urban areas. *AIAA*, Paper 99-3441. Washington DC, USA.
- Davidson, M. J., Mylne, K. R., Jones, C. D., Phillips, J. C., Perkins, R. J., Fung, J. C. H. and Hunt, J. C. R. (1995): Plume dispersion through large groups of obstacles - a field investigation. *Atmospheric Environment*, 29(22), 3245–3256.
- Davidson, M. J., Snyder, W. H., Lawson, R. E. and Hunt, J. C. R. (1996): Wind tunnel simulations of plume dispersion through groups of obstacles. *Atmospheric Environment*, 30(22), 3715–3731.
- Doran, J. C., Allwine, K. J., Flaherty, J. E., Clawson, K. L. and Carter, R. G. (2007): Characteristics of puff dispersion in an urban environment. *Atmospheric Environment*, 41(16), 3440–3452.
- Durst, F., Melling, A. and Whitelaw, J. H. (1976): *Principles and Practice of Laser-Doppler Anemometry*. Academic Press. London, England.
- Dym, C. L. (2004): *Principles of Mathematical Modeling*, 2nd edn, Academic Press. Burlington, USA.
- Dym, C. L. and Ivey, E. S. (1980): *Principles of Mathematical Modeling*, 1st edn, Academic Press. New York, USA.
- Efthimiou, G. C., Berbekar, E., Harms, F., Bartzis, J. G. and Leitl, B. (2015): Prediction of high concentrations and concentration distribution of a continuous point source release in a semi-idealized urban canopy using CFD-RANS modeling. *Atmospheric Environment*, 100, 48–56.
-

-
- ESDU (1985): *ESDU 85020 - Characteristics of atmospheric turbulence near the ground. Part II: single point data for strong winds (neutral atmosphere)*. Engineering Sciences Data Unit, London, England.
- Etling, D. (2008): *Theoretische Meteorologie*, 3rd edn, Springer Berlin, Germany. In German.
- Fackrell, J. E. (1984): Parameters characterising dispersion in the near wake of buildings. *Journal of Wind Engineering and Industrial Aerodynamics*, 16, 97–118.
- Fischer, R. (2011): *Entwicklung eines problemorientierten Software-Pakets zur automatisierten Aufbereitung, Analyse und Dokumentation von im Windkanal produzierten Daten zur LES-Validierung*. PhD thesis, University of Hamburg, Germany. In German.
- Fischer, R. A. and Tippett, L. H. C. (1928): Limiting forms of the frequency distributions of the largest or smallest members of a sample. *Proceedings to the Cambridge Philosophical Society*, 24, 180–190.
- Freedman, D. and Diaconis, P. (1981): On the histogram as a density estimator: L_2 theory. *Zeitschrift Für Wahrscheinlichkeitstheorie Und Verwandte Gebiete*, 57, 453–476.
- Gariazzo, C., Lamberti, M., Hänninen, O., Silibello, C., Pelliccioni, A., Porta, D., Cecinato, A., Gherardi, M. and Forastiere, F. (2015): Assessment of population exposure to Polycyclic Aromatic Hydrocarbons (PAHs) using integrated models and evaluation of uncertainties. *Atmospheric Environment*, 101, 235–245.
- Gifford, F. A. (1961): Use- of Routine Meteorological Observations for Estimating Atmospheric Dispersion. *Nucl. Saf.*, 2(4), 47–57.
- Gnedenko, B. V. (1943): Sur la distribution limite du terme maximum d'une série aléatoire. *Annals of Mathematics*, 44, 423–453. In French.
- Gomes, M. S. D. P., Isnard, A. A. and Pinto, J. M. D. C. (2007): Wind tunnel investigation on the retention of air pollutants in three-dimensional recirculation zones in urban areas. *Atmospheric Environment*, 41, 4949–4961.
- Grimmond, C. S. B., Blackett, M., Best, M. J., Baik, J. J., Belcher, S. E., Beringer, J., Bohnenstengel, S. I., Calmet, I., Chen, F., Coutts, A., Dandou, A., Fortuniak, K., Gouvea, M. L., Hamdi, R., Hendry, M., Kanda, M., Kawai, T., Kawamoto, Y., Kondo, H., Krayenhoff, E. S., Lee, S. H., Loridan, T., Martilli, A., Masson, V., Miao, S., Oleson, K., Ooka, R., Pigeon, G., Porson, A., Ryu, Y. H., Salamanca, F., Steeneveld, G. J., Tombrou, M., Voogt, J. a., Young, D. T. and Zhang, N. (2011): Initial results from Phase 2 of the international urban energy balance model comparison. *International Journal of Climatology*, 31, 244–272.
- Grimmond, C. S. B. and Oke, T. R. (1999): Aerodynamic Properties of Urban Areas Derived from Analysis of Surface Form. *Journal of Applied Meteorology*, 38, 1262–1292.
-

-
- Grimmond, C. S. B. and Oke, T. R. (2002): Turbulent Heat Fluxes in Urban Areas: Observations and a Local-Scale Urban Meteorological Parameterization Scheme (LUMPS). *Journal of Applied Meteorology*, 41, 792–810.
- Hanna, S. (2010): A history of classic atmospheric dispersion field experiments. *AMS 16th Conference on Air Pollution Meteorology*. Atlanta, GA, USA.
- Hanna, S. R., Briggs, G. A. and Hosker, R. P. (1982): *Handbook on atmospheric diffusion*. United States Department of Energy, Springfield, USA
- Hanna, S. and Chang, J. (2012): Acceptance criteria for urban dispersion model evaluation. *Meteorology and Atmospheric Physics*, 116(3–4), 133–146.
- Hanna, S., Chang, J. and Strimaitis, D. (1993): Hazardous gas model evaluation with field observations. *Atmospheric Environment*, 27(15), 2265–2285.
- Harms, F. (2010): *Systematische Windkanaluntersuchungen zur Charakterisierung instationärer Ausbreitungsprozesse einzelner Gaswolken in urbanen Rauigkeitsstrukturen*. PhD thesis, University of Hamburg, Germany. In German.
- Harms, F., Leitl, B., Schatzmann, M. and Patnaik, G. (2011): Validating LES-based flow and dispersion models. *Journal of Wind Engineering and Industrial Aerodynamics*, 99(4), 289–295.
- Hässelbarth, W., Golze, M., Noack, S. and Subaric-Leitis, A. (2006): *EUROLAB Technical Report - Guide to the Evaluation of Measurement Uncertainty for Quantitative Test Results*. Technical Report No. 1/2006, Paris, France.
- Hasselman, T. K., Wathugala, G. W. and Crawford, J. (2002): A Hierarchical Approach for Model Validation and Uncertainty Quantification. *Fifth World Congress on Computational Mechanics*, Vienna, Austria.
- Heist, D. K., Brixey, L. A., Richmond-Bryant, J., Bowker, G. E., Perry, S. G. and Wiener, R. W. (2009): The effect of a tall tower on flow and dispersion through a model urban neighborhood: Part 1. Flow characteristics. *Journal of Environmental Monitoring*, 11(12), 2163–2170.
- Hellweg, M. (2015): *Systematische Auswertung von Messungen zur Ausbreitung störfallartig freigesetzter Luftschadstoffe im Stadtgebiet Hamburgs*. Bachelor's thesis, University of Hamburg, Germany. In German.
- Hertwig, D. (2013): *On Aspects of Large-Eddy Simulation Validation for Near-Surface Atmospheric Flows*. PhD thesis, University of Hamburg, Germany.
- Hertwig, D., Efthimiou, G. C., Bartzis, J. G. and Leitl, B. (2012): CFD-RANS model validation of turbulent flow in a semi-idealized urban canopy. *Journal of Wind Engineering and Industrial Aerodynamics*, 111, 61–72.
-

-
- Higson, H. L., Griffiths, R. F., Jones, C. D. and Bilton, C. (1995): Effect of atmospheric stability on concentration fluctuations and wake retention times for dispersion in the vicinity of an isolated building. *Environmetrics*, 6, 571–581.
- Hopman, T. (2002): *Introduction to indicial notation*. Department of Physics, University of Guelph, Canada.
- Isaacson, M. S. and Sandri, G. v. H. (1990): Laboratory study of pollutant detention times in wake cavities downwind of low-rise buildings. *Journal of Wind Engineering and Industrial Aerodynamics*, 36, 653-663.
- Janssen, T. (2013): *Windkomfort und bodennahe Luftbewegung im Bereich des geplanten Campus Bundesstraße am Standort Geomatikum*. Master's thesis, University of Hamburg, Germany. In German.
- JCGM: Joint Committee for Guides in Metrology (2008): *Evaluation of measurement data: Guide to the expression of uncertainty in measurement*, 1st edn, JCGM 100:2008
- Kipsch, F. (2014): *Systematische Windkanaluntersuchungen zur Charakterisierung des Einflusses der urbanen Baustruktur hinsichtlich der Stadtdurchlüftung*. PhD thesis, University of Hamburg, Germany. In German.
- Klein, P., Leitl, B. and Schatzmann, M. (2010a): Concentration fluctuations in a downtown urban area. Part II: analysis of Joint Urban 2003 wind-tunnel measurements. *Environmental Fluid Mechanics*, 11(1), 43–60.
- Klein, P. M. and Young, D. T. (2010b): Concentration fluctuations in a downtown urban area. Part I: analysis of Joint Urban 2003 full-scale fast-response measurements. *Environmental Fluid Mechanics*, 11(1), 23–42.
- Kochanski, A. K., Pardyjak, E. R., Stoll, R., Gowardhan, A., Brown, M. J. and Steenburgh, W. J. (2015): One-way coupling of the WRF-QUIC Urban dispersion modeling system. *Journal of Applied Meteorology and Climatology*, 54(10), 2119–2139.
- Kolmogorov, A. N. (1991): Dissipation of Energy in the Locally Isotropic Turbulence. *Proceedings of the Royal Society A: Mathematical, Physical and Engineering Sciences*, 434(1890), 15–17.
- Lajos, T. (2008): *Az áramlástan alapjai*, 4th edn, Budapest University of Technology and Economics, Hungary. In Hungarian.
- Lateb, M., Meroney, R. N., Yataghene, M., Fellouah, H., Saleh, F. and Boufadel, M. C. (2015): On the use of numerical modelling for near-field pollutant dispersion in urban environments – A review. *Environmental Pollution*, 1-13.
- Leitl, B. (2009): Advances and Challenges in Applied Flow and Dispersion Modelling. *Seventh Asia-Pacific Conference on Wind Engineering*. Taipei, Taiwan.
-

-
- Leitl, B., Chauvet, C., Schatzmann, M. (2001): Effects of Geometrical Simplification and Idealization on the Accuracy of Microscale Dispersion Modelling. *Proc. 3rd Int. Conf. on Urban Air Quality*, Loutraki, Greece.
- Leitl, B., Harms, F., Berbekar, E. and Patnaik, G. (2016): *Weiterentwicklung des Softwaretools zur Simulation der Ausbreitung von Gefahrstoffen in den bodennahen Luftschichten Hamburgs*. Report. University of Hamburg, Germany. In German.
- Leitl, B., Hertwig, D., Harms, F. and Schatzmann, M. (2012): *Entwicklung eines Werkzeugs zur Optimierung der Einsatzsteuerung bei Gefahrstofffreisetzungen in Stadtgebieten*. Report. University of Hamburg, Germany. In German.
- Lübcke, M. (2014): *Transiente Ausbreitungsprozesse in einer semi-idealisierten Stadtstruktur*. Master's thesis, University of Hamburg, Germany. In German.
- Ma, Y., Boybeyi, Z., Hanna, S. and Chayantrakom, K. (2005): Plume dispersion from the MVP field experiment. Analysis of surface concentration and its fluctuations. *Atmospheric Environment*, 39(17), 3039–3054.
- MacDonald, R. W., Griffiths, R. F. and Cheah, S. C. (1997): Field experiments of dispersion through regular arrays of cubic structures. *Atmospheric Environment*, 31(6), 783–795.
- Macdonald, R. W., Griffiths, R. F. and Hall, D. J. (1998): A comparison of results from scaled field and wind tunnel modelling of dispersion in arrays of obstacles. *Atmospheric Environment*, 32(22), 3845–3862.
- Mann, P. S. (1992): *Introductory Statistics*, 1st edn, Wiley, New York, USA.
- Mavroidis, I., Andronopoulos, S. and Bartzis, J. G. (2012): Computational simulation of the residence of air pollutants in the wake of a 3-dimensional cubical building. The effect of atmospheric stability. *Atmospheric Environment*, 63, 189–202.
- McNeil, A. J. (1997): Estimating the Tails of Loss Severity Distributions Using Extreme Value Theory. *ASTIN Bulletin*, 27(1), 117–137.
- McQuaid, J. (1985): Heavy gas dispersion trials at Thorney Island. *Proceedings of a Symposium held at the University of Sheffield*, U.K.
- Mendoza, C. (1994): A theorem for rayleigh's method of dimensional analysis and its proof. *Mechanics Research Communications*, 21(2), 103–107.
- Mole, N., Schopflocher, T. P. and Sullivan, P. J. (2008): High concentrations of a passive scalar in turbulent dispersion. *Journal of Fluid Mechanics*, 604, 447–474.
- Moonen, P., Gromke, C. and Dorer, V. (2013): Performance assessment of Large Eddy Simulation (LES) for modeling dispersion in an urban street canyon with tree planting. *Atmospheric Environment*, 75, 66–76.

-
- Munro, R., Chatwin, P. and Mole, N. (2001): The high concentration tails of the probability density function of a dispersing scalar in the atmosphere. *Boundary-Layer Meteorology*, (2), 315–339.
- Mylne, K. and Mason, P. (1991): Concentration fluctuation measurements in a dispersing plume at a range of up to 1000 m. *Quarterly Journal of the Royal Meteorological Society*, 117(497), 177–206.
- Mylne, K. R. (1992): The PDF of concentration fluctuations - comments on Yee (1990) and Yee (1991). *Boundary-Layer Meteorology*, 61, 189–193.
- Nironi, C., Salizzoni, P., Marro, M., Mejean, P., Grosjean, N. and Soulhac, L. (2015): Dispersion of a Passive Scalar Fluctuating Plume in a Turbulent Boundary Layer . Part I : Velocity and Concentration Measurements. *Boundary-Layer Meteorology*, 156(3), 415–446.
- NRL: Naval Research Laboratory (2016): CT-Analyst. Website: <http://www.nrl.navy.mil/lcp/ct-analyst> (last accessed on September 20, 2016).
- Oberkampf, W. L. and Trucano, T. G. (2002): Verification and validation in computational fluid dynamics. *Progress in Aerospace Sciences*, 38, 209–272.
- OED Online: Oxford English Dictionary (2015): *transient*, *adj.* and *n.* Website: <http://www.oed.com/view/Entry/204789?redirectedFrom=transient&> (last accessed on December 02, 2015), Oxford University Press, England.
- Oke, T. R. (1982): The energetic basis of the urban heat island. *Quarterly Journal of the Royal Meteorological Society*, 108, 1-24.
- Pasquill, F. (1961): The Estimation of the Dispersion of Windborne Material. *Meteorol. Mag.*, 90, 33–49.
- Pasquill, F. (1974): *Atmospheric Diffusion* 2nd edn, John Wiley & Sons, New York, USA.
- Patnaik, G., Boris, J. P., Grinstein, F. F. and Iselin, J. (2005): Large scale urban simulations with FCT. In *Kuzmin, D., Löhner, R., Turek, S. (Eds.), High-Resolution Schemes for Convection-Dominated Flows: 30 Years of FCT* (pp. 105–130). Springer.
- Petersen, G. (2013): *Wind tunnel modelling of atmospheric boundary layer flow over hills*. PhD thesis, University of Hamburg, Germany.
- Pickands, J. . (1975): Statistical inference using extreme order statistics. *Annals of Statistics*, 3(1), 119–131.
- Puttock, J.S., Colenbrander, G. W. (1985): Thorney Island data and dispersion modelling. *Journal of Hazardous Materials*, 11, 381-397.
- Rakai, A. (2014): *(Wind and) Smog in the city – Towards operational modelling of flow and dispersion in urban areas with Computational Fluid Dynamics (CFD)*. PhD thesis, Budapest University of Technology and Economics, Hungary.
-

-
- Rakai, A., Kristof, G. and Franke, J. (2013): Sensitivity analysis of microscale obstacle resolving models for an idealized Central-European city centre, Michel-Stadt. *Időjárás*, 118(1), 53–77.
- Richardson, L. F. (1926): Atmospheric Diffusion Shown on a Distance-Neighbour Graph Lewis. *Proc. Roy. Soc. (London), Series A*, 110(756), 709–737.
- Richmond-Bryant, J. and Reff, A. (2012): Air pollution retention within a complex of urban street canyons: A two-city comparison. *Atmospheric Environment*, 49, 24–32.
- Roberts, E. M. (1979): Review of Statistics of Extreme Values with Applications to Air Quality Data. *Journal of the Air Pollution Control Association*, 29(7), 733–740.
- Roberts, O. F. T. (1923): The Theoretical Scattering of Smoke in a Turbulent Atmosphere. *Proc. Roy. Soc. A*, 104, 640–654.
- Robins, A., Cheng, H. and Hayden, P. (2013): The dispersion of short duration , ground level emissions in turbulent boundary layers. *PHYSMOD 2013 – International Workshop on Physical Modeling of Flow and Dispersion Phenomena*. Guildford, England.
- Rotach, M. W., Gryning, S. E., Batchvarova, E., Christen, A., Vogt, R. (2003): Pollutant dispersion close to an urban surface – the BUBBLE tracer experiment. *Meteorology and Atmospheric Physics*, 87, 39-56
- Schatzmann, M. and Britter, R. (2011): Quality assurance and improvement of micro-scale meteorological models. *Proceedings of the 11th International Conference on Harmonisation within Atmospheric Dispersion Modelling for Regulatory Purposes* (pp. 159–163)
- Schatzmann, M. and Leitl, B. (2002): Validation and application of obstacle-resolving urban dispersion models. *Atmospheric Environment*, 36, 4811-4821.
- Schatzmann, M. and Leitl, B. (2011): Issues with validation of urban flow and dispersion CFD models. *Journal of Wind Engineering and Industrial Aerodynamics*, 99(4), 169–186.
- Schatzmann, M., Leitl, B. and Liedtke, J. (2000): Dispersion in urban environments - Comparison of field measurements with wind tunnel results. *Environmental Monitoring and Assessment*, 65, 249–257.
- Schatzmann, M., Olesen, H. and Franke, J. (2010): *COST 732 Model evaluation case studies : approach and results*. COST Action 732, University of Hamburg, Germany.
- Schlünzen, K., Bächlin, W. and Brünger, H. (2004): An evaluation guideline for prognostic microscale wind field models. *Proceedings of the 9th Int. Conf. on Harmonisation within Atmospheric Dispersion Modelling for Regulatory Purposes*, 147–150.
- Schopflicher, T. P. and Sullivan, P. J. (1998): A composite PDF of scalar concentration in turbulent flows. *Environmental Modelling & Software*, 13(3–4), 305–308.
- Schopflicher, T. P. and Sullivan, P. J. (2002): A mixture model for the PDF of a diffusing scalar in a turbulent flow. *Atmospheric Environment*, 36(27), 4405–4417.
-

-
- Smith, M. . E. (1968): *Recommended Guide for the Prediction of the Dispersion of Airborne Effluents*. 1st edn, American Society of Mechanical Engineers, New York, USA.
- Snyder, W. H. (1981): *Guideline for fluid modeling of atmospheric diffusion*. Report EPA-600/8-81-009, U.S. Environmental Protection Agency, Research Triangle Park (NC), USA.
- Stockie, J. M. (2011): The Mathematics of Atmospheric Dispersion Modeling. *SIAM Review*, 53(2), 349–372.
- Sutton, O. G. (1932): A Theory of Eddy Diffusion in the Atmosphere. *Proc. R. SOC. (London), Ser. A*, 135, 143.
- Taylor, B. N. and Kuyatt, C. E. (1994): *Guidelines for Evaluating and Expressing the Uncertainty of NIST Measurement Results*. NIST Technical Note 1297, Physics Laboratory, National Institute of Standards and Technology, Gaithersburg, USA.
- Taylor, J. R. (1983): *An Introduction to Error Analysis: The Study of Uncertainties in Physical Measurements*. *American Journal of Physics*. 2nd ed. University Science Books.
- Townsend, A. A. (1956): *The Structure of Turbulent Shear Flow*. University Press. Cambridge, England.
- Trini Castelli, S., Leitl, B., Baumann-Stanzer, K., Reisin, T.G., Armand, P., Andronopoulos, S., and all COST ES1006 Members. (2016): Conclusions and reflections from COST Action ES1006 activity: What do we miss for the applications of models in local-scale emergency response in built environments? In *17th International Conference on Harmonisation within Atmospheric Dispersion Modelling for Regulatory Purposes*. Budapest, Hungary.
- Tritton, D. J. (1988): *Physical Fluid Dynamics* 2nd edn, Clarendon Press, Oxford, England.
- Tseng, Y.-H., Meneveau, C. and Parlange, M. B. (2006): Modeling flow around bluff bodies and predicting urban dispersion using large eddy simulation. *Environmental Science & Technology*, 40, 2653–2662.
- van Milligen, B. P., Bons, P. D., Carreras, B. A and Sánchez, R. (2005): On the applicability of Fick’s law to diffusion in inhomogeneous systems. *European Journal of Physics*, 26, 913–925.
- VDI 3783/12: Verein Deutscher Ingenieure (2000): *Environmental meteorology – Physical modelling of flow and dispersion processes in the atmospheric boundary layer – Application of wind tunnels*. Guideline VDI-3783-12, Beuth Verlag, Berlin, Germany.
- Weil, J. C., Snyder, W. H., Lawson, R. E. and Shipman, M. S. (2002): Experiments on buoyant plume dispersion in a laboratory convection tank. *Boundary-Layer Meteorology*, 102(3), 367–414.
- Wikipedia (2016a): *Hamburger Rathaus*. Website: https://de.wikipedia.org/wiki/Hamburger_Rathaus (last accessed on September 20, 2016). In German.
-

-
- Wikipedia (2016b): *HafenCity*. Website: <https://en.wikipedia.org/wiki/HafenCity> (last accessed on September 20, 2016).
- Xie, Z.-T., Hayden, P., Robins, A. G. and Voke, P. R. (2007): Modelling extreme concentrations from a source in a turbulent flow over a rough wall. *Atmospheric Environment*, 41(16), 3395–3406.
- Yassin, M. F. and Elmi, A. A. (2011): Stochastic analysis of concentration field in a wake region. *Environmental Science and Pollution Research International*, 18(2), 270–81.
- Yee, E. (1990): The shape of the probability density function of short-term concentration fluctuations of plumes in the atmospheric boundary layer. *Boundary-Layer Meteorology*, 51(3), 269–298.
- Yee, E. (2008): Probability law of concentration in plumes dispersing in an urban area. *Environmental Fluid Mechanics*, 9(4), 389–407.
- Yee, E., Kosteniuk, P. R., Chandler, G. M., Biltoft, C. A. and Bowers, J. F. (1993): Statistical characteristics of concentration fluctuations in dispersing plumes in the atmospheric surface layer. *Boundary-Layer Meteorology*, 65, 69–109.
- Yim, S. H. L., Fung, J. C. H., Lau, A. K. H. and Kot, S. C. (2009): Air ventilation impacts of the “wall effect” resulting from the alignment of high-rise buildings. *Atmospheric Environment*, 43(32), 4982–4994.

List of Figures

Figure 1.1 Scatter-plots of measured versus ensemble averaged modeled mean concentration values for continuous releases within the Michelstadt blind test case for model Type I (a), Type II (b) and Type III (c). Source: COST ES1006 (2015b)3

Figure 2.1 The relation between our conceptual models of the world and observations made within the real world (inspired by Dym and Ivey, 1980)8

Figure 2.2 Schematic of the planetary boundary layer (based on Arya, 2001 and Hertwig, 2013). The heights are more typical for neutral stability and they are highly variable in space and time. 14

Figure 3.1: Sketch of the Wotan boundary-layer wind tunnel (Harms, 2010).....24

Figure 3.2 Parts of concentration time series of a continuous release (a) and a puff release (b) measurement. Results are in model scale.25

Figure 3.3 The peak time and the dosage-based arrival time and leaving time indicated in a puff measurement time series. (Based on Figure 4 in the paper of Berbekar et al., 2015a).28

Figure 3.4 The relationship between the dosage and the reference wind speed in model scale for various measurement locations. The quality of the fit of $f(x)=a/x$ is characterized by the R^2 value. The data for this graph was taken from the measurements described in Harms et al. (2011) and Harms (2010).29

Figure 3.5 Exemplary results for the relationship between the concentration and the reference wind speed in model scale for puffs (a) and for continuous releases (b). The goodness of the fit for (b) is characterized by the R^2 value. The puff results are from the measurements described in Harms et al. (2011) and Harms (2010). The continuous release case was measured within the Hamburg model.30

Figure 3.6 The relationship between the peak concentration related to the flow rate (pc/Q) and the release duration (T_{rel}) in model scale for short-term releases. The results are from the measurements described in (Frank Harms, 2010) (a) and the first (b) and the second (c) campaign of the Hamburg measurements (see Chapter 3.2.5). The points without marker face coloring were not considered for the linear fitting.32

Figure 3.7 The mean, standard deviation, 95th percentile and the maximum of the concentration distribution resulting from a continuous release measurement during the Michelstadt campaign.34

Figure 3.8 Michelstadt model in the wind tunnel35

Figure 3.9 Map of the area modeled in the wind tunnel (a). Hamburg model in the wind tunnel (b).	35
Figure 3.10 The dimensionless longitudinal pressure gradient of the wind tunnel during the measurements of the Hamburg test case. The thick solid lines represent the Eq. (3.30) criterion. The x axis represents the distance from the upwind side of the approach flow section of the wind tunnel.	37
Figure 3.11 The lateral velocity profile in the wind tunnel (a) and the profile of a Reynolds-number independence test (b) during the wind tunnel measurements of the Hamburg test case. (The gray lines are only plotted as visual aids, and have no physical or mathematical meaning.)	38
Figure 3.12: Comparison between the previous and new campaigns of vertical profiles of statistical measures of the velocity component u_x for the Hamburg model: mean velocity (a), turbulence intensity (b), integral length scale of turbulence (c) and flux (d).	39
Figure 3.13 Comparison between the previous and new campaigns of vertical profiles of statistical measures of the velocity component u_x for the Michelstadt model: mean velocity (a), turbulence intensity (b), integral length scale of turbulence (c) and flux (d).	40
Figure 3.14 Exemplary concentration measurements of the Reynolds-number independence tests for the Michelstadt (a) and the Hamburg (b) test case.	41
Figure 3.15 Exemplary convergence plots of the mean concentration for continuous releases (a) and peak concentration for puff releases (b).	42
Figure 3.16 Exemplary distributions of standard deviations of the mean concentration (a) and coefficients of variation (b) for the continuous release repetition measurements of the Hamburg test case.	43
Figure 3.17 95th percentiles of the concentration distributions, taken from the two measurement campaigns of the Hamburg test case.	45
Figure 3.18 The geometry of Michelstadt. The arrows indicate the two measured wind directions and the sources are marked with dots. The labels are the names of the source locations.	46
Figure 3.19 The area of the Hamburg model. The red dots represent the release locations. The labels are the names of the source locations.	46
Figure 3.20 Original, high resolution geometry.	47
Figure 3.21 Phase 1 geometry.	47
Figure 3.22 Phase 2 geometry.	47
Figure 3.23 Phase 3 geometry.	48
Figure 3.24 Phase 0 geometry, where the city hall is missing.	48
Figure 3.25 The city hall of Hamburg (a, source: Wikipedia, 2016a). The model of the city hall in the high-resolved (b) and LoD1 (c) geometries.	48

Figure 4.1 Definition of coordinate system for a point source release on a flat-open terrain. The source is marked with a black star and the wind direction is pointing from left to right. The arrow shows the wind direction of the approach flow and the shades of grey correspond to the expected concentration levels.....	54
Figure 4.2 Exemplary longitudinal mean concentration profile measured at half-building height in a street canyon of the Michelstadt model (a). The fit of the simplified Gaussian distribution in x direction is indicated with a black line. The locations of the source (square) and measurements (circles) within the model (b). The mean wind direction of the approach flow is from left to right, as for all figures without the indication of the wind direction.	56
Figure 4.3 Exemplary longitudinal mean concentration profile measured at half-building height within separate street canyons in the Michelstadt model (a). The fit of the simplified Gaussian distribution in x direction is indicated with a black line. The locations of the source (square) and measurements (circles) within the model (b).	57
Figure 4.4 Exemplary longitudinal mean concentration profile measured above the buildings of the Michelstadt model at 52.4 m height in full scale (a). The fit of the simplified Gaussian distribution in x direction is indicated with a black line. The locations of the source (square) and measurements (circles) within the model (b).	57
Figure 4.5 Exemplary longitudinal mean concentration profile measured at pedestrian level in the Hamburg model (a). The fit of the simplified Gaussian distribution in x direction is indicated with a black line. The locations of the source (square) and measurements (circles) within the model (b).	58
Figure 4.6 Exemplary longitudinal mean concentration profile measured above roof level of the Hamburg model at z=52.5 m height in full scale (a). The fit of the simplified Gaussian distribution in x direction is indicated with a black line. The locations of the source (square) and measurements (circles) within the model (b).	58
Figure 4.7 Lateral mean concentration profiles measured at half-building height in the Michelstadt model (a). The fits of the simplified Gaussian distribution in y direction are indicated with lines. The locations of the source (square) and measurements (circles) within the model (b).	59
Figure 4.8 Lateral mean concentration profiles measured above the buildings of the Michelstadt model at 52.4 m in full scale (a). The fits of the simplified Gaussian distribution in y direction are indicated with lines. The locations of the source (square) and measurements (circles) within the model (b).	60
Figure 4.9 Lateral mean concentration profiles measured at pedestrian height (black) and at 12.6-m height (gray) in full scale in the Hamburg model (a). The fits of the simplified Gaussian distribution in y direction are indicated with lines. The locations of the source (square) and measurements (circles) within the model (b).	60

Figure 4.10 Lateral mean concentration profile measured at pedestrian height in the Hamburg model (a). The fit of the simplified Gaussian distribution in y direction is indicated with a black line. The locations of the source (square) and measurements (circles) within the model (b).	61
Figure 4.11 Vertical mean concentration profiles measured within the Michelstadt model. The fits of the simplified vertical Gaussian distribution are indicated with lines. The locations of the source (square) and measurements (circles) within the model (b).	61
Figure 4.12 Vertical mean concentration profiles measured within the Michelstadt model. The fits of the simplified vertical Gaussian distribution are indicated with lines. The locations of the source (square) and measurements (circles) within the model (b).	62
Figure 4.13 Normal, clipped normal, lognormal, exponential and gamma PDFs (a-c) and CDFs (d-f) fitted on measurement data from the Michelstadt campaign. The measured concentration distribution and its 95th percentile are also plotted. The distribution of the measured data for Figures a-c is indicated with brown color. The measurement locations are shown in (g).	65
Figure 4.14 Scatterplots of the 95th percentiles of the measured and modeled concentration distributions for the Michelstadt data set (a) and the new (b) and previous (c) campaign of the Hamburg measurements.	66
Figure 4.15 Fractional mean bias of the 95th percentile from the fitted on the whole concentration distribution (fit) and estimated from the first two moments (est) PDFs for all measurements. The acceptance zone defined for urban dispersion models is within the green lines.	67
Figure 4.16 Normalized mean-square error of the 95th percentile from the fitted on the whole concentration distribution (fit) and estimated from the first two moments (est) PDFs for all measurements. The acceptance zone defined for urban dispersion models is below the green line.	67
Figure 4.17 Fraction of the 95th percentile from the fitted on the whole concentration distribution (fit) and estimated from the first two moments (est) PDFs for all measurements. The acceptance zone defined for urban dispersion models is above the green line.	68
Figure 4.18 The correlation between the mean and the standard deviation (a) and the mean and 95th percentile (b) of the measured concentration distributions. The black lines indicate the best fit on the whole data set.	69
Figure 4.19 The location of the S2 source (black circle) and the measurement point S2P1 (square) in the Michelstadt model (a). The probability distribution of the measured concentration at S2P1 (b).	70
Figure 4.20 The sensitivity of the shape parameter (a) and scale parameter (b) of the GEV distribution, depending on the block size.	72

Figure 4.21 GEV distribution fitted on the block maxima of the concentration time series with block size 400 for the S2P1 case.....	72
Figure 4.22 Distribution of the shape parameters of the GEV distributions based on all Michelstadt measurements with block size 400 (a), 450 (b) and 500(c).....	73
Figure 4.23 A part of the time series measured at S2P1 location (a). The red line is at $C^*=520$. The mean excess function (MEF) plot of the S2P1 measurement (b).....	74
Figure 4.24 The quantile-quantile (QQ) plots of the raw data (a, b) and the declustered data (c) with $u=400$ (a) and $u=520$ (b, c) thresholds.....	74
Figure 4.25 The sensitivity of the shape parameter (a) and scale parameter (b) of the GPD for the S2P1 measurement, depending on the threshold.....	75
Figure 4.26 GPD fitted on the upper tail of the concentration time series distribution with threshold $u=520$ for the S2P1 measurement without declustering (a) and with declustering (b). .	75
Figure 4.27 Probability density of the shape parameters of the GPD for the whole data set with the 98th percentile (a) and 99th percentile (b) as thresholds.....	76
Figure 4.28 Prediction of the extreme value based on GPD fits with different thresholds. Filled symbols show the predictions with finite upper limit that are above the maximum of the measured distributions (indicated with a red line).	77
Figure 4.29 Averaged time series measured at different locations with identical release conditions; the end of the release is indicated with a red line (a). C_0 defined as the mean concentration between the time steps, when 20% and 80% of the total dosage has reached the measurement location (b). The period between the 20% and 80% of the total dosage is indicated with red lines.	79
Figure 4.30 Time constants resulting from different methods of evaluation (a). Time constants resulting from the same method of evaluation, but averaging at different stages (b). ...	81
Figure 4.31 Eq. (4.13) and Eq. (4.14) fitted on exemplary measurement results of source S4 of the Hamburg data set (a-e). The source location is indicated with a black circle, the measurement points are marked with squares (f).....	83
Figure 4.32 The relationship between the time constants (τ^* [-]) and the distance from the source (a) and the arrival time for short-term releases (b) measured for different source locations within the Hamburg model at pedestrian level. The locations of the sources within the Hamburg model (c).	84
Figure 4.33 The relationship between the leaving time and the arrival time for puff releases measured at S6 source location within the Hamburg model at pedestrian level.....	85
Figure 4.34 Time constants (τ^* [-]) measured for different source locations within the Hamburg model at pedestrian level. The source location is indicated with a black circle. The labels show the actual values of the time constant at each measurement location. The overlapping measurement locations are circled. The uncertainty of the time constants is $\delta\tau^*=85$	86

Figure 4.35 3D model of a part of Hamburg (source: Google Earth). The location of the S9 source (star) and the locations of the shortest (blue arrow) and longest (red arrow) measured residence times are indicated. The direction of the mean approach flow is from left to right.	87
Figure 4.36 Modified building structures within the center of Hamburg between 2008 and 2015 (source: Google Earth). The maps on the left side are from 2008 and the maps on the right were recorded in 2015.	88
Figure 4.37 The locations of the puff measurements of source S11 for the high resolution and phase 1 (Ph1) model geometries. The source is indicated with a black circle and the squares mark the measurement locations. The Ph1 geometry corresponds to the test case, where only the city hall is simplified.	90
Figure 4.38 The measured mean peak concentrations (a); absolute (b) and relative (c) differences of the measured mean peak concentration results of the puff measurements of source S11 for phase 1.	90
Figure 4.39 The measurement point locations for S9 (a) and S11 (b). The sources are marked with a black circle and the squares indicate the measurement locations. The phases of geometrical simplifications are indicated with different shades of grey.	91
Figure 4.40 The measured mean concentrations (a) and the absolute (b) and relative (c) differences of continuous release measurement results for source S9 with different phases of geometrical simplifications.	92
Figure 4.41 The measured mean concentrations (a); absolute (b) and relative (c) differences of continuous release measurement results for source S11 with different phases of geometrical simplifications.	92
Figure 4.42 The measured mean concentrations (a and b) and the measurement locations (c) of the vertical profiles. The source is indicated by a black circle.	94
Figure 4.43 The puff measurement locations for source S11. The black circle indicates the source locations and the measurement points are marked with squares. The phases of geometrical simplifications are indicated with different shades of grey.	94
Figure 4.44 The measured mean peak concentrations (a) and the absolute (b) and relative (c) differences of puff release measurement results for source S11 with different phases of geometrical simplifications.	95
Figure 4.45 The measured mean dosages (a) and the absolute (b) and relative (c) differences of puff release measurement results for source S11 with different phases of geometrical simplifications.	96
Figure 4.46 The measured mean peak time (a), its absolute (b) and relative (c) differences of puff release measurements for source S11 with different phases of geometrical simplifications.	97
Figure 4.47 The absolute differences of measured mean arrival time (a), leaving time (b) and duration (c) of puff releases for source S11 with different phases of geometrical simplifications.	97

Figure 4.48 The measured time constants for the two test cases as function of the distance from the source..... 98

Figure 4.49 Time constants (τ^* [-]) measured for source S10 at pedestrian level within the high resolution (a) and the phase 3 geometries (b). The source is marked with a black circle and the squares correspond to the measurement locations. The labels show the actual values of the time constant at each measurement location. The uncertainty of the time constants is $\delta\tau^*=85$ 98

Figure 4.50 Leaving times of puffs measured for source S10 at pedestrian level within the high resolution (a) and the phase 3 geometries (b). The source is marked with a black circle and the squares correspond to the measurement locations. The labels show the actual values of the time constant at each measurement location. The uncertainty of the time constants is $\delta\tau^*=85$ 99

Figure 6.1 Longitudinal mean concentration profiles measured at half-building height in the Michelstadt model. The fits of the simplified Gaussian distribution in x direction are indicated with lines. The locations of the source (square) and measurements (circles) within the model (b). 107

Figure 6.2 Longitudinal mean concentration profile measured at half-building height in the Michelstadt model. The fit of the simplified Gaussian distribution in x direction is indicated with a black line. The locations of the source (square) and measurements (circles) within the model (b). 107

Figure 6.3 Lateral mean concentration profiles measured at half-building height in the Michelstadt model. The fit of the simplified Gaussian distribution in y direction is indicated with a black line. The locations of the source (square) and measurements (circles) within the model (b). 108

Figure 6.4 Lateral mean concentration profiles measured at half-building height in the Michelstadt model. The fit of the simplified Gaussian distribution in y direction is indicated with a black line. The locations of the source (square) and measurements (circles) within the model (b). 108

Figure 6.5 Lateral mean concentration profiles measured at half-building height in the Michelstadt model. The fit of the simplified Gaussian distribution in y direction is indicated with a black line. The locations of the source (square) and measurements (circles) within the model (b). 109

Figure 6.6 Lateral mean concentration profiles measured at half-building height in the Michelstadt model. The fit of the simplified Gaussian distribution in y direction is indicated with a black line. The locations of the source (square) and measurements (circles) within the model (b). 109

Figure 6.7 Vertical mean concentration profile measured within the Hamburg model. The fit of the simplified Gaussian distribution in y direction is indicated with a black line. The locations of the source (square) and measurements (circles) within the model (b)..... 110

Figure 6.8 Vertical mean concentration profiles measured within the Michelstadt model. The fits of the simplified Gaussian distribution in z direction are indicated with lines. The locations of the source (square) and measurements (circles) within the model.	110
Figure 6.9 The measured 95th percentile of the concentration distributions (a) and their absolute (b) and relative (c) differences of continuous release measurement results for source S11 with different phases of geometrical simplifications.	111
Figure 6.10 The measured 95th percentile of the concentration distributions (a) and their absolute (b) and relative (c) differences of continuous release measurement results for source S9 with different phases of geometrical simplifications.	111
Figure 6.11 The measurement locations (squares) for source S10 (circle). The phases of geometrical simplifications are indicated with different shades of grey.	112
Figure 6.12 The measured mean concentrations (a) and their absolute (b) and relative (c) differences of continuous release measurement results for source S10 with different phases of geometrical simplifications.	112
Figure 6.13 The measured 95th percentile of the concentration distributions (a) and their absolute (b) and relative (c) differences of continuous release measurement results for source S10 with different phases of geometrical simplifications.	112
Figure 6.14 The measurement locations (squares) for source S6 (circle). The phases of geometrical simplifications are indicated with different shades of grey.	113
Figure 6.15 The measured mean concentrations (a) and their absolute (b) and relative (c) differences of continuous release measurement results for source S6 with different phases of geometrical simplifications.	113
Figure 6.16 The measured 95th percentile of the concentration distributions (a) and their absolute (b) and relative (c) differences of continuous release measurement results for source S6 with different phases of geometrical simplifications.	113
Figure 6.17 The measured vertical profiles of the 95th percentile of the concentration distributions (a) and their absolute (b) and relative (c) differences of continuous release measurement results with different phases of geometrical simplifications.	114
Figure 6.18 The puff measurement locations (squares) for source S10 (circle). The phases of geometrical simplifications are indicated with different shades of grey.	114
Figure 6.19 The measured mean peak concentrations (a) and the absolute (b) and relative (c) differences of puff release measurement results for source S10 with different phases of geometrical simplifications.	115
Figure 6.20 The measured mean dosages (a) and the absolute (b) and relative (c) differences of puff release measurement results for source S10 with different phases of geometrical simplifications.	115

Figure 6.21 The measured mean peak times (a) and the absolute (b) and relative (c) differences of puff release measurement results for source S10 with different phases of geometrical simplifications.	115
Figure 6.22 The measured mean arrival times (a) and the absolute (b) and relative (c) differences of puff release measurement results for source S10 with different phases of geometrical simplifications.	116
Figure 6.23 The measured mean leaving times (a) and the absolute (b) and relative (c) differences of puff release measurement results for source S10 with different phases of geometrical simplifications.	116
Figure 6.24 The measured mean durations (a) and the absolute (b) and relative (c) differences of puff release measurement results for source S10 with different phases of geometrical simplifications.	116
Figure 6.25 measured mean arrival time (a), leaving time (b) and duration (c) of puff releases for source S11 with different phases of geometrical simplifications.	117
Figure 6.26 The relative differences of measured mean arrival time (a), leaving time (b) and duration (c) of puff releases for source S11 with different phases of geometrical simplifications.	117

List of Tables

Table 1.1 Types of emergency response tools and atmospheric dispersion models, based on the integrated flow and/or dispersion modeling approaches (COST ES1006, 2015b).2

Table 2.1 Surface roughness length data for different urban and industrial categories (Britter and Hanna, 2003). 15

Table 2.2 Surface roughness lengths and surface displacement length for different surfaces (VDI, 2000) 15

Table 3.1 Uncertainty values of selected statistical parameters characterizing continuous release measurements within the different campaigns.44

Table 3.2 Uncertainty values of some statistical parameters characterizing puff release measurements within the different campaigns.44

Table 3.3 Statistics of the measurements carried out on the two model geometries45

Table 4.1 Literature overview on describing concentration measurements with PDF's.64

Table 4.2 Statistical metrics of the 95th percentile prediction for all measurement campaigns and PDFs. 68

Table 4.3 Literature overview on concentration decay evaluation techniques.80

Table 4.4 List of the measured test cases and the number of modified buildings.89